공학박사 학위논문

Fluorinated Interface Engineering using Conjugated Structures for High Cycling Performance of Lithium Metal-Based Batteries

리튬 금속 기반 배터리의 우수한 사이클 성능을 위한 공액 구조에서의 불소화 계면 공정

2023년 8월

서울대학교 대학원
융합과학부 나노융합전공

표선미

Fluorinated Interface Engineering using Conjugated Structures for High Cycling Performance of Lithium Metal-Based Batteries

지도교수 김 연 상

이 논문을 공학박사학위 논문으로 제출함.

2023년 7월

서울대학교 대학원
융합과학부 나노융합전공
표 선 미

표선미의 박사학위 논문을 인준함

2023 년 7 월

위 원 장 ____________________ 인

부위원장 ____________________ 인

위 원 ____________________ 인

위 원 ____________________ 인

위 원 ____________________ 인

Abstract

Fluorinated Interface Engineering using Conjugated Structures for High Cycling Performance of Lithium Metal-Based Batteries

Seonmi Pyo
Program in Nano Science and Technology
The Graduate School
Seoul National University

High-energy-density rechargeable batteries as an energy storage system have attracted significant interest with a wide range of applications from smart phones to electrical vehicles. Recently, Li metal-based batteries are considered one of the promising next-generation energy storage technologies. Because Li metal anodes (LMAs) offer the lowest negative electrochemical potential, high theoretical specific

capacity, and low gravimetric density. In this respect, Li metal batteries (LMBs) as well as anode-free Li metal batteries (AFLMBs) without excess Li inventory are the ultimate choice of high energy density system.

Despite numerous advantages, Li metal-based batteries have difficulties in practical applications originated by the highly reactive property of Li metal and "hostless" electrochemical plating/stripping processes. Therefore, their intrinsic disadvantages lead to dendritic Li growth and the repeated formation and cracking of the solid electrolyte interphase (SEI) during cycling. Especially, in anode-free designs where there is no excess Li to compensate for the loss of active Li sources, it is more challenging to improve their cycling performances. To address these issues, this dissertation focuses on a critical point related to a favorable interfacial chemistry for promoting the formation of LiF-rich SEI and stabilizing Li plating behavior.

For LMBs, the first part introduces functional safety-reinforced separators using conjugated carbon network (CCN) materials, such as graphene, carbon black, and activated carbon. In the cell operating window, the carbon-coated layer induces an in-situ fluorine doping reaction on CCN in a specific electrolyte solvent, resulting in the formation of LiF-rich SEI on the LMAs. Notably, I generalize the stabilization mechanism of the LMAs by demonstrating a correlation between CCN materials with different structures and fluorinate metathesis.

For AFLMBs, the second part proposes a silver nanoparticles incorporated p-doped conjugated polymer (Ag-PCP) wetting agent on the copper current collector. It promotes Ag-Li alloy reaction and interfacial fluorination of the Ag-PCP wetting agent with π-conjugated structures, which effectively lowers the Li nucleation energy barrier and generates a stable SEI with a high ratio of LiF at the early stage. As a result, the Ag-PCP applied cells show dendrite-free Li morphology and superior cycle performances with high Li utilization efficiency even under harsh conditions.

This dissertation provides promising strategies for interfacial stabilization of Li metal-based batteries, aiming for the practical employment of high-energy-density rechargeable batteries.

Keywords: functional separator, lithiophilic wetting agent, interfacial fluorination, LiF-rich SEI, dendrite-free morphology, lithium metal-based batteries

Student Number: 2018-21982

Contents

Abstract 1

Contents..4

List of figures 7

Chapter 1 Introduction 17

1.1 Overview 17

1.2 Fundamental and literature review 20

1.1.1 Background on Li metal-based batteries...................................20

1.1.2 Challenges of Li metal-based batteries 23

1.1.3 Main strategies for Li metal-based batteries 25

1.3 References 28

Chapter 2 Advanced Li metal anode by fluorinated metathesis on conjugated carbon networks 33

2.1 Introduction 33

2.2 Experimental section 38

2.2.1 Fabrication process 38

2.2.2 Galvanostatic cycling measurements.......................................50

2.2.3 Optophysical characteristics 66

2.2.4 Electron microscopy image analysis...74

2.2.5 F-doping mechanism by fluorinated metathesis 86

2.2.6 Semi-ionic C–F bond 94

2.2.7 Application to other conjugated carbon network materials 97

2.2.8 Stabilization of the Li metal anode surface using a pencil 111

2.3 Conclusion...115

2.4 Experimental details 117

2.5 References 127

Chapter 3 Lithiophilic Wetting Agent Inducing Interfacial Fluorination for Long-Lifespan Anode-Free Lithium Metal Batteries 134

3.1 Introduction 134

3.2 Experimental section 138

3.2.1 Characterization of the Ag-PCP wetting agent 138

3.2.2 Morphology of Li nucleation and growth....................................147

3.2.3 SEI Characterization of the Ag-PCP wetting agents....................152

3.2.4 Mechanism of interfacial fluorination 166

3.2.5 Electrochemical performances of asymmetric cells 171

3.2.6 Electrochemical performances of anode-free full cells 181

3.3 Conclusion 186

3.4 Experimental details 188

3.5 References 195

Chapter 4 Conclusion and Outlook 201

List of publications 204

요 약 (국문초록) 207

List of figures

Chapter 1

Figure 1.1 Working principle of Li-ion batteries.

Figure 1.2 Schematics illustration of configuration for Li-ion batteries, Li metal batteries, and anode-free Li metal batteries.

Figure 1.3 The mechanism of Li nucleation and growth.

Chapter 2

Figure 2.1 Raman spectroscopy of graphene.

Figure 2.2 TEM image of graphene and its selected area electron diffraction (SAED) pattern.

Figure 2.3 AFM image and height profile of graphene flake deposited on the Si-wafer.

Figure 2.4 Fabrication process of GAA.

Figure 2.5 FT-IR analysis.

Figure 2.6 Mechanical property of the aramid and the graphene-coated-aramid.

Figure 2.7 TEM image of the interface between aramid and graphene.

Figure 2.8 The solubility test of the graphene-coated-aramid side.

Figure 2.9 Galvanostatic cycling measurements of Li/Cu asymmetric cell (half-cell). Initialization process of (a) the reference system and (b) the GAA applied system. (c) Coulombic efficiency. (d) Time–voltage profiles.

Figure 2.10 Stepwise behavior of Li|Li symmetrical cell.

Figure 2.11 Galvanostatic cycling measurements. (a) Time–voltage profile for a Li|Li symmetrical cell of the reference system and the GAA applied system at a current density of 5 mA cm^{-2} (1 mAh cm^{-2}). (b) The ohmic potential drop of a Li|Li symmetrical cell with the GAA separator for 1000 cycles at a current density of 5 mA cm^{-2} (1 mAh cm^{-2}). Time–voltage profiles for a Li|Li symmetrical cell of the reference system and the GAA applied system (c) under rapid charge/discharge conditions (20 mA cm^{-2}, 1 mAh cm^{-2}), and (d) at a high areal capacity at high current density (20 mA cm^{-2}, 20 mAh cm^{-2}). (e) The entire time–voltage profile of Li metal batteries (Li/LFP) with the GAA separator. (f) Time–voltage profile of the mid-cycle-stage at a 20 C-rate (blue square of the (e) graph). (g) The cycling performance of Li metal batteries (Li/LFP) with the GAA separator and the uncoated aramid separator (the reference system) at a 20 C-rate (The N/P ratio is 30)

Figure 2.12 (a) Time–voltage profiles in initial stage (1 ~ 20th cycles). EIS data of (b) the reference system, (c) the GAA applied system.

Figure 2.13 Anodic polarization curves in Li|Li symmetrical cell test as the cycle progresses (5 mA $cm^{-2,}$ 1 mAh cm^{-2}).

Figure 2.14 Coulombic efficiency of Li metal batteries with GAA separators (sample) and without GAA separators (ref.).

Figure 2.15 The cycling performance of the flexible Li metal battery with the GAA separators in the repeated dimensional change (20 C-rate, bending radius: 20 mm).

Figure 2.16 Optophysical analysis. (a and b) C XPS data of the graphene-coated fiber side of the GAA separator before the cycles and after the cycles. P XPS data after the 1000 cycles at a current density of 5 mA cm^{-2} (1 mAh cm^{-2}) for (c) the reference system and (d) the GAA applied system, and (e) the bar graph comparing the residual electrolyte in the two systems. TOF-SIMS data of the stable SEI component on the Li metal anode surface for (f) the reference system and (g) the GAA applied system. (h) 3D depth mapping image comparing the stable SEI component in the two systems

Figure 2.17 F XPS data.

Figure 2.18 Microscopic FT-IR data of (a) the uncoated aramid fiber and (b) the graphene-coated aramid fiber after the 1000 cycles in the current density of 5 mA cm^{-2} (1 mAh cm^{-2}). (c and d) The enlarged graph from 1000 ~ 1400 $cm^{-2.}$

Figure 2.19 (a, b) TOF-SIMS depth profiles, (c) 3D depth mapping image.

Figure 2.20 Optical image of Li metal anode before and after the cycle (1000 times at the current density of 5 mA cm^{-2} (1 mAh cm^{-2})).

Figure 2.21 Electron microscopy image and energy dispersive X-ray spectroscopy data. The facial section images of the Li metal anode after the 1000 cycles at a current density of 5 mA cm^{-2} (1 mAh cm^{-2}) in (a and b) the reference system and (c and d)

the GAA applied system. The cross section image of (e) the bare Li metal, (f and g) the reference system and in the GAA applied system after the 1000 cycles at a current density of 5 mA cm^{-2} (1 mAh cm^{-2}). (h) The cross section image of the single graphene-coated-fiber after the cycles. The EDS mapping image of (i) C, (j) F, and (k) P in the sectional graphene-coated-fiber. (l) The enlarged image of the graphene-coating-layer, and (m) the EDS line data of the yellow line of the (l) image. (n) The enlarged image of the boundary between the graphene-coating-layer and the SEI layer on it, and (o) the EDS line data of the yellow line of the (n) image.

Figure 2.22 SEM facial image of the graphene-coated-fiber side as cycle progresses.

Figure 2.23 SEM oblique image of the graphene-coated-fiber side as cycle progresses.

Figure 2.24 Cross-section SEM image of the fiber and the enlarged boundary image.

Figure 2.25 SEM analysis. (a) The single fiber strand image. (b) EDS data and (c) EDS mapping images of the single fiber strand of GAA after the cycle.

Figure 2.26 The internal spacing measurement of graphene using by Cs-STEM.

Figure 2.27 Concept images. (a) The behavior of the Li metal anode in the reference system. (b) The expected mechanism of the Li metal anode in the GAA applied system.

Figure 2.28 (a, b) Galvanostatic cycling measurement: the time–voltage profiles for Li|Li symmetrical cells in different solvent system. (c) The ratio of LiF^{-} among TOF-SIMS data for the LMA surface of in different solvent system.

Figure 2.29 XPS data. (a) C XPS and (b) F XPS after F-doing process using HPF6 in water. (c) C XPS and (d) F XPS after the Li salts treatment.

Figure 2.30 Galvanostatic cycling measurements and P XPS data of the reference system and the activated carbon-, carbon black-, and graphene-coated fiber applied systems. (a and b) Time–voltage profiles for the Li|Li symmetrical cell at a current density of 5 mA cm^{-2} (1 mAh cm^{-2}). (c and d) The ohmic potential drop tendency of Li|Li symmetrical cells at a current density of 5 mA cm^{-2} (1 mAh cm^{-2}). (e) The cycling performance of Li metal batteries (Li/LFP) at a 20 C-rate. (f–i) P XPS data after the 1000 cycles at a current density of 5 mA cm^{-2} (1 mAh cm^{-2}).

Figure 2.31 Coulombic efficiency of Li metal batteries in the case of the other CCN materials being applied.

Figure 2.32 Optophysical analyses for other conjugated carbon network materials: graphene-, carbon black-, and activated carbon-coated applied systems. The C XPS data (a–c) before the cycles and (d–f) after the cycles. (g) Zeta-potential data of the intrinsic carbon materials. (h) XRD data of the intrinsic carbon materials. (i) TOF-SIMS data.

Figure 2.33 Particle size distribution of the carbon materials measured by dynamic light scattering spectrophotometer (DLS) after the grinding process; (a) Graphene. (b) Carbon black. (c) Activated carbon.

Figure 2.34 Li|Li symmetrical cell test at the high current density of 20 mA cm^{-2} (1 mAh cm^{-2}) in graphene, carbon black, and activated carbon applied system.

Figure 2.35 Life-span test.

Figure 2.36 Pencil application system. (a) An image of the pencil-drawn part on paper-mill-aramid and its depiction of the fluorination state through the F-doping mechanism. (b) Zeta-potential data of a charcoal pencil and a graphite pencil. (c) XRD data of a charcoal pencil and a graphite pencil. (d) Time–voltage profiles for Li|Li symmetrical cells. (e) The cycling performance of LFP full cells. (The N/P ratio is 30)

Figure 2.37 Coulombic efficiency of Li metal batteries in the case of the charcoal pencil and the graphite pencil applied.

Chapter 3

Figure 3.1 Characterization of the Ag-PCP wetting agent. The optical images of (a) PCP│Cu and (b) Ag-PCP│Cu. (c) Cu, (d) C, and (e) Ag EDS mapping images of the Ag-PCP│Cu cross-section. (f) The thickness of Ag-PCP wetting agent on Cu foil.

Figure 3.2 Characterization of PCP and Ag-PCP wetting agents. (a) XRD patterns of PCP wetting agents before (red) and after (blue) Ag treatment. 2D GIWAXS images of (b) PCP wetting agent and (c) Ag-PCP wetting agent. (d) Schematic of the differences between the PCP and Ag-PCP wetting agents in the extent of alignment and π-π stacking distance ($d_{(020)}$) of polymer chains.

Figure 3.3 1D GIWAXS profiles of pristine PCP and Ag-PCP. Q_{xy} value corresponds to the π–π stacking distance ($d_{(020)}$) of polymer chains.

Figure 3.4 (a) FT-IR spectra of PCP wetting agents before (red) and after (blue) Ag treatment in the wavenumber region of 600–1700 cm^{-1}. XPS profiles of (b) C 1s and (c) S 2p for pristine PCP (up) and Ag-PCP (down).

Figure 3.5 Li plating behavior on bare Cu, PCP|Cu, and Ag-PCP|Cu after Li deposition of 3 mAh cm^{-2} with a current density of 3 mA cm^{-2}. Top view SEM images at 1st and 300th cycle Li plating, Cross-sectional SEM images at 300th cycle, and FIB cross-section at 300th cycle of (a,b,g,h) bare Cu, (c,d,i,j) PCP|Cu, and (e,f,k,l) Ag-PCP|Cu.

Figure 3.6 Top view SEM images of (a) bare Cu, (b) PCP|Cu, and (c) Ag-PCP|Cu with their magnified views (inset).

Figure 3.7 Interfacial chemistry of bare Cu, pristine PCP|Cu, and Ag-PCP|Cu after cycling. (a) F 1s XPS depth profiles of SEI formed on the cycled (i) bare Cu, (ii) pristine PCP|Cu, and (iii) Ag-PCP|Cu after 300 cycles at a current density of 3 mA cm^{-2} (3 mAh cm^{-2}). (b) 3D chemical composition images from TOF-SIMS depth profiles of SEI formed on the cycled separators directly attached to bare Cu, pristine PCP|Cu, and Ag-PCP|Cu, respectively. (c) CV curves in the potential region of –0.05~1.8 V (vs Li^+/Li) at a scan rate of 0.2 mV s^{-1}. (d) TEM image of the cycled Ag-

PCP wetting agent and (e) EDS line data of yellow line in d image. The binding energies of F anion with (f) PCP wetting agent; C–F binding energy (up), S–F binding energy (down) or (g) Ag-PCP wetting agent; C–F binding energy (up), S–F binding energy (down) extracted from the DFT calculations.

Figure 3.8 C 1s XPS profiles of SEI formed on the cycled separators directly attached to (a) bare Cu, (b) PCP/Cu, and (c) Ag-PCP/Cu, respectively, after 300 cycles at a current density of 3 mA cm^{-2} (3 mAh cm^{-2}).

Figure 3.9 Li 1s XPS depth profiles of SEI formed on the cycled (a) bare Cu, (b) pristine PCP│Cu, and (c) Ag-PCP│Cu after 300 cycles at a current density of 3 mA cm^{-2} (3 mAh cm^{-2}).

Figure 3.10 Several element concentrations (Li, C, O, F, S, and N) from XPS depth profiles of SEI formed on the cycled (a) PCP│Cu and (b) Ag-PCP│Cu after 300 cycles at a current density of 3 mA cm^{-2} (3 mAh cm^{-2}).

Figure 3.11 The comparison of LiF^{-} ratio, a component of stable SEI, from TOF-SIMS depth profiles of SEI formed on the cycled separators directly attached to bare Cu, PCP│Cu, and Ag-PCP│Cu, respectively.

Figure 3.12 Cyclic voltammetry (CV) curves of (a) Ag-PCP│Cu, (b) PCP│Cu, and (c) Ag│Cu as working electrodes with Li metal as reference and counter electrodes in the potential region of –0.05~1.8 V (vs Li^{+}/Li) at a scan rate of 0.2 mV s^{-1}.

Figure 3.13 Schematic of Li plating behavior and the SEI formation mechanism (a) Bare Cu, (b) PCP│Cu, and (c) Ag-PCP│Cu.

Figure 3.14 Electrochemical performances of asymmetric cells (Li//bare Cu, Li//PCP│Cu, and Li//Ag-PCP│Cu). (a) Evaluation of Li nucleation overpotential; voltage profile of Li plating at a current density of 0.1 mA cm^{-2} (1 mAh cm^{-2}). (b) Evaluation of interfacial stability and Li plating/stripping reversibility; Voltage profile of the practical applicability test. During the initial five cycles, excess Li metal with a capacity of 3 mAh cm^{-2} was plated onto the bare Cu, PCP│Cu, and Ag-PCP│Cu, respectively. In subsequent cycles, all cells were cycled at a current density of 1 mA cm^{-2} with a capacity of 1 mAh cm^{-2}. (c-e) Voltage profiles of Li plating/stripping at a current density of 3 mA cm^{-2} (3 mAh cm^{-2}).

Figure 3.15 Li nucleation overpotential of asymmetric cells (Li//bare Cu, Li//PCP│Cu, and Li//Ag-PCP│Cu) at different current densities ranging from 0.1 to 3 mA cm^{-2}.

Figure 3.16 Voltage-time profiles at current density of 0.5 mA cm^{-2} for 1 mAh cm^{-2} Li deposition and then Li stripping to 0.3 V. The magnified images show voltage polarization of the bare Cu, PCP│Cu, and Ag-PCP│Cu, respectively.

Figure 3.17 Aurbach CE test

Figure 3.18 (a) Voltage profiles of Li plating/stripping at a current density of 3 mA

cm^{-2} (3 mAh cm^{-2}) in the 1st cycle. (b) XRD patterns of the Ag-PCP│Cu showing the Ag-Li alloying/dealloying. (c) CV curve of Ag-PCP│Cu and Ag│Cu as working electrodes with Li metal as reference and counter electrodes in the potential region of - 0.05 ~ 1.8 V (vs Li^{+}/Li) at a scan rate of 0.2 mV s^{-1}.

Figure 3.19 The rate performance of asymmetric cells (Li//bare Cu, Li//PCP│Cu, and Li//Ag-PCP│Cu).

Figure 3.20 Nyquist plots of (a) LFP//bare Cu, (b) LFP//PCP│Cu, and (c) LFP//Ag-PCP│Cu full cells before and after 10 cycles at 1 C-rate.

Figure 3.21 Electrochemical performances of LFP full cells (LFP//bare Cu, LFP//PCP│Cu, and LFP//Ag-PCP│Cu) at 1 C-rate. (a) Voltage profiles of Li plating/stripping at the 1st cycle. (b) Cycling performance of LFP//PCP│Cu (red) and LFP//Ag-PCP│Cu (blue) full cells. Voltage profiles of Li plating/stripping at the 2nd, 10th, 50th, 100th, and 200th cycles; (c) LFP//bare Cu, (d) LFP//PCP│Cu, and (e) LFP//Ag-PCP│Cu.

Figure 3.22 Cycling performance of LFP//bare Cu full cell.

Chapter 1 Introduction

1.1 Overview

Li-ion batteries (LIBs) are the most widely used energy storage technologies for mobile phones, electric vehicles, and large-scale energy storage systems. [1] However, commercial LIBs composed of graphite anodes operate based on Li-ion intercalation chemistry and thus have limitations in increasing energy density. [2] In terms of increasing energy density, Li metal-based batteries show great potential by using the ideal Li metal anodes (LMAs), which can achieve energy density exceeding 500 Wh kg^{-1} at the cell level than that of the commercial LIBs (less than 250 Wh kg^{-1}). [3,4] In other words, this is closely related to miniaturization and the long operating time of the devices. However, Li metal-based batteries suffer from unwanted side reactions at the anode/electrolyte interface, such as Li dendrite growth and the continual formation of unstable solid electrolyte interphase (SEI) layer. [5] As a result, their actual utilizations have been hindered by low coulombic efficiency and rapid capacity fading. [6] Recently, various studies have been devoted to improving the cycling stability of Li metal-based batteries, such as electrolyte additives, 3D frameworks, and artificial SEI. [7–9] Although these strategies presents a considerable effect to suppress the interfacial side reactions, the fundamental understanding how the interfacial stabilization strategies affect Li nucleation, growth, and the SEI formation is limited. Understanding the stabilization mechanisms is necessary to efficiently regulate Li plating behavior and the SEI chemistry in the repeated cycling.

This dissertation proposes fluorinated interfacial engineering without additional treatment of electrode or electrolyte additives for Li metal-based batteries with high cycling performance. Also, it has the advantage of applying to the current system due to simple fabrication processes. Notably, I uncover a correlation between interfacial fluorination mechanism and conjugated structures to efficiently achieve a favorable SEI chemistry. The stabilization mechanism of the LMAs is identified and discussed on a carbon-coated separator with sp^2 π conjugation electron system, particularly fluorinated metathesis of conjugated carbon network (CCN) materials, such as graphene, carbon black, and activated carbon in Chapter 2. [10] In Chapter 3, for anode-free Li metal batteries (AFLMBs), the formation mechanism of LiF-rich SEI is investigated through interfacial fluorination induced by a silver nanoparticles incorporated p-doped conjugated polymer (Ag-PCP) wetting agent on the copper current collector. [11] Finally, Chapter 4 reports the effectiveness of these methods for high-energy-density Li metal-based batteries, together with the comprehensive conclusion of this dissertation.

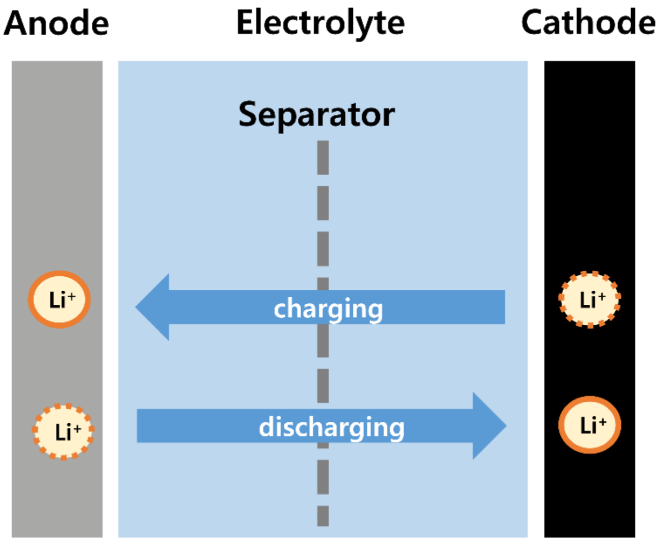

Figure 1.1 Working principle of Li-ion batteries.

1.2 Fundamental and literature review

1.1.1 Background on Li metal-based batteries

The need for beyond LIBs technologies has been promoted by increasing their applications over the existing electronics market. Among various beyond-LIBs, Li metal-based batteries, including LMBs and AFLMBs arouse attention as next-generation systems to increase energy density. [2] Unlike conventional LIBs with a low theoretical capacity of graphite anodes (372 mAh g^{-1}), Li metal possesses a high theoretical capacity (3862 mAh g^{-1}), the lowest redox potential (-3.04 V vs. standard hydrogen electrode), and low gravimetric density (0.534 g cm^{-1}). [12] In this regard, AFLMBs without excess Li inventory are the ultimate system to achieve the maximum possible energy density compared to all conventional LIBs, in which all the active Li sources are stored in the cathode. [3] In anode-free cell configuration, Li ions extracted from the cathode are plated on the copper current collector during the charging process, and are stripped from the formed in-situ Li metal anode to return the cathode during the discharging process. [4] Thus, it significantly reduces weight and volume of the overall cell. In addition, this system has the advantage of simplifying manufacturing procedures and greatly reducing production costs due to the absence of anodes. [13] Based on all these above advantages, two types of Li metal-based batteries suggest next-generation rechargeable batteries as energy storage technologies with high energy density.

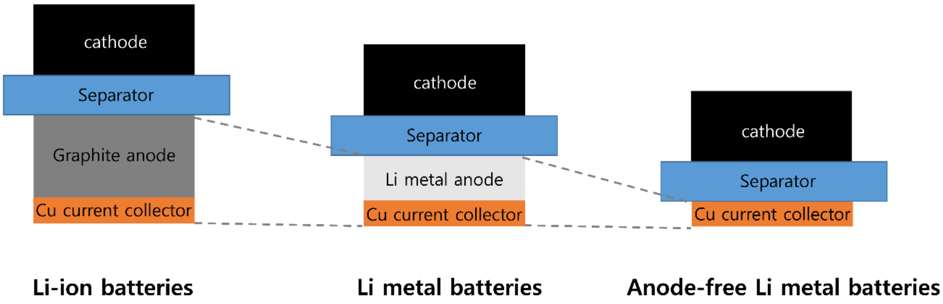

Figure 1.2 Schematics illustration of configuration for Li-ion batteries, Li metal batteries, and anode-free Li metal batteries.

1.1.2 Challenges of Li metal-based batteries

Li metal is regarded as an ideal anode for high-energy-density batteries. [6,9] However, its actual applications have enormous obstacles to be addressed. First, Li metal in the alkali metal group has high chemical/electrochemical reactivity. [14,15] Due to intrinsic properties of Li metal, an undesirable side reaction between active Li ions and the liquid electrolyte continuously occurs during charging/discharging processes, which promotes Li dendrite growth and thick SEI formation. [5,16–18] Second, since Li metal is a “hostless” anode, large volume changes are inevitable during the electrochemical plating/stripping process, resulting in the fracture of the unstable SEI layer and the successive decomposition the liquid electrolyte with active Li. [13,19–21] In AFLMBs, these fatal factors are more critical due to without excess Li inventory to compensate for irreversible loss of active Li. [3,22–24] Besides the problems mentioned above, in AFLMBs, one of the huge challenges is inhomogeneous Li nucleation caused by “lithiophobic” property of the copper current collector where the initial Li ions are plated, thereby large nucleation overpotential. [25–28] Therefore, the fundamental understating of interfacial issues is essential for improving the cycling performances of Li metal-based batteries.

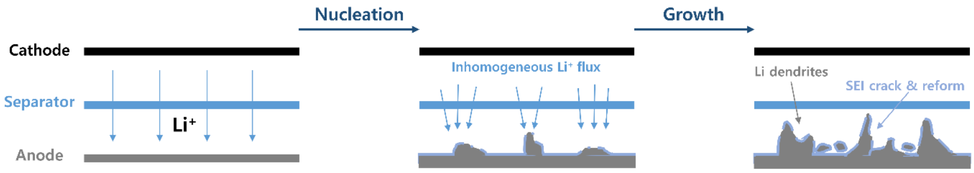

Figure 1.3 The mechanism of Li nucleation and growth.

1.1.3 Main strategies for Li metal-based batteries

Many studies have been reported to alleviate anode/electrolyte interfacial issues. Detailed strategies are as below:

(1) Modification of the liquid electrolyte: the reduction pathway of the liquid electrolyte is an important factor in determining the SEI component as well as Li deposition morphology on the Li metal surface. At this time, when the SEI layer is formed by the reduction of salt anions instead of solvent decomposition, it means that stable and robust SEI is formed. Therefore, this SEI layer is rendered by adding electrolyte additives as well as adjusting solvent composition or salt anion concentration. [7,29–33]

(2) 3D matrix as anode host: the introduction of a 3D matrix host with free volume can accommodate a large amount of active Li during electrochemical cycling, thereby mitigating the consumption of the liquid electrolyte and active Li. In addition, it induces low local current density and homogeneous Li-ion flux on the anode surface, resulting in the suppression of Li dendrite growth. [33–37]

(3) Artificial SEI: the ideal SEI well operates the role of the passivation layer against the continuous side reaction between the liquid electrolyte and Li ions

during the Li plating/stripping processes. The inorganic artificial SEI with a high ratio of fluorine facilitates Li ions transfer. Also, the organic artificial SEI with lithiophilic functional groups achieves uniform and flat Li deposition morphologies. [19,38–41]

For designing favorable interface properties, I introduce the advantages of the previously proposed systems and strengthen the interfacial understanding of Li metal-based batteries.

In Chapter 2, I apply a functional carbon-coated separator on the Li metal anode. This system suppresses dendritic Li growth by using the randomly woven architecture of aramid fibers with high modulus and forms a stable SEI layer by inducing fluorine doping reaction on carbon materials. In Chapter 3, I fabricate a silver nanoparticles incorporated p-doped conjugated polymer (Ag-PCP) wetting agent on the copper current collector. [10,11] This strategy regulates homogeneous Li deposition by employing a lithiophilic material and achieves the formation of LiF-rich SEI at the early stage *via* the interfacial fluorination.

These proposed systems ensure enhanced interfacial stability in Li metal-based batteries, remarkably the formation of LiF-rich SEI and dendrite-free Li morphology even under harsh conditions. Also, I introduce simple fabrication and demonstrate the mechanism of interfacial fluorination induced by conjugated structures. Therefore, these strategies are attractive to a wide range of applications for interfacial stabilization in other energy storage systems.

1.3 References

[1] M. Armand, *Nature* **2001**, *414*, 359.

[2] J. Xiao, Q. Li, Y. Bi, M. Cai, B. Dunn, T. Glossmann, J. Liu, T. Osaka, R. Sugiura, B. Wu, J. Yang, J. G. Zhang, M. S. Whittingham, *Nat. Energy* **2020**, *5*, 561.

[3] Y. Tian, Y. An, C. Wei, H. Jiang, S. Xiong, J. Feng, Y. Qian, *Nano Energy* **2020**, *78*, 105344.

[4] S. Nanda, A. Gupta, A. Manthiram, *Adv. Energy Mater.* **2021**, *11*, 1.

[5] B. Liu, J. G. Zhang, W. Xu, *Joule* **2018**, *2*, 833.

[6] A. Shao, X. Tang, M. Zhang, M. Bai, Y. Ma, *Adv. Energy Sustain. Res.* **2022**, *3*, 2100197.

[7] J. Fu, X. Ji, J. Chen, L. Chen, X. Fan, D. Mu, C. Wang, *Adv. Mater.* **2020**, *132*, 22378.

[8] C. P. Yang, Y. X. Yin, S. F. Zhang, N. W. Li, Y. G. Guo, *Nat. Commun.* **2015**, *6*, 1.

[9] X. Liang, Q. Pang, I. R. Kochetkov, M. S. Sempere, H. Huang, X. Sun, L. F. Nazar, *Nat. Energy* **2017**, *2*, 1.

[10] Y. J. Gong, S. Pyo, H. Kim, J. Cho, H. Yun, H. Kim, S. Ryu, J. Yoo, Y. S. Kim, *Energy Environ. Sci.* **2021**, *14*, 940.

[11] S. Pyo, S. Ryu, Y. J. Gong, J. Cho, H. Yun, H. Kim, J. Lee, B. Min, Y. Choi, J.

Yoo, Y. S. Kim, *Adv. Energy Mater.* **2023**, *13*, 1.

[12] Z. Xie, Z. Wu, X. An, X. Yue, J. Wang, A. Abudula, G. Guan, *Energy Storage Mater.* **2020**, *32*, 386.

[13] W. Chen, R. V. Salvatierra, M. Ren, J. Chen, M. G. Stanford, J. M. Tour, *Adv. Mater.* **2020**, *32*, 1.

[14] A. Wang, S. Kadam, H. Li, S. Shi, Y. Qi, *npj Comput. Mater.* **2018**, *4*, 1.

[15] Q. Li, H. Pan, W. Li, Y. Wang, J. Wang, J. Zheng, X. Yu, H. Li, L. Chen, *ACS Energy Lett.* **2018**, *3*, 2259.

[16] C. J. Huang, B. Thirumalraj, H. C. Tao, K. N. Shitaw, H. Sutiono, T. T. Hagos, T. T. Beyene, L. M. Kuo, C. C. Wang, S. H. Wu, W. N. Su, B. J. Hwang, *Nat. Commun.* **2021**, *12*, 1.

[17] K. Zou, W. Deng, P. Cai, X. Deng, B. Wang, C. Liu, J. Li, H. Hou, G. Zou, X. Ji, *Adv. Funct. Mater.* **2021**, *31*, 1.

[18] A. Pei, G. Zheng, F. Shi, Y. Li, Y. Cui, *Nano Lett.* **2017**, *17*, 1132.

[19] Y. J. Gong, J. W. Heo, H. Lee, H. Kim, J. Cho, S. Pyo, H. Yun, H. Kim, S. Y. Park, J. Yoo, Y. S. Kim, *Adv. Energy Mater.* **2020**, *10*, 1.

[20] J. Song, H. Lee, M. J. Choo, J. K. Park, H. T. Kim, *Sci. Rep.* **2015**, *5*, 1.

[21] J. Qian, W. A. Henderson, W. Xu, P. Bhattacharya, M. Engelhard, O. Borodin, J. G. Zhang, *Nat. Commun.* **2015**, *6*, 1.

[22] L. Lin, L. Suo, Y. sheng Hu, H. Li, X. Huang, L. Chen, *Adv. Energy Mater.* **2021**, *11*, 1.

[23] T. T. Beyene, B. A. Jote, Z. T. Wondimkun, B. W. Olbassa, C. J. Huang, B. Thirumalraj, C. H. Wang, W. N. Su, H. Dai, B. J. Hwang, *ACS Appl. Mater. Interfaces* **2019**, *11*, 31962.

[24] Z. T. Wondimkun, W. A. Tegegne, J. Shi-Kai, C. J. Huang, N. A. Sahalie, M. A. Weret, J. Y. Hsu, P. L. Hsieh, Y. S. Huang, S. H. Wu, W. N. Su, B. J. Hwang, *Energy Storage Mater.* **2021**, *35*, 334.

[25] S. H. Wang, J. Yue, W. Dong, T. T. Zuo, J. Y. Li, X. Liu, X. D. Zhang, L. Liu, J. L. Shi, Y. X. Yin, Y. G. Guo, *Nat. Commun.* **2019**, *10*, 1.

[26] L. Jin, H. Zhang, S. Li, S. Lei, M. Liu, Z. Zeng, C. Yu, S. Cheng, J. Xie, *ACS Appl. Mater. Interfaces* **2021**, *13*, 38425.

[27] R. Zhang, X. R. Chen, X. Chen, X. B. Cheng, X. Q. Zhang, C. Yan, Q. Zhang, *Angew. Chemie - Int. Ed.* **2017**, *56*, 7764.

[28] B. Horstmann, J. Shi, R. Amine, M. Werres, X. He, H. Jia, F. Hausen, I. Cekic-Laskovic, S. Wiemers-Meyer, J. Lopez, D. Galvez-Aranda, F. Baakes, D. Bresser, C. C. Su, Y. Xu, W. Xu, P. Jakes, R. A. Eichel, E. Figgemeier, U. Krewer, J. M. Seminario, P. B. Balbuena, C. Wang, S. Passerini, Y. Shao-Horn, M. Winter, K. Amine, R. Kostecki, A. Latz, *Energy Environ. Sci.* **2021**, *14*, 5289.

[29] S. Chen, J. Zheng, D. Mei, K. S. Han, M. H. Engelhard, W. Zhao, W. Xu, J. Liu, J. G. Zhang, *Adv. Mater.* **2018**, *30*, 1.

[30] J. Zheng, P. Yan, D. H. Mei, M. H. Engelhard, S. S. Cartmell, B. J. Polzin, C. M. Wang, J. G. Zhang, W. Xu, *Adv. Energy Mater.* **2016**, *6*, 1.

[31] J. Zheng, J. A. Lochala, A. Kwok, Z. D. Deng, J. Xiao, *Adv. Sci.* **2017**, *4*, 1.

[32] T. Li, X. Q. Zhang, P. Shi, Q. Zhang, *Joule* **2019**, *3*, 2647.

[33] Y. Liu, D. Lin, Y. Jin, K. Liu, X. Tao, Q. Zhang, X. Zhang, Y. Cui, *Sci. Adv.* **2017**, *3*, 1.

[34] C. Jin, O. Sheng, J. Luo, H. Yuan, C. Fang, W. Zhang, H. Huang, Y. Gan, Y. Xia, C. Liang, J. Zhang, X. Tao, *Nano Energy* **2017**, *37*, 177.

[35] S. Huang, H. Yang, J. Hu, Y. Liu, K. Wang, H. Peng, H. Zhang, L. Z. Fan, *Small* **2019**, *15*, 32.

[36] R. Zhang, X. Chen, X. Shen, X. Q. Zhang, X. R. Chen, X. B. Cheng, C. Yan, C. Z. Zhao, Q. Zhang, *Joule* **2018**, *2*, 764.

[37] H. Zhao, D. Lei, Y. B. He, Y. Yuan, Q. Yun, B. Ni, W. Lv, B. Li, Q. H. Yang, F. Kang, J. Lu, *Adv. Energy Mater.* **2018**, *8*, 1.

[38] H. Kim, Y. S. Kim, J. Yoo, *Sustain. Energy Fuels* **2020**, *4*, 522.

[39] J. Qian, Y. Li, M. Zhang, R. Luo, F. Wang, Y. Ye, Y. Xing, W. Li, W. Qu, L. Wang, L. Li, Y. Li, F. Wu, R. Chen, *Nano Energy* **2019**, *60*, 866.

[40] P. Li, W. Feng, X. Dong, Y. Wang, Y. Xia, *Adv. Mater. Interfaces* **2020**, *7*, 1.

[41] Q. Xu, X. Yang, M. Rao, D. Lin, K. Yan, R. A. Du, J. Xu, Y. Zhang, D. Ye, S. Yang, G. Zhou, Y. Lu, Y. Qiu, *Energy Storage Mater.* **2020**, *26*, 73.

Chapter 2 Advanced Li metal anode by fluorinated metathesis on conjugated carbon networks

2.1 Introduction

Li metal has drawn increasing attention from the energy field as among the best anode materials for next-generation LIBs due to its high theoretical specific capacity (3862 mAh g^{-1}) and low redox potential [−3.04 V (vs. a standard hydrogen electrode)]. [1] Despite continuous efforts to introduce Li metal as a LIBs anode, issues related to cycle characteristics, such as rate capability and lifespan, remain obstacles, and must be addressed. The root cause of these issues lies in the unstable SEI formed on the Li metal anode (LMA) surface by the reaction of Li metal and an electrolyte. [2] During charging/discharging, LMA utilizes a lithiation–delithiation mechanism (hostless electrochemical plating/stripping) at its surface. During this process and due to the high reactivity of Li, an unstable SEI repeatedly forms and collapses on its surface accompanied by considerable electrolyte consumption and significant dimensional expansion that degrades the anode properties of Li. [3] Thus, as the cycle progresses, perpetual occurrence of this undesirable interfacial reaction leads to accumulation of an electrochemically inactive layer, dendritic growth, and electrically isolated Li at the LMA surface, thereby deteriorating the cycle characteristics of LMA until cell failure or a stability problem occurs. [4] Moreover, because these side effects further accelerate and worsen as the applied current increases, LMA can operate only within a limited number of cycles at high current density; therefore, studying the interfacial phenomena of the LMA is essential for its application as a LIBs anode. [5] Various strategies to stabilize the LMA surface have been attempted (i.e., dendrite-suppressing layers, electrolyte additives, and a modified Li metal surface). [6–8] Among these, studies regarding a functional separator to allow chemically stable SEI formation have provided excellent results by controlling the undesirable interfacial reaction between the LMA and electrolyte and with the advantage of not requiring additives, additional treatments, or a modified Li metal surface. [5,9–14] Specifically, this approach has been widely expanded by using carbon-based materials (graphite or graphene-family materials), which are light and advantageous in terms of the energy density of the entire cell. Additionally, their chemical stability and high conductivity make them suitable as an interlayer or a passivation layer for stabilizing the interface between the LMA and electrolyte. [15–19] When the conductive structure is placed above the LMA as an interlayer between LMA and separator or when a conductive aspect of the functional separator is in contact with the LMA, the conductive structure at the top structurally meets the Li^+ ion flux first during the plating step; therefore, this results in formation of an SEI with different composition on the conductive frame, thereby maintaining LMA interfacial stability. [12-15]

The present study researched the use of functional separators to support the formation of chemically stable SEI, with a specific focus on fluorinated metathesis of conductive CCN materials to induce a stable SEI *via* LiF formation. LiF is a key component of stable SEI, has a wide electrochemical-stability window, and can improve the surface diffusion of ions, leading to denser and smoother Li^+ plating. [14,20,21] Here, I selected graphene as the conductive CCN material and used it to coat paper-mill-aramid, in which aramid fibers with high modulus were woven into each other, by a simple paste-painting process. In the proposed system, the CCN in the graphene-coated layer induces LiF formation as a stable SEI component *via* fluorinated metathesis (as a novel F-doping mechanism): F^- anion formed by $LiPF_6$ electrolyte decomposition in the specific solvent environment (polar, compact, and with a high dielectric constant) reacted with the sp^2 C of the CCN in graphene to generate semi-ionic C–F bonds, resulting in a partially fluorinated graphene-coated layer (the F-doped state). These chemically labile semi-ionic C–F bonds induce LiF during the Li^+ ion plating process. As a result, the graphene-coated paper-mill-aramid acts as a conductive frame to form stable SEI with large amounts of LiF along its surface, thereby maintaining the cycle characteristics of LMA, even under rapid charge/discharge conditions (20 mA cm^{-2} and 1 mAh cm^{-2}), as well as at a high current density and high areal capacity (20 mA cm^{-2} and 20 mAh cm^{-2}). [22–25] Furthermore, a Li/$LiFePO_4$ (LFP) cell with the proposed system retained 82.13% of its initial capacity after 1000 cycles at a high 20 C-rate, thereby demonstrating low capacity fading.

I then generalized the applicability of this F-doping mechanism to other CCN materials, such as carbon black (CB) and activated carbon (AC). As shown in the electrochemical test results and optophysical analyses, LMA surface stabilization was also achieved when other CCN materials were coated on the paper-mill-aramid, although the results differed according to carbon type. In the case of graphene as a complete lattice structure comprising pure carbon, the F-doping mechanism *via* the reaction of F^{-} anion and sp^2 C occurred easily, resulting in a high LiF formation rate. However, this inferred that the higher degree of electrically negative functionality and disordered lattice present in the CCN materials would result in greater hindrance of bonding between the F^{-} anion and sp^2 C, thereby reducing LiF formation. I found that the CCN materials could induce the formation of LiF as a stable SEI component in a specific solvent environment and stabilize the LMA surface, but that the stabilization effect was dependent on the negative functional groups on the CCN materials and the resulting structural completeness. Finally, based on this generalized correlation between CCN materials and the F-doping mechanism, I proposed a simple, effective, and cheap pencil method for LMA surface stabilization.

2.2 Experimental section

2.2.1 Fabrication process

As a representative CCN material, graphene was used to fabricate the functional separators. Detailed information on the structures of graphene used in this experiment was obtained using Raman spectroscopy, transmission electron microscopy (TEM), and atomic force microscopy (AFM) (Figure 2.1, Figure 2.2, and Figure 2.3). As a conductive CCN, graphene has a complete lattice structure comprised of pure carbon. The fabrication process of the graphene-coated aramid attached to the uncoated aramid (GAA) separator is described in detail in the experimental details and Figure 2.4. Appropriate quantities of graphene powder and phenol resin (PR) were mixed, and the resulting high viscosity mixture was diluted in 3-methoxy-3-methyl-1-butanol. The as-prepared graphene paste was then painted with a brush on paper-mill-aramid, followed by drying at 150 °C for 8 h. After drying, the graphene-coated surface on aramid fibers was confirmed through Fourier transform infrared (FT-IR) analysis (Figure 2.5). The graphene-coated paper-mill aramid was then attached to the uncoated paper-mill-aramid under 30 MPa at 50 °C for 1 h using acetone and ethanol to obtain the GAA separator (thickness: 40 ± 2 mm; and weight: 1.1726 ± 0.1 mg cm^{-}

^{2}). The weight of deposited graphene per unit area was 0.0505 ± 0.1 mg cm^{-2}. In the GAA separator, the side with the graphene-coated aramid fibers was the functional part and acted as the conductive frame for stable SEI formation *via* fluorinated metathesis (the F-doping mechanism), whereas the side with the uncoated aramid fibers served as the separator.

During the fabrication process, the painting method simply spreads the paste on the frame to provide a platform that allows easy formation of a coating layer of various carbon materials on the fibers. Additionally, this technique ensures that coating the graphene layer, which can host the F-doping mechanism, on the woven fiber structure with a modulus of ≥ 6 GPa can form a stable SEI through the F-doping mechanism and simultaneously help the fiber structure suppress dendritic growth *via* its high modulus. [5,26,27] This suggests that the painting method can provide a platform that allows LMA surface stabilization *via* the F-doping mechanism involving various carbon materials, as well as chemical stabilization of the selected structure with high modulus. Therefore, I used paper-mill-aramid as a frame with high modulus (Figure 2.6) and exhibiting the following tensile strength and Young’s modulus: uncoated aramid, 2.6 GPa and 142.9 GPa (with a corresponding elongation of 5.9%), respectively; and GAA, 3.0 GPa and 54.4 GPa (with a corresponding elongation of ~4.9%), respectively.

Paper-mill-aramid has several additional advantages. With respect to graphene, when other materials form covalent bonds with graphene, there are considerable disadvantages due to disrupting its conjugated electron system as well as impairing its physical and electrical properties. [28] Therefore, π-π stacking interactions, which usually occur between two relatively nonpolar aromatic rings with overlapping π orbitals, can be a good alternative to covalent bonding as noncovalent functionalization of a graphene sheet by using aromatic organic molecules. [29] As a component of paper-mill-aramid, aramid polymers, which have a relatively linear nature and a high degree of aromaticity, stabilize the graphene sheet through π-π interactions without disrupting the electronic conjugation of graphene. [30] Similarly, graphene sheets also have advantages of π-π interactions with the aramid polymer *via* its graphitized basal plane structure because this interaction does not induce exfoliation. [31] Therefore, the interface between the aramid polymer and graphene is stabilized by π-π interactions without destroying the electronic π-system of graphene. The TEM image presents the boundary between graphene and aramid (Figure 2.7). As revealed by the TEM image, phenomena such as the nanostructure variation of graphene by aramid or the exfoliation of the graphene coating layer cannot be found at the boundary of aramid and graphene. Furthermore, the TEM image showed that there is no change in the lattice structure of graphene caused by the hetero-atom doping of graphene by the functional group of aramid, which is often a concern at the interface between graphene and other functional groups.

In addition, because the aramid functional group [–C(=O)– N(–H)–] shows good adhesion with paste containing PR, the coating layer did not melt into a liquid electrolyte, and the graphene flakes (or other carbon particles) were unable to escape (Figure 2.8). Moreover, the woven fiber structure of paper-mill-aramid has a high surface area that provides sufficient host sites for the F-doping mechanism. Additionally, the structure of paper-mill-aramid provides reasonable ionic conductivity after coating (uncoated aramid separator, 4.88115 mS cm^{-1} vs. the GAA separator, 4.59253 mS cm^{-1}). Furthermore, the resistance of the side with the graphene-coated fiber was ~25 Ω cm^{-2} according to the sheet-resistance measurement using Van der Paw's law, indicating a good conductive frame. [32] As a separator, paper-mill-aramid has high porosity and good thermal resistance. [33] Therefore, application of the GAA separator fabricated using the painting method as the reaction host for the F-doping mechanism can induce stable SEI formation. Concurrently, its high modulus helps prevent dendritic growth and offers good ionic conductivity and a conductive frame.

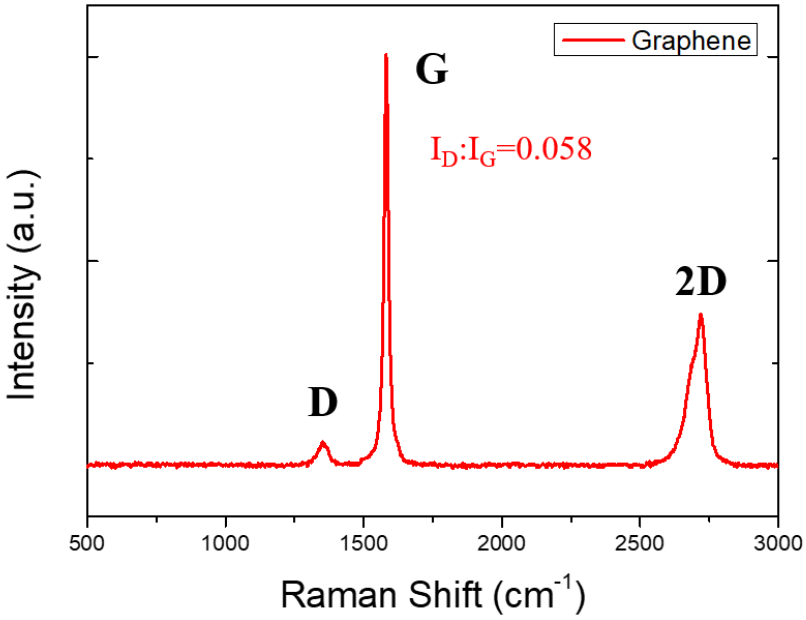

Figure 2.1 Raman spectroscopy of graphene. Raman spectroscopy clearly reveals the highly ordered nature of graphene, showing an I_D/I_G ratio of 0.058 and its sharp 2D peak. [34]

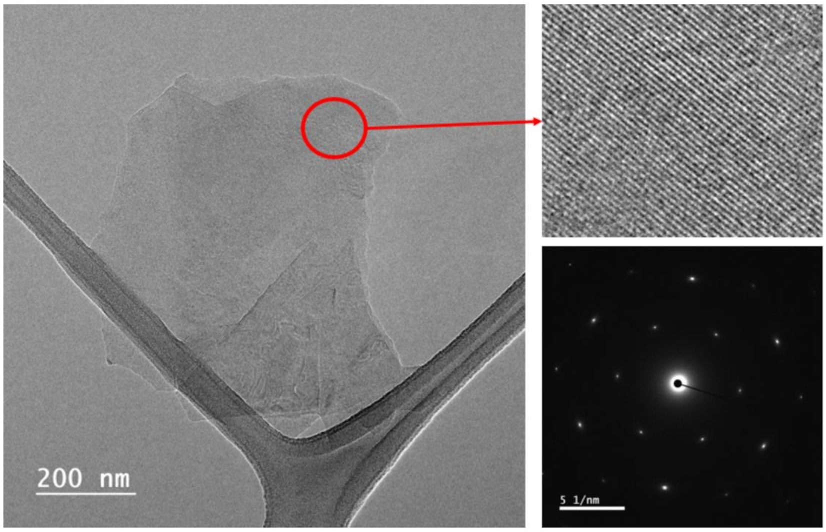

Figure 2.2 TEM image of graphene and its selected area electron diffraction (SAED) pattern.

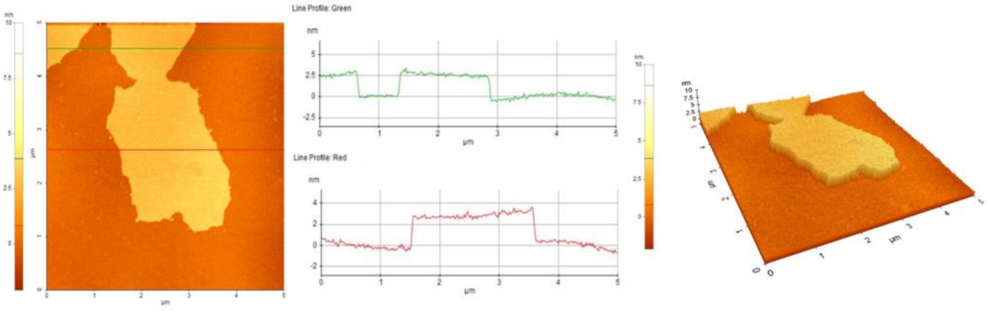

Figure 2.3 AFM image and height profile of graphene flake deposited on the Si-wafer.

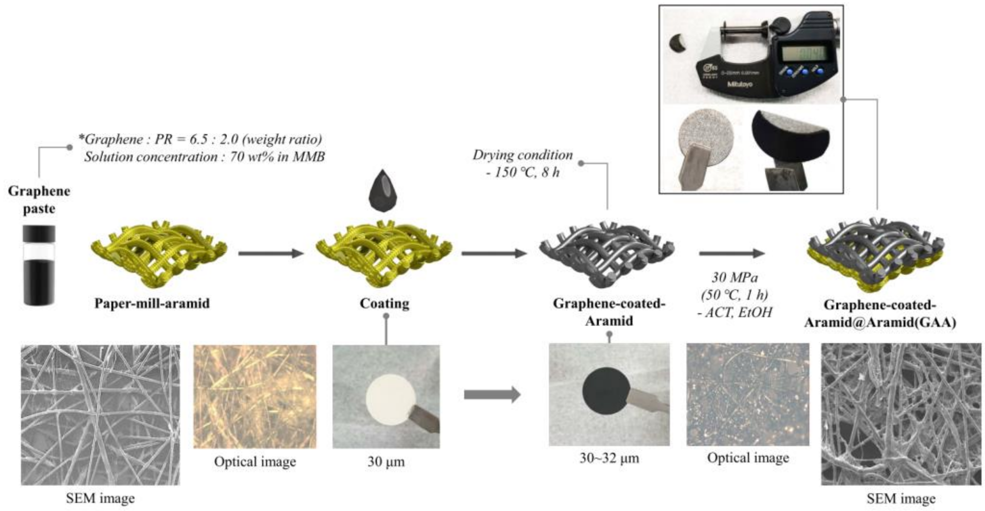

Figure 2.4 Fabrication process of GAA.

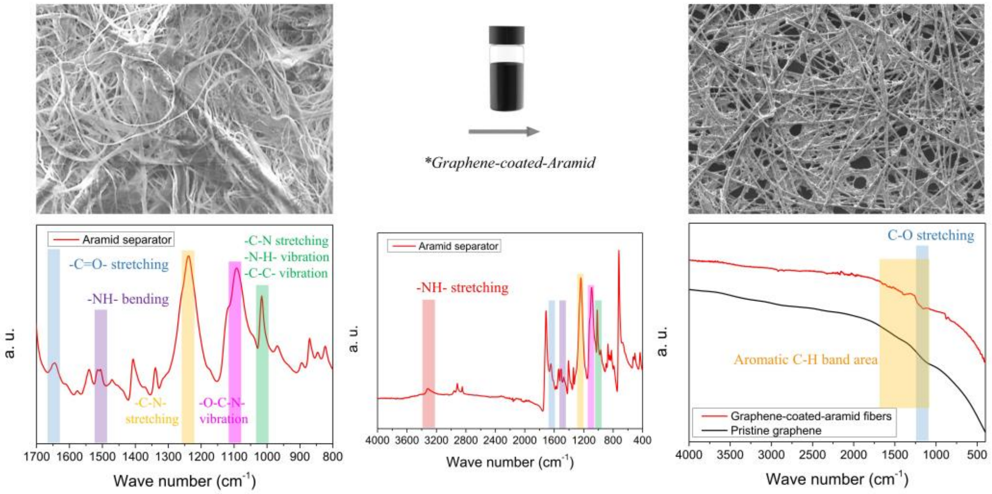

Figure 2.5 FT-IR analysis. Before the graphene paste coating, the typical aramid peaks (–C(=O)–N(–H)–) appears from 800 cm^{-1} to 1700 cm^{-1} and at 3300 cm^{-1}. After the graphene paste coating, the aramid peaks did not appear, and the spectrum similar to pristine graphene was observed in GAA (C−O peaks was shown by PR resin). [35–39]

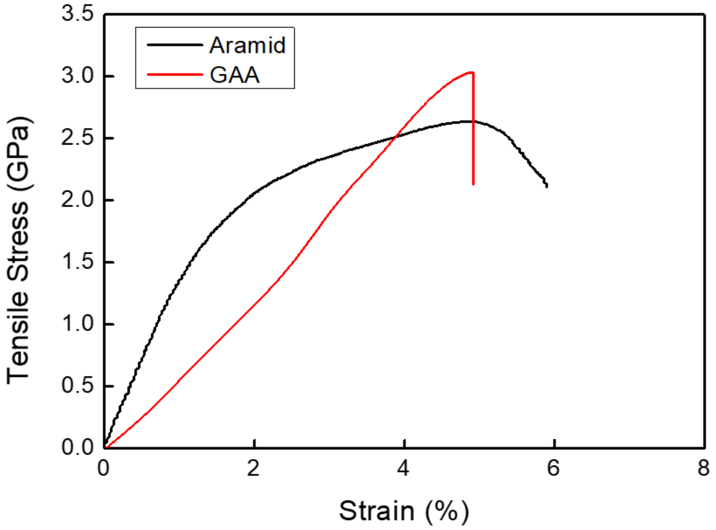

Figure 2.6 Mechanical property of the aramid and the graphene-coated-aramid.

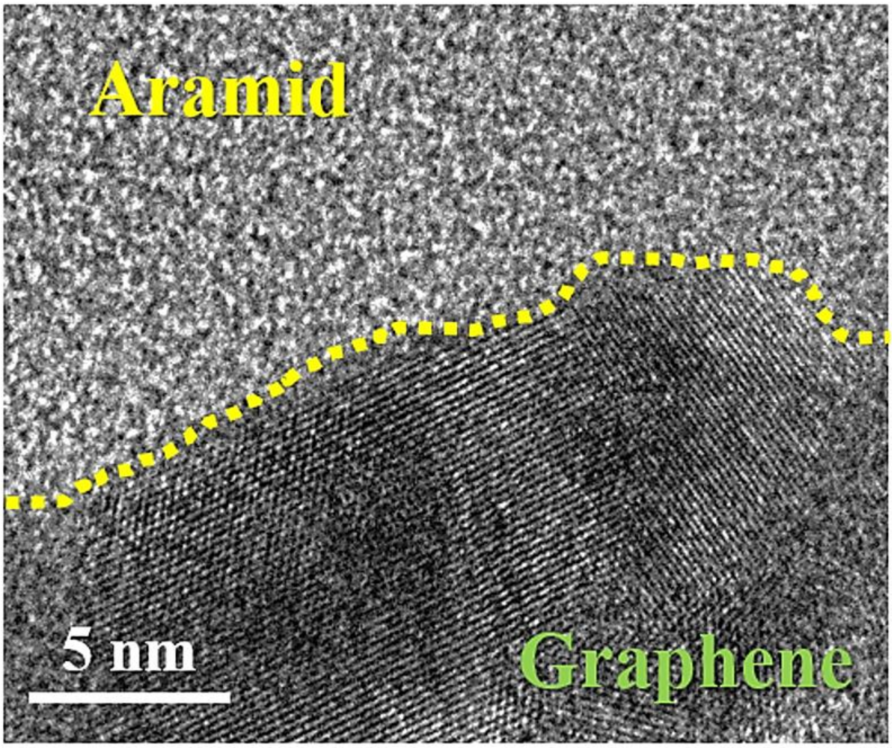

Figure 2.7 TEM image of the interface between aramid and graphene.

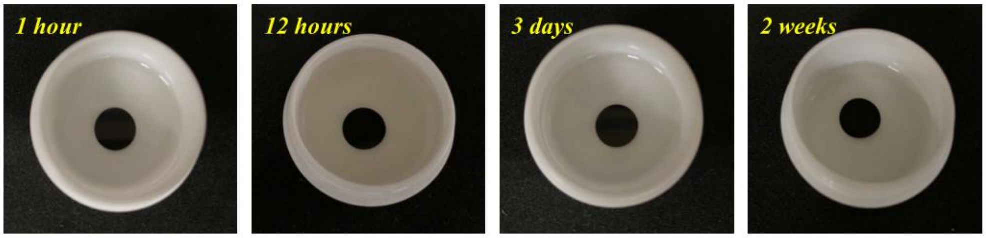

Figure 2.8 The solubility test of the graphene-coated-aramid side.

2.2.2 Galvanostatic cycling measurements

To evaluate the LMA performance without cathode coupling, Li|Li symmetrical cells provided information about the LMA surface stability according to the drops in the ohmic potential and anodic polarization curves during the continuous plating/ stripping process in time–voltage profiles. [40–42] Prior to the cycling measurements of the Li|Li symmetrical cell tests, the effect of the GAA architecture on the cell performance was assessed in a half-cell system, which included no Li reservoir on one end (Li/Cu) (Figure 2.9). [43] Then, galvanostatic cycling measurements of Li|Li symmetrical cells were performed at a current density of 5 mA cm^{-2} (1 mAh cm^{-2}) and a high current density corresponding to the rapid charge/discharge condition (a current density of 20 mA cm^{-2} and 1 mAh cm^{-2}). I performed an additional cell test at a high current density and high areal capacity (20 mA cm^{-2} and 20 mAh cm^{-2}). [22-25] As the Li|Li symmetrical cell, the reference system and the GAA applied system constituted the structure [reference system: Li/aramid/Li (black); and the GAA applied system: Li/graphene-coated fibers/aramid/graphene-coated fibers/Li (red)]. When current was applied, the LMA of the symmetrical cell corresponding to the reference system exhibited a stepwise behavior as described in Figure 2.10 and shown in Figure 2.11a. Electrochemical impedance spectroscopy (EIS) to evaluate the SEI formation in the initial stage also supported the results of symmetrical cell tests (Figure 2.12). [40] In the reference system, the ohmic potential drop increased due to the accumulation of an unstable SEI layer on the LMA surface *via* the undesirable interfacial reaction between Li metal and the electrolyte, and then the ohmic potential drop decreased due to a failure to maintain the expanded structure of the unstable SEI layer on the LMA surface. While this phenomenon occurred repeatedly during cycling, the continuous exposure of fresh Li to the electrolyte resulted in a thick inactive layer and electrically isolated Li, which can act as a resistive element on the LMA surface. Thus, the ohmic potential drop continuously fluctuated and the internal resistance markedly increased to the electrolyte degradation level. Furthermore, the repeated formation/collapse of the unstable SEI caused irregularities in the anodic polarization curves (Figure 2.13). Because this behavior of the reference system continued as the cycles progressed, the electrode properties of the Li metal as an anode were gradually degraded, eventually leading to cell failure. Unlike the reference system, the GAA applied system showed a much lower ohmic potential drop during the cycle progression over 1000 cycles (Figure 2.11b). Additionally, this was represented by a flat and regular anodic polarization curve for up to 1000 cycles without any convex profile corresponding to the energy barrier to Li^+ ion transfer by the thick inactive layer and the electrically isolated Li. These results were due to stable SEI formation.

This passivation effect of the LMA surface, which was based on formation of a stable SEI caused by the GAA separator, increased the reliability of the cycling characteristics of the LMA during charge/discharge under various test conditions: (1) at a current density of 5 mA cm^{-2} (1 mAh cm^{-2}), (2) in a rapid charge/discharge test at a high current density of 20 mA cm^{-2} (1 mAh cm^{-2}), and (3) at a high current density and high areal capacity (20 mA cm^{-2}, 20 mAh cm^{-2}) (Figure 2.11b–d). [22-25]

Galvanostatic cycling measurements of Li metal batteries using an LFP cathode were then performed to prove the effectiveness of the GAA separators in an actual Li/LFP cell. For a high C-rate test, the synthesized LFP was additionally post-processed with N-doped carbon (NC) and reduced graphene oxide (rGO), which were applied to Li/LFP cells. [44] Before the test, the Li/LFP cells underwent a rest stage and two stages of the stabilization process to initialize the LFP interface (Figure 2.11e). The Li/LFP cells were then tested at a 20 C-rate within a potential window of 2.5 V to 4.2 V. As shown in Figure 2.11f and g, the Li metal battery with the GAA separator retained 82.13% (100.45 → 82.50 mAh g^{-1}) of its initial capacity after 1000 cycles, and showed lower capacity fading as compared with the Li metal battery without the GAA separator (with the uncoated aramid separator), which retained 38.41% (100.67 → 38.67 mAh g^{-1}) of its initial capacity after 1000 cycles. Figure 2.14 indicates the coulombic efficiency for the two cases. In terms of capacity fading, the Li metal battery with the GAA separator was superior to the Li metal battery with the uncoated aramid separator because the interfacial stability between the LMA and electrolyte was improved by resolving the undesirable interfacial reaction that deteriorated the reliability of the LMA, as was the case of Li|Li symmetrical cells. Thus, the galvanostatic cycling measurements showed that the GAA separator could efficiently stabilize the LMA surface.

Additionally, a Li/GAA/LFP pouch cell was fabricated to exhibit its bending stability (Figure 2.15), with the GAA separator demonstrating good flexibility as a result of the structure of woven aramid fibers and the softness of the used binder (PR). In the Li/GAA/LFP pouch cell, the binder polymer of the flexible LFP cathode preparation was replaced by poly(vinylidenefluoride-co-hexafluoropropylene) (PVdF-HFP) instead of polyvinylidene fluoride (PVDF). [45,46] This Li/GAA/LFP pouch cell was fabricated to investigate the effect of LMA surface stabilization during dimensional changes. For this purpose, the cell was cycled in the bent state at every ten cycling intervals (at a 20 C-rate within a potential window of 2.5 V to 4.2 V), and showed good cyclic stability during repeated dimensional changes between the flat and bent states while maintaining low capacity fading.

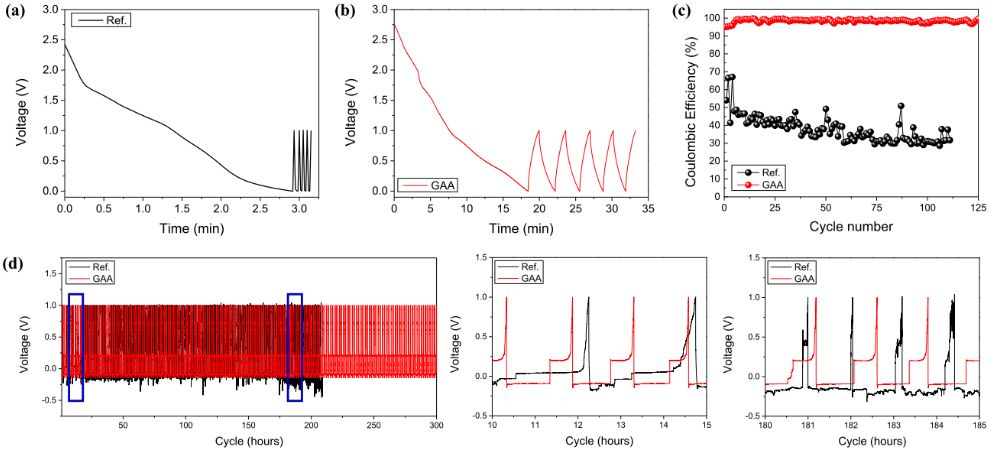

Figure 2.9 Galvanostatic cycling measurements of Li/Cu asymmetric cell (half-cell). Initialization process of (a) the reference system and (b) the GAA applied system. (c) Coulombic efficiency. (d) Time–voltage profiles.

Galvanostatic cycling measurements of a Li/Cu asymmetric cell (half-cell) structure were conducted to analyze the Li^+ ions plating/stripping behavior on the surface and assess the SEI structure stability when using GAA separator in a three-electrode system. [43] In Li/Cu asymmetric cell, a planar Cu foil served as the working electrode and Li foil served as both the counter electrode and the reference electrode. The structure of the reference system and the GAA applied system are as follows; the reference system - Li/aramid/Cu (black), the GAA applied system - Li/aramid/graphene-coated-fibers/Cu (red). To evaluate the stability of SEI formed in the GAA case, the graphene-coated-fibers side was put in contact with the planar Cu foil. Before the test, asymmetric cells (half-cell) were cycled 5 times from 0 to 1 V at a current density of 50 μA cm^{-2} for initialization. The purposes of initialization were to remove any contamination on the surface, and to stabilize the interface and the initial SEI. During this initialization process, the plated Li$^+$ ion was partially consumed for the formation of initial SEI layer. Then, Li$^+$ ion was plated on the Cu foil (the working electrode) at a current density of 1 mA cm^{-2} (1 mAh cm^{-2}). Next, the polarity was reversed, and the plated Li on the Cu foil was stripped to Li foil (the counter and reference electrode) up to 1 V. In the reference system, since SEI was unstable, a new SEI was continuously formed in each cycle, consuming the Li$^+$ ion source; this led a low coulombic efficiency and a minimal capacity stripped at each cycle because no Li reservoir was employed. Therefore, the reference system was gradually degraded as the cycling continued. When less than only 30 % of coulombic efficiency appears, the system is virtually a failure. However, the GAA applied system showed the low cathodic overpotential in constant and regular shape when the cycle progressed. This indicates the SEI is stable due to the passivation by the GAA separator. Therefore, the GAA applied system exhibited the coulombic efficiency of >99% after the initial stages because only a little Li$^+$ ion source was consumed to form new SEI. These results prove that the GAA architecture can improve the structural stability of SEI formed on it, and GAA separator can help induces the stable SEI.

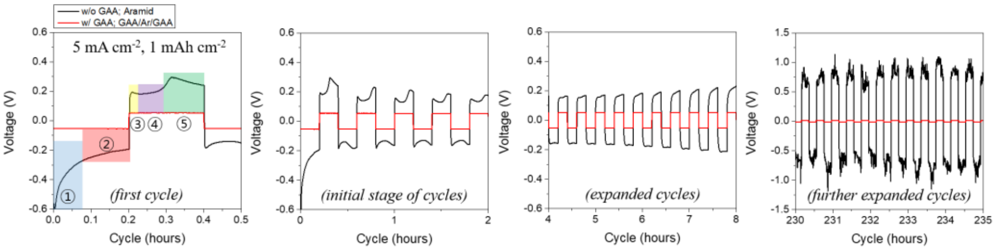

Figure 2.10 Stepwise behavior of Li|Li symmetrical cell.

The voltage variation in the time-voltage profile, when current was applied to Li metal anode in the reference system, indicates the stepwise behavior according to the kinetics of each stage. And such kinetics is relied on the morphological surface changes of Li metal anode. [40–42] The initial stages of the cycle represent the peaking shape which is dependent on the spatially varying rate constant. In the first half-cycle of region 1, in the manufacturing process, the native oxide layer and the initial SEI layer spontaneously formed in both the reducing electrode and the oxidizing electrode induce the specific kinetic hindrance. And such layers interfere the Li^+ ions plating to the reducing electrode and the Li^+ ion stripping from the oxidizing electrode, contributing to the high overpotential at the beginning stage. In region 2, as the Li^+ ion plating progressed, the nucleation points, which can grow into the dendritic growth containing SEI, were formed on the surface of the reducing electrode, while SEI also was formed on the Li metal anode surface. In this stage, the dendritic growth took precedence over the formation of the nucleation point in the reducing electrode, and the pitting process is dominant in the oxidizing electrode. Thus, the overpotential gradually decreased from the initial maximum overpotential at the beginning stage. After the polarity is reversed, the reducing electrode and the oxidizing electrode were reversed. In second half-cycle of region 3, since the fluctuated surface with pits and the dendritic growth of the nucleation point on the reducing electrode contributed to the activation barrier for Li^+ ion transfer, a convex graph shape appeared in the initial voltage. In this step, the nucleation point formation was dominant than the dendrite growth on the reducing electrode, and in the oxidizing electrode, the stripping from the dendrite was in preference to from bulk Li because of the short pathway. As the plating continued, the Li^+ ion movement pathway transitioned from the nucleation point formation to dendrite growth on the reducing electrode. After the pathway transition has occurred, the plating to the dendrite on the reducing electrode and the stripping from dendrite on the oxidizing electrode were dominant, and this kinetics was relatively fast. Besides, the Li which was newly deposited in the previous cycle did facilitate the stripping process on the oxidizing electrode. Thus, the minimum voltage was observed in region 4. All the Li deposited in the previous cycle were stripped and the active Li source was exhausted, and then, the Li source was changed from dendrite to bulk Li. Therefore, an energy barrier was required in the stripping process from bulk Li under the SEI layer, increasing overpotential in region 5. In this process, the Li dendrite, of which the active Li was depleted, became the electrically isolated Li as the resistance element. In the tail area of region 5, the pathway transition reoccurred from the bulk Li to the pits on the oxidizing electrode, reducing the overpotential. Like this, a minimum amount of the inactive layer, which was accumulated on the electrode, did induce the fast quasi-steady-state condition during the initial cycles; hence, the time-voltage profile was mainly determined by the spatially varying rate constant. This process was continuously repeated as the cycle progressed, accumulating more inactive layer from pits, dendrite, and isolated Li on the Li metal anode surface, which established a large concentration gradient. Therefore, as the cycle progresses, the effective diffusion coefficient became smaller. In the expanded cycles, since the thick inactive materials layer made tortuous pathway across the electrode/electrolyte interphase, the Li^+ ion transport was impeded by this thick inactive layer. And the large Li^+ ion concentration difference between the reducing electrode and the oxidizing electrode made that the mass transport be the dominant kinetics in the expanded cycles. This interfacial concentration variation was accompanied by an overpotential increase and the dynamic concentration gradient reached its quasi-steady-state equilibrium with the arc shape plateau of the time-voltage profile in the half cycle. When continuing the cycle, in the further expanded cycles, the brittle nature of the unstable SEI resulted in cracks on its surface and the exfoliated dendrites re-exposed the underneath Li to fresh electrolyte. The exposed pristine Li consumed the fresh electrolyte and generated the new SEI. These undesirable interfacial reactions induced the increase of the ohmic potential drop and the irregular anodic polarization curve, eventually causing the cell failure. Due to this characters of Li as an anode, at a current density above 0.5 mA cm^{-2}, suppressing the Li dendrite for a long-time is a hard task; besides, the when current is applied, controlling the unstable SEI formation by the dendrite nucleation and the pits is challengeable as well.

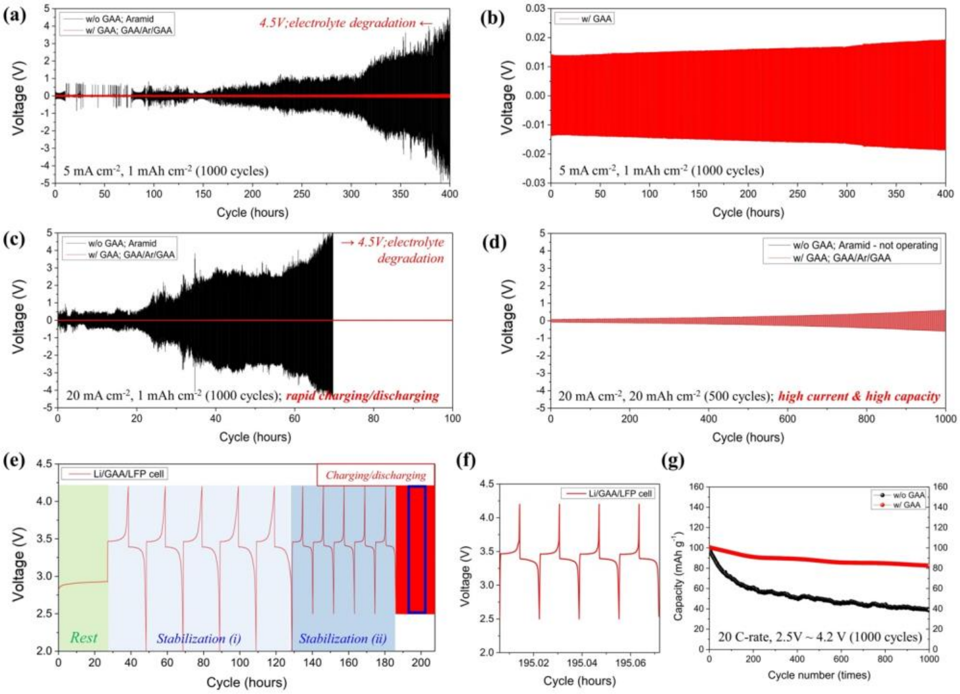

Figure 2.11 Galvanostatic cycling measurements. (a) Time–voltage profile for a Li|Li symmetrical cell of the reference system and the GAA applied system at a current density of 5 mA cm^{-2} (1 mAh cm^{-2}). (b) The ohmic potential drop of a Li|Li symmetrical cell with the GAA separator for 1000 cycles at a current density of 5 mA cm^{-2} (1 mAh cm^{-2}). Time–voltage profiles for a Li|Li symmetrical cell of the reference system and the GAA applied system (c) under rapid charge/discharge conditions (20 mA cm^{-2}, 1 mAh cm^{-2}), and (d) at a high areal capacity at high current density (20 mA cm^{-2}, 20 mAh cm^{-2}). (e) The entire time–voltage profile of Li metal batteries (Li/LFP) with the GAA separator. (f) Time–voltage profile of the mid-cycle-stage at a 20 C-rate (blue square of the (e) graph). (g) The cycling performance of Li metal

batteries (Li/LFP) with the GAA separator and the uncoated aramid separator (the reference system) at a 20 C-rate (The N/P ratio is 30)

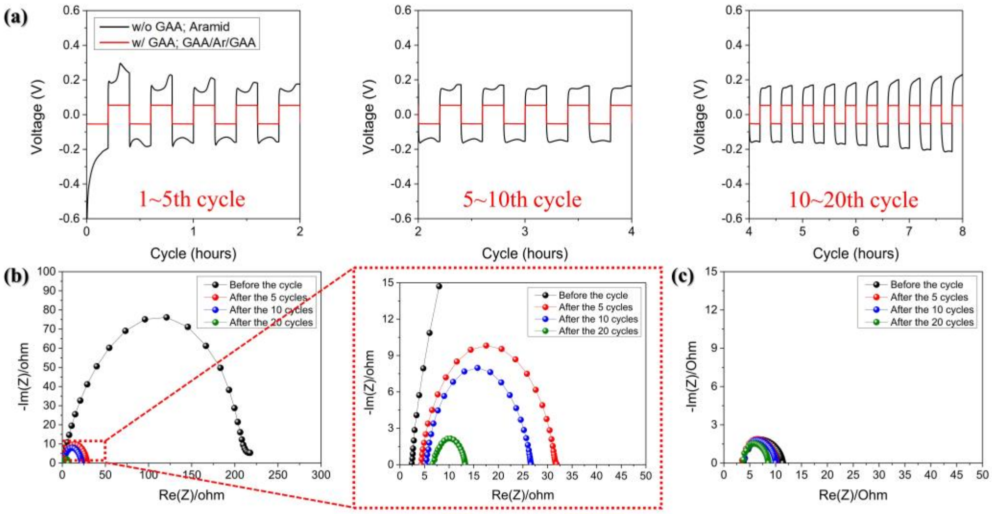

Figure 2.12 (a) Time–voltage profiles in initial stage (1 ~ 20th cycles). EIS data of (b) the reference system, (c) the GAA applied system.

The reference system indicates a high resistance (~220 Ω cm^{-2}) before the cycling. As cycle progresses, it was significantly decrease to 31.8 Ω cm^{-2} after the 5 cycles and to 26.6 Ω cm^{-2} after the 10 cycles and to 13.2 Ω cm^{-2} after the 20 cycles as a result of the native oxide layer destruction and the dendritic Li formation, while the GAA applied system showed a low resistance and a small decrease by the stable SEI formation at the initial stage; 11.4 Ω cm^{-2} before the cycling, 10.1 Ω cm^{-2} after the 5 cycles, 9.90 Ω cm^{-2} after the 10 cycles, 8.62 Ω cm^{-2} after the 20 cycles. [40]

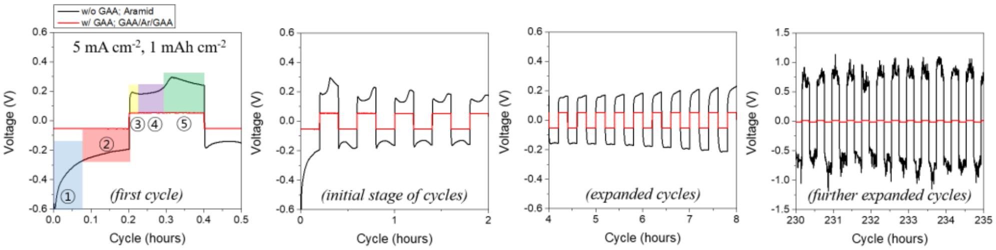

Figure 2.13 Anodic polarization curves in Li|Li symmetrical cell test as the cycle progresses (5 mA cm^{-2}, 1 mAh cm^{-2}).

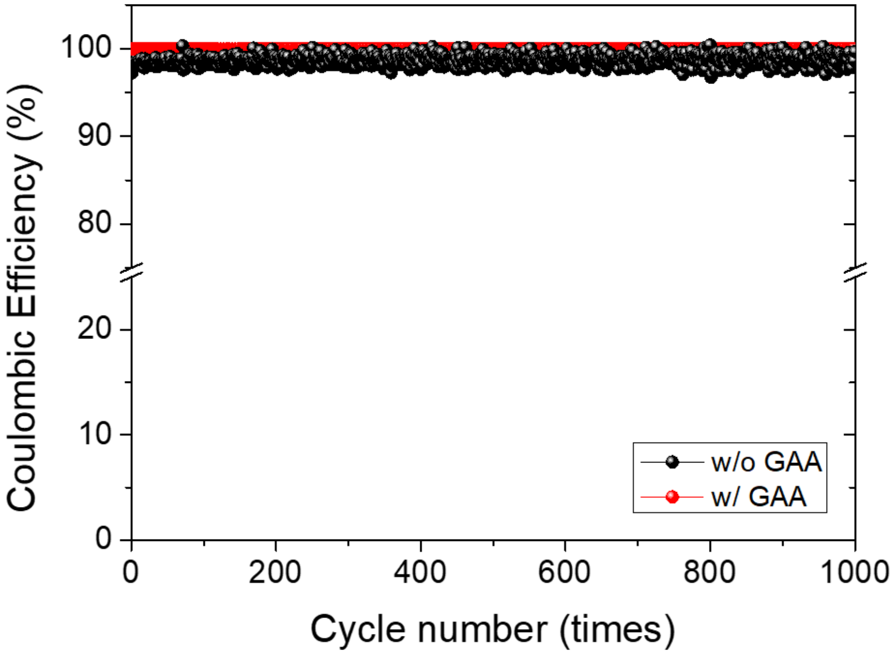

Figure 2.14 Coulombic efficiency of Li metal batteries with GAA separators (sample) and without GAA separators (ref.).

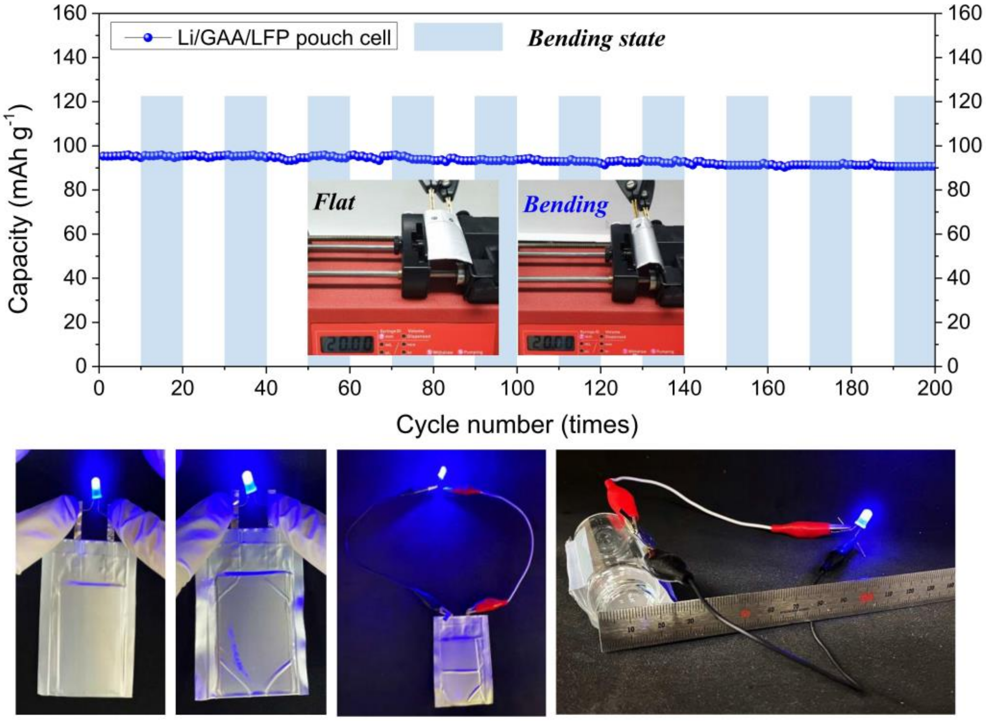

As-prepared *5 th bending* *10 th bending*

Figure 2.15 The cycling performance of the flexible Li metal battery with the GAA separators in the repeated dimensional change (20 C-rate, bending radius: 20 mm).

2.2.3 Optophysical characteristics

X-ray photoelectron spectroscopy (XPS), Fourier transform infrared spectroscopy (FT-IR, microscopic mode), and time-of-flight secondary ion mass spectrometry (TOF-SIMS) analyses were then performed to demonstrate that the LMA surface could be stabilized due to a relatively large amount of the stable SEI in the GAA applied system. All analyses were performed using the graphene-coated fiber side or the LMA surface tested after the course of 1000 cycles at a current density of 5 mA cm^{-2} (1 mAh cm^{-2}). In Figure 2.16a and b, the XPS data show the carbon peaks for the graphene-coated fiber side before and after the cycles, respectively. Before the cycles, on the graphene-coated fiber side, the binding state of the carbon was indicated by the strongest sp^2 C peak for graphene and weak C–OH and C–O peaks for the PR used as a binder (C 1s, 92.84%, and O 1s, 7.16%). [47,48] After the cycles, the sp^2 C peak decreased along with an increase in the C–OH and C–O peaks, while additional COOH, covalent C–F, and semi-ionic C–F bonds appeared. In terms of SEI formation, the increases in C–OH and C–O bonds and the appearance of COOH bonds represented the SEI component formed by the electrolyte decomposition. [49,50] Notably, the semi-ionic C–F bond was formed on the graphene-coated fiber side *via* fluorinated metathesis. As shown in our previous work, the semi-ionic C–F bond, which has intermediate properties of a covalent C–F bond and ionic C–F bond, could be formed along the surface of the CCN material in a specific solvent environment when a current was applied. [14] A polar, compact, and high dielectric constant solvent such as ethylene carbonate (EC) can further stabilize PF_5 in the decomposition process of PF_6 anions of the $LiPF_6$ electrolyte. [51] During this decomposition process, the further stabilized PF_5 also helped fluorine radicals to exist in an instantaneously intact state, and then they reacted with the sp^2 C of graphene. Therefore, semi ionic C–F bonds and covalent C–F bonds appeared. Especially, in the semi-ionic C–F bond, the fluorine atom connected to the CCN is in the hyperconjugation state, thereby resulting in a slightly delocalized electron of the carbon–fluorine bond. [52] It induces a lower-order fluorine atom on the partially fluorinated CCN with longer bonding length. Thus, the low-order fluorine atom of the semi-ionic C–F bond has chemically labile properties and the low bonding dissociation energy of fluorine, so it could induce LiF, known as a stable SEI component, when Li^+ ions were plated in a reducing atmosphere. [53] In the GAA applied system, formation of the semi-ionic C–F bond and a higher proportion of LiF relative to that of the reference system were identified by F XPS (Figure 2.17).

The semi-ionic C–F bond and LiF were also observed by FT-IR. In microscopic FT-IR sectional analysis of the reference system, the peaks designated as the carbon–

fluorine bond and LiF revealed no peak as compared with the peak variation before and after the cycles, whereas, in the GAA applied system, an aromatic C–F bond, a semi-ionic C–F bond, and LiF were observed on the fiber cross-section (Figure 2.18a and b). Thus, a stable SEI including LiF was formed along the graphene-coated fibers. This stable SEI, which contained a large amount of LiF formed *via* fluorinated metathesis (the F-doping mechanism) of the CCN material, affected the cycling characteristics of the cell. Meanwhile, the characteristic peak at 1200 cm^{-1} attributed to the mono-fluorinated aliphatic group, which was formed from the reaction of the fluorination or the oxyfluorination of the aramid group by F anions, was not observed in both the uncoated aramid separator and the graphene-coated aramid separator before and after the cycles (Figure 2.18c and d). [48] This result showed that the aramid does not react chemically with F anions within the cell environment when the electric field was applied. Additionally, the residual electrolyte was observed *via* XPS. Figures 2.16c–e show the residual electrolyte as the original state in P XPS. Phosphorus is the central atom of the electrolyte anion (PF_6); therefore, its binding state offers information about the electrolyte degradation. In the reference system, a considerable amount of electrolyte was consumed during new SEI formation through the side reaction of the repeated formation/collapse of the unstable SEI layer on the LMA surface. Moreover, accumulation of an inactive layer and electrically isolated

Li resulting from the side reaction induced the internal resistance of the cell, which markedly increased up to the electrolyte degradation level. These phenomena resulted in low residual electrolyte (7.92%). However, application of the GAA separator resulted in a high ratio of electrolyte remaining in its original state (64.87%), indicating that less electrolyte was consumed for the formation of a new SEI due to the stable SEI on the LMA surface. This result agreed with the attenuated increases in internal resistance in the Li|Li symmetrical cell using the GAA separator as shown in Figure 2.11b. Furthermore, the stable SEI formed at the LMA surface was in contact with the graphene-coated fiber side, and the LMA surface has a high ratio of LiF.

Figures 2.16f–h show the TOF-SIMS depth profile and elemental 3D depth mapping images of the LMA surface for molecules known as stable SEI components. Although the ratios of CO_3^-, Li_2O^-, and $Li_2CO_3^-$ (as stable SEI components) on the LMA surface did not differ greatly between the reference system and the GAA applied system, the ratio of LiF on the GAA-LMA surface showed a relatively higher intensity than that of the reference system by one order of magnitude. Additionally, due to the high ratio of stable SEI on the GAA-LMA surface, the proportion of unstable SEI components appeared relatively lower on the GAA-LMA surface than on the LMA surface in the reference system (Figure 2.19).

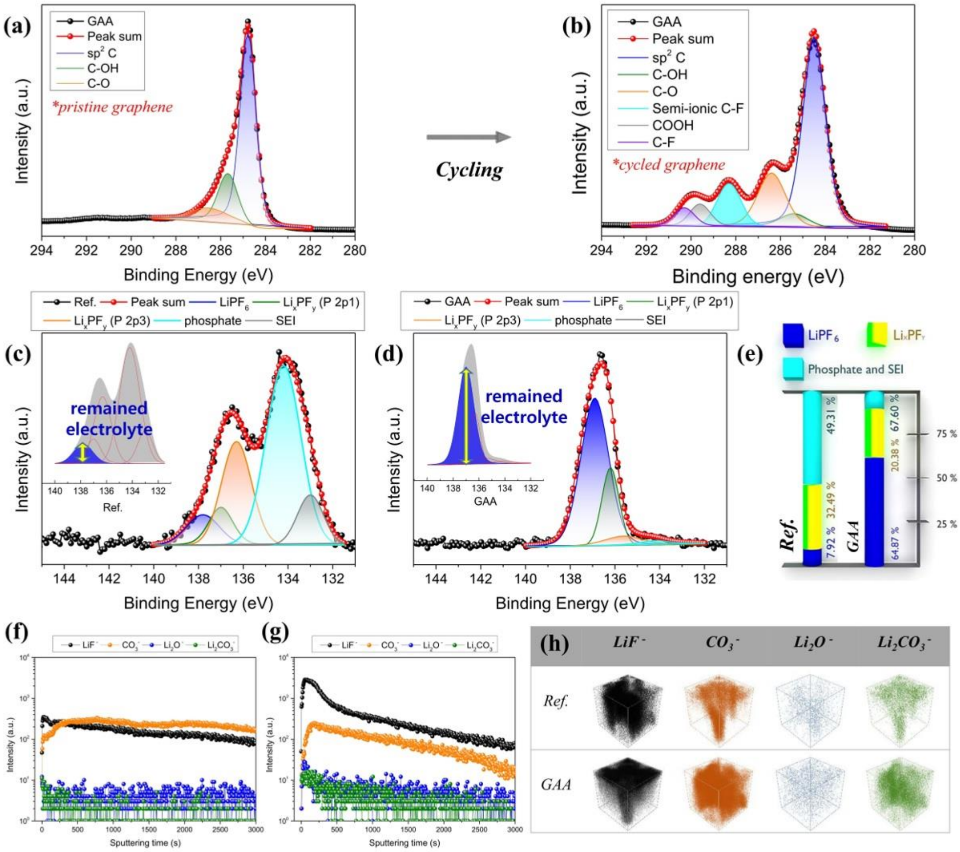

Figure 2.16 Optophysical analysis. (a and b) C XPS data of the graphene-coated fiber side of the GAA separator before the cycles and after the cycles. P XPS data after the 1000 cycles at a current density of 5 mA cm^{-2} (1 mAh cm^{-2}) for (c) the reference system and (d) the GAA applied system, and (e) the bar graph comparing the residual electrolyte in the two systems. TOF-SIMS data of the stable SEI component on the Li metal anode surface for (f) the reference system and (g) the GAA applied system. (h) 3D depth mapping image comparing the stable SEI component in the two systems.

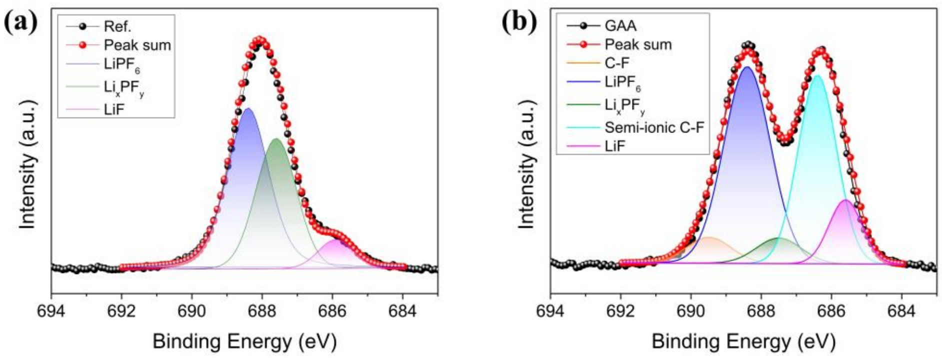

Figure 2.17 F XPS data. [49,56]

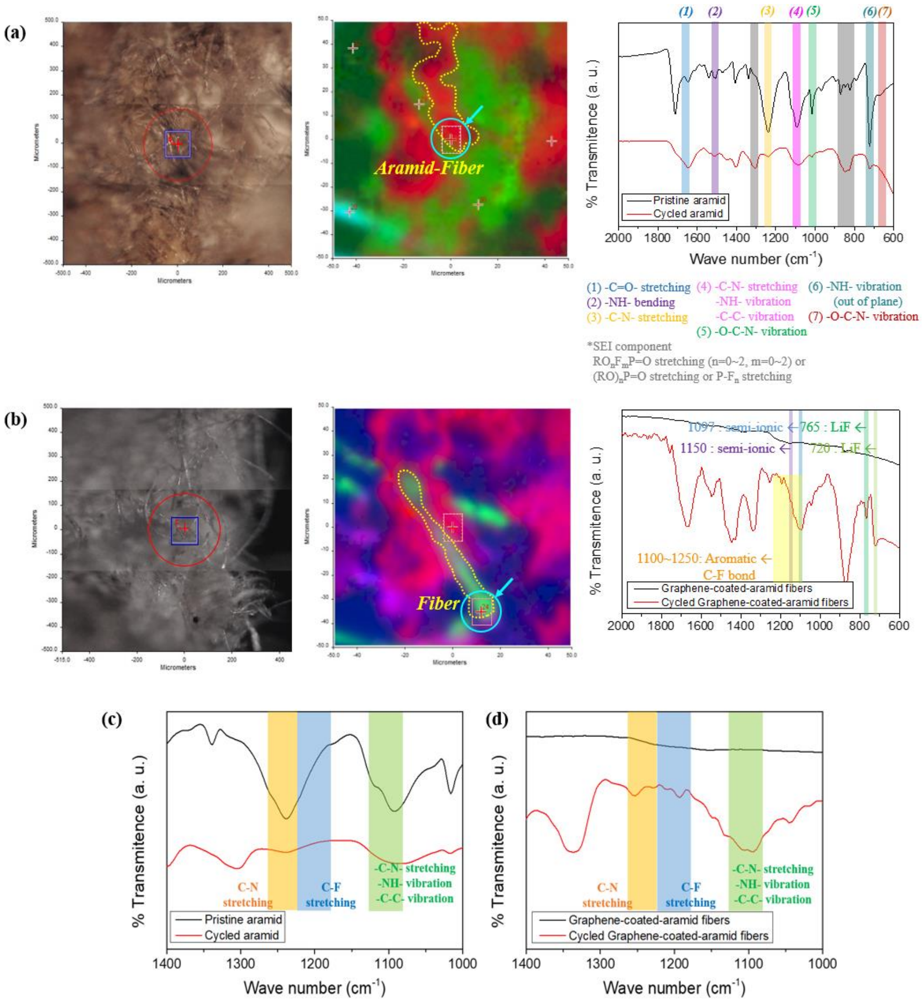

Figure 2.18 Microscopic FT-IR data of (a) the uncoated aramid fiber and (b) the graphene-coated aramid fiber after the 1000 cycles in the current density of 5 mA cm^{-2} (1 mAh cm^{-2}). (c and d) The enlarged graph from 1000 ~ 1400 cm^{-2}. To reveal sections, fibers was cut in an oblique direction using the surface and interfacial characterizing analysis system (SAICAS). The analyses were focused on the red cross in the white dotted square line. [36–39,57–60]

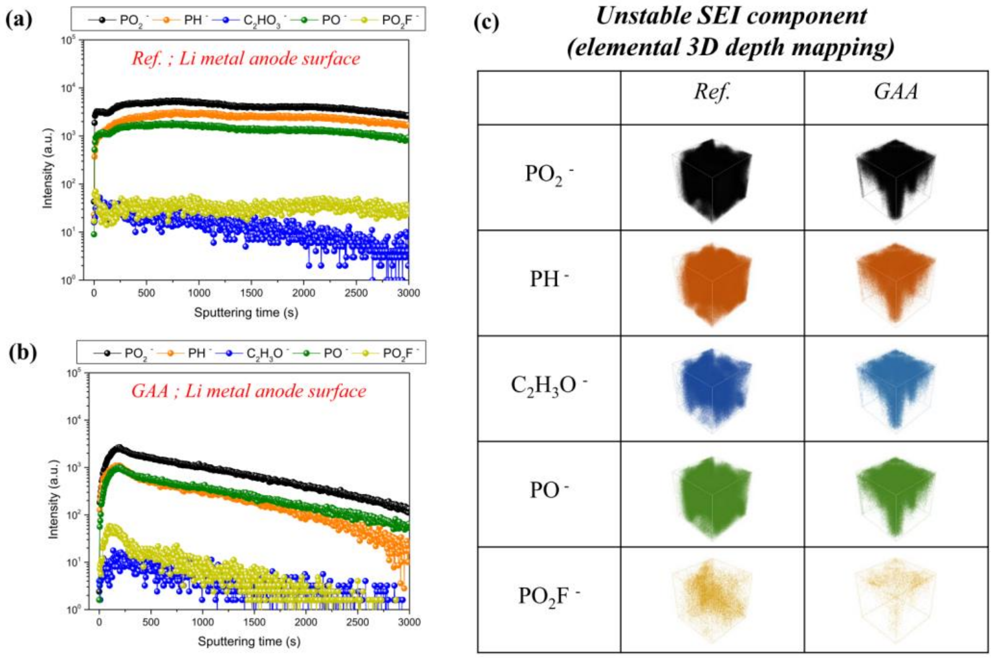

Figure 2.19 (a, b) TOF-SIMS depth profiles, (c) 3D depth mapping image.

2.2.4 Electron microscopy image analysis

The LMA surface of the GAA applied system and the graphene-coated fiber side of the GAA separator were visualized using scanning and transmission electron microscopy (SEM and TEM, respectively) to analyze the cell that was cycled 1000 times at a current density of 5 mA cm^{-2} (1 mAh cm^{-2}). Additionally, for comparison, the LMA surface of the reference system tested under the same conditions was analyzed. As shown in Figure 2.20, it was easy to distinguish the difference between the LMA surface of the reference system and the LMA surface of the GAA applied system even in the optical image. The difference in the LMA surface with and without the GAA separator was more pronounced in the SEM images. As can be seen in the facial section images of Figure 2.21a and b, the LMA surface of the reference system showed uncontrollable interfacial reactions between the Li metal and the electrolyte, which induced non-uniform plating/stripping, leading to accumulation of the thick inactive layer considered to comprise the unstable SEI, electrically isolated Li, and points where dendritic growth could progress. However, following application of the GAA separator, the LMA surface was a flat and smooth surface and absent a non-uniformly structured morphological interface (Figure 2.21c and d). Moreover, the cross sectional image showed that the LMA of the reference system displayed significant dimensional expansion and accumulation of the inactive layer due to the undesirable interfacial reactions, whereas, in the GAA applied system, such phenomena appeared significantly less often, and the morphology differed little from the initial state of Li (Figure 2.21e–g). As the cycles progressed, on the graphene-coated aramid fiber side of the GAA separator, both in the facial (Figure 2.22) and oblique (45°) (Figure 2.23) images, it was seen that the SEI grew along the coated fibers and was gradually filled from the bottom side to the upper side in the confined fiber structure. Because the SEI first formed on the graphene-coated aramid fiber side where electron migration was easy through contact with the LMA, this enabled the formation of a stable SEI containing large amounts of LiF on the LMA surface from an early cycle stage. Furthermore, the randomly woven architecture of aramid fibers with high modulus helped suppress the dendritic growth, which resulted in no observable dendritic shape. Similarly, as can be seen when a fiber was cut by a focused ion beam (FIB) (Figure 2.24), the SEI also grew along the graphene-coated fibers, and such a phenomenon was also observed in the energy dispersive X-ray spectroscopy (EDS) mapping image of the graphene-coated fiber (Figure 2.25). These findings suggested that the graphene-coated fibers provided a conductive framework for stable SEI formation. Figures 2.21h–o show the results of the TEM cross-sectional analysis for the graphene-coated fiber after the cycles. In Figure 2.21h, the aramid fiber cross-section and the graphene-coated layer with graphene flakes were identified. EDS mapping was carried out for the two identified areas. As shown in Figure 2.21i and j, EDS mapping of the identified areas showed that more C existed in the graphene-coated layer outside of the aramid fibers, with F observed mainly in this layer. Moreover, the SEI was formed along the graphene-coated layer, and minimal presence of P within the coating layer was observed, although some was found outside the coating layer (Figure 2.21k, Figure 2.24, and Figure 2.25). Therefore, fluorine seen in the EDS mapping image of the graphene-coated layer did not appear as an electrolyte component. Also, considering that the internal spacing of graphene was 0.28~0.31 nm (slightly less than the reference value of 0.33 nm), fluorine in the graphene-coated layer was caused by F^- anions, not electrolyte permeation (ionic diameters for PF_6: 0.51 nm, and F^-: 0.12–0.13 nm) (Figure 2.26). [55] To characterize fluorine in the graphene-coated layer, the surrounding chemical composition of the graphene with the clear lattice fringe was analyzed using EDS line data (Figure 2.21i and m). In the EDS line data, the intensity of elements other than fluorine was similar in the graphene with the clear lattice fringe and in the graphene with the lattice relaxation area, while the intensity of fluorine increased in the graphene with the lattice relaxation area. Given the above-mentioned optophysical analysis of the graphene-coated layer, the increase of the fluorine intensity in the graphene with the lattice relaxation area in the graphene-coated layer was estimated to be caused by the fluorine doping of the graphene lattice structure. Additionally, a change in F intensity was observed at the boundary between the graphene-coated layer and SEI layer (Figure 2.21n and o). The higher proportion of fluorine in the graphene-coated layer than in the SEI layer indicated that graphene and fluorine are chemically interacting in the graphene-coated layer, and this chemical binding could be due to the F-doping as shown in the optophysical analyses conducted on the graphene-coated fiber side earlier.

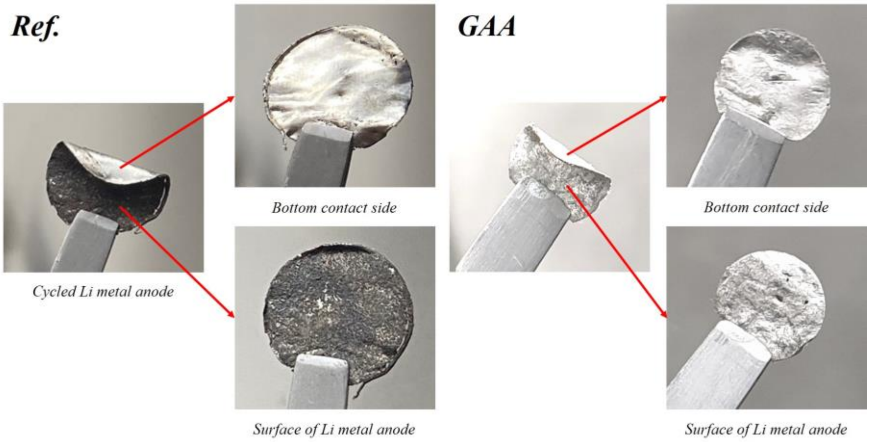

Figure 2.20 Optical image of Li metal anode before and after the cycle (1000 times at the current density of 5 mA cm^{-2} (1 mAh cm^{-2})).

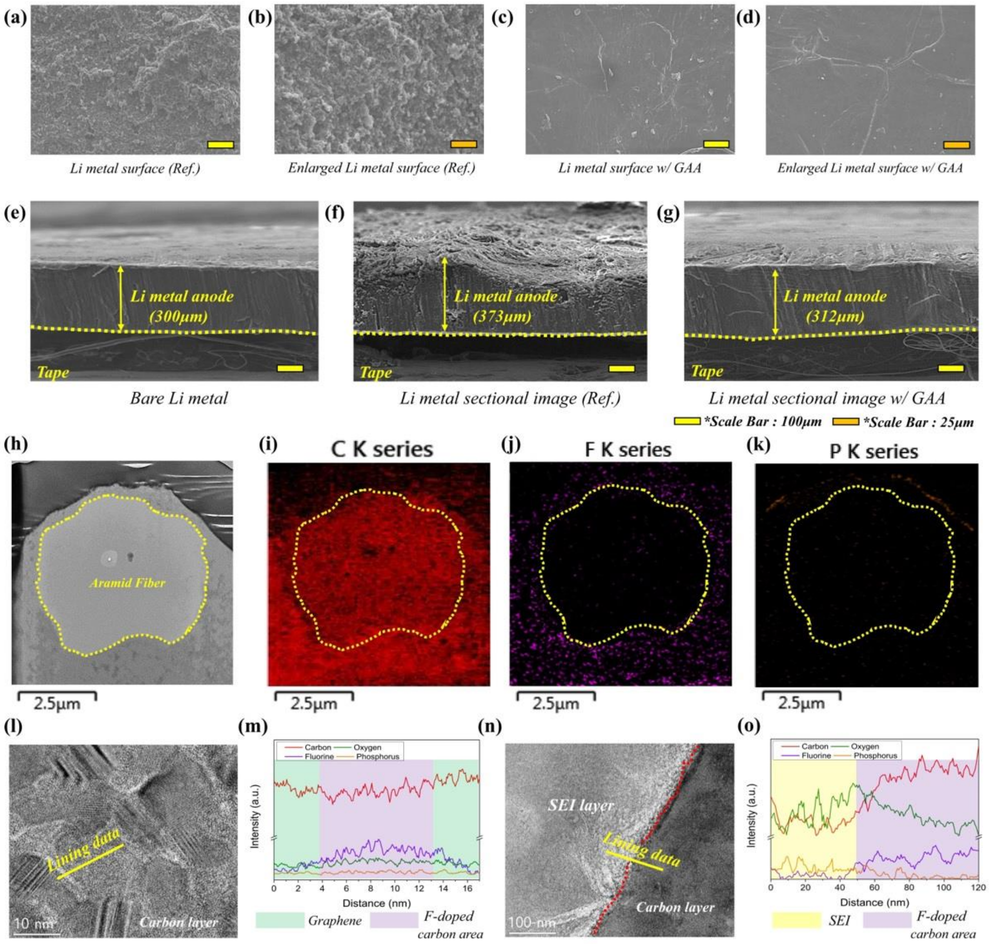

Figure 2.21 Electron microscopy image and energy dispersive X-ray spectroscopy data. The facial section images of the Li metal anode after the 1000 cycles at a current density of 5 mA cm^{-2} (1 mAh cm^{-2}) in (a and b) the reference system and (c and d) the GAA applied system. The cross section image of (e) the bare Li metal, (f and g) the reference system and in the GAA applied system after the 1000 cycles at a current density of 5 mA cm^{-2} (1 mAh cm^{-2}). (h) The cross section image of the single

graphene-coated-fiber after the cycles. The EDS mapping image of (i) C, (j) F, and (k) P in the sectional graphene-coated-fiber. (l) The enlarged image of the graphene-coating-layer, and (m) the EDS line data of the yellow line of the (l) image. (n) The enlarged image of the boundary between the graphene-coating-layer and the SEI layer on it, and (o) the EDS line data of the yellow line of the (n) image.

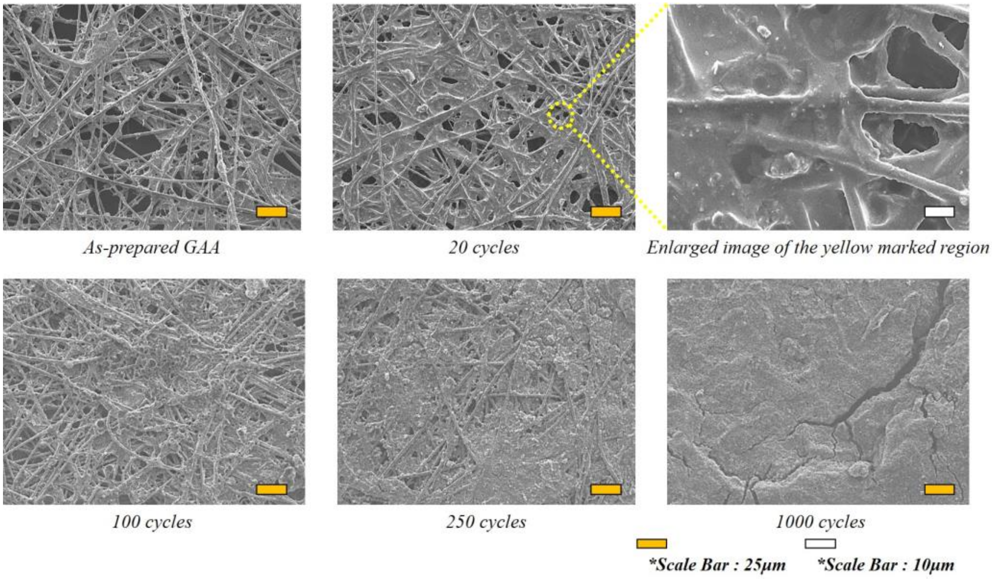
As-prepared GAA

20 cycles

Enlarged image of the yellow marked region

100 cycles

250 cycles

1000 cycles

Figure 2.22 SEM facial image of the graphene-coated-fiber side as cycle progresses.

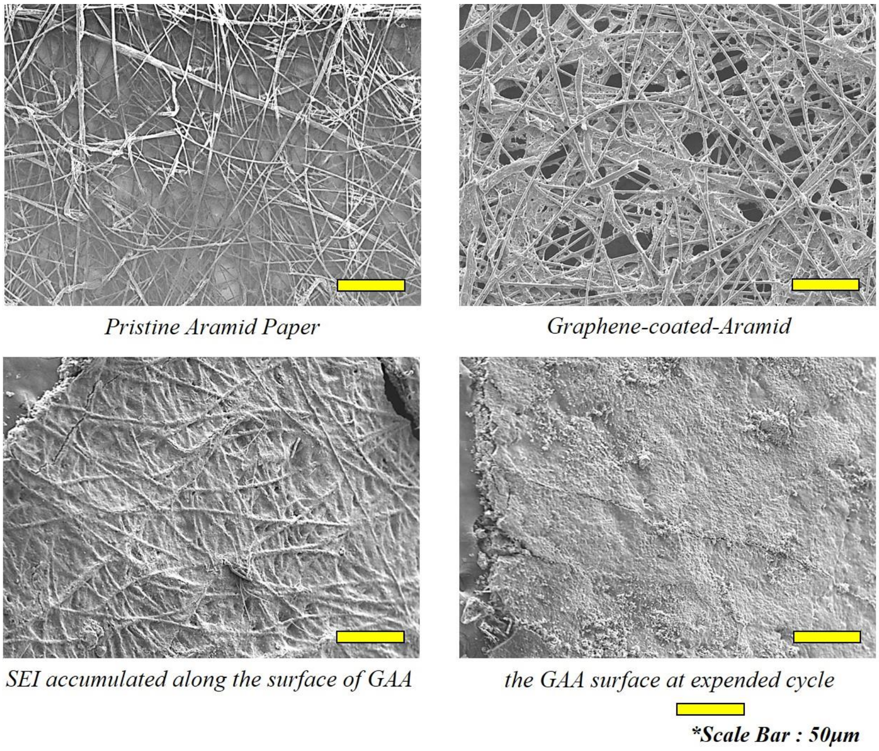

Pristine Aramid Paper

Graphene-coated-Aramid

SEI accumulated along the surface of GAA

the GAA surface at expended cycle

***Scale Bar : 50μm**

Figure 2.23 SEM oblique image of the graphene-coated-fiber side as cycle progresses.

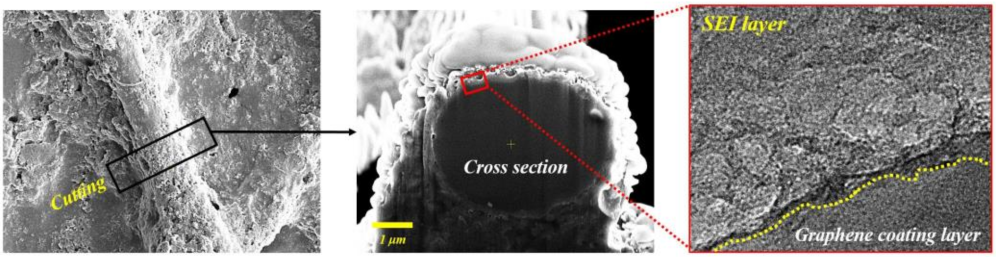

Figure 2.24 Cross-section SEM image of the fiber and the enlarged boundary image.

The mosaic area around the graphene-coating-layer was considered as SEI.

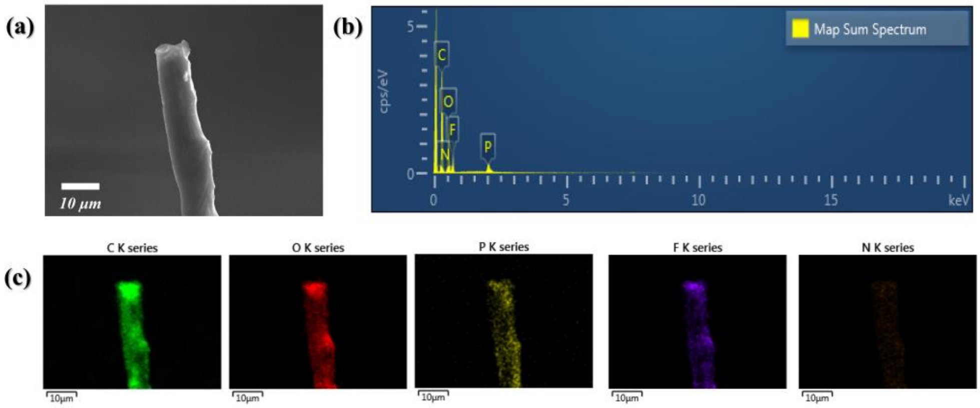

Figure 2.25 SEM analysis. (a) The single fiber strand image. (b) EDS data and (c) EDS mapping images of the single fiber strand of GAA after the cycle.

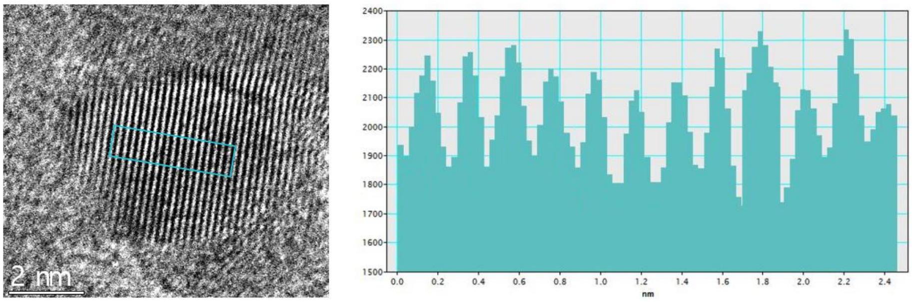

Figure 2.26 The internal spacing measurement of graphene using by Cs-STEM.

2.2.5 F-doping mechanism by fluorinated metathesis

Based on the optophysical characterization and electron microscopy analyses, Figure 2.27 illustrates the F-doping mechanism by fluorinated metathesis. As described in Figure 2.27a, the reference system was cycled with repeated formation/collapse of an unstable SEI on the LMA surface accompanied by the accumulation of an electrically inactive layer, Li dendrite nucleation and growth, dimensional expansion of Li metal, and fresh electrolyte decomposition. These side reactions degraded the cycling characteristics of LMA, with the reference system ultimately reaching cell failure. By contrast, Figure 2.27b shows LMA surface stabilization by the GAA separator. As a current was applied, a reducing atmosphere was created on the LMA surface and on the graphene-coated fiber side in contact with the LMA. Under this condition in the cell, the PF_6^- anion of the $LiPF_6$ electrolyte was decomposed to PF_5 and an F^- anion in the specific solvent environment of a polar, compact, and high dielectric constant solvent, such as EC. During the decomposition process, the specific solvent environment increased the stability of PF_5. It is because such a solvent does not form a large cavity between PF_5 and solvent molecules during the solvation process, and thus they have better access to PF_5, allowing PF_5 to be surrounded more closely by solvent molecules (another electrolyte solvent as a reference group is presented in

Figure 2.28). So, when the stability of PF_5 was increased by that solvent system in the PF_6^- decomposition process compared to the other adducts, it is estimated that the decomposition can be facilitated to form more PF_5 and F^- anions, and F^- anions can be formed more stably. At this time, the hybrid orbital of the fluorine coupled to the phosphorus was dissociated to a fluorine radical, and the fluorine radical exists in an instantaneously intact state under the influence of the stabilized PF_5. At this time, the graphene is in an electron-rich state, and then the fluorine radicals bind with the π orbitals of graphene to form a covalent C–F bond and a semi-ionic C–F bond (F-doped state). At the relatively high concentration used in LIB electrolytes, ~1 M, a large degree of ion pairs is believed to remain intact. As a result, the partially fluorinated graphene has a good conductive property and a low bond dissociation energy (BDE) of fluorine, and a tendency for Li^+ ions to be deposited on its surface. [53,61] Plating Li^+ ions resulted in the semi-ionic C–F bond of the F-doped surface, which has a chemically reactive property, inducing LiF on the graphene-coated layer and on the LMA surface in contact with that layer. This results in formation of LiF, as the key material of a stable SEI, in a relatively high proportion. This mechanism was also confirmed through separate ex-situ experiments (Figure 2.29). Therefore, in the GAA applied system, the SEI with relatively large amounts of LiF was stable, and the accumulated layer of unstable SEI during the cycles was much lower than that of the reference system, indicating the occurrence of fewer side reactions on the LMA surface. Furthermore, a large amount of electrolyte remained at levels similar to the original state, and stable behavior in the electrochemical tests was observed even at a high current density. Moreover, rather than unstably accumulating on the LMA surface, the SEI grew along the graphene-coated fibers in the randomly-arranged confined fiber system with high modulus, and minimal dimensional expansion and suppressed dendritic growth were observed. These results indicated that the LMA reliably maintained its cycling characteristics due to SEI stability induced by the GAA separator, thereby resolving the previously observed issues with the LMA related to repeated unstable SEI formation/collapse.

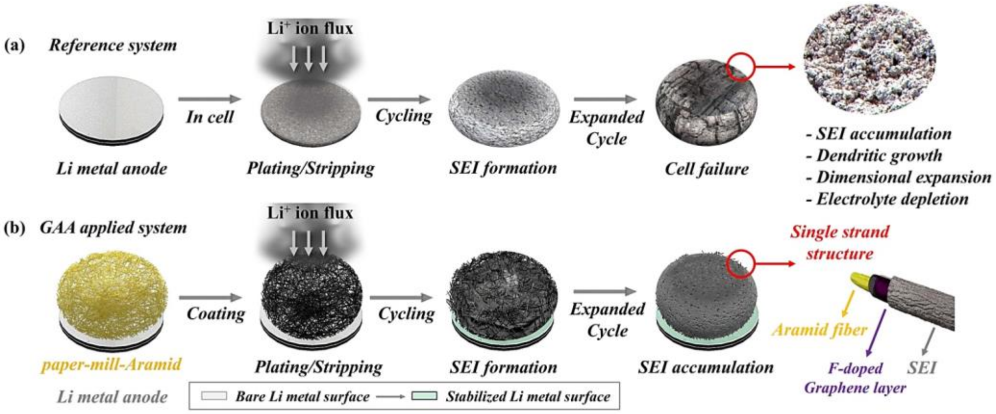

Figure 2.27 Concept images. (a) The behavior of the Li metal anode in the reference system. (b) The expected mechanism of the Li metal anode in the GAA applied system.

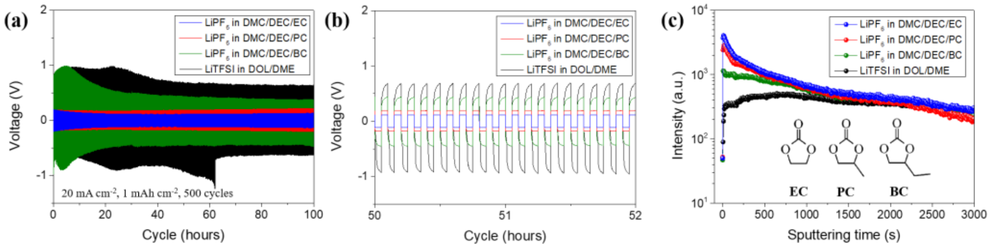

Figure 2.28 (a, b) Galvanostatic cycling measurement: the time–voltage profiles for Li|Li symmetrical cells in different solvent system. (c) The ratio of LiF^{-} among TOF-SIMS data for the LMA surface of in different solvent system.

To confirm the effects of solvent, the electrochemical data of the cells and the LiF ratio on the LMA surface is compared using ethylene carbonate (EC), propylene carbonate (PC), and 1,2-butylene carbonate (BC) (Polarity: EC > PC > BC, Size: EC < PC < BC, Dielectric constant: EC (90) > PC (65.5) > BC (56.1) at 300 K). [62,63] In addition, the different electrolyte system of LiTFSI in DOL/DME was also compared (DOL:1,3-dioxolane, DME: dimethyl ether). In a PC solvent introduced system, it showed a low ohmic potential drop and a stable anodic polarization curve, which means the stable operation of the cell. This is presumed that PC solvent has a similar role to EC solvent inside the cell environment. As a result, when PC was introduced, a relatively high proportion of LiF was formed on the surface of the Li metal anode, resulting in a stable SEI formation. However, when BC solvent was introduced, the time–voltage profile in the half cycle showed the arc shape plateau and the Li metal surface exhibited show a relatively low ratio of LiF. This is because the thick inactive layer as resistance factor made tortuous pathway across the electrode/electrolyte interphase to Li^+ ion migration, which means that the Li^+ ion transport was impeded by the thick inactive layer. So, the large concentration difference of Li^+ ion between the reducing electrode and the oxidizing electrode induces the change that the dominant kinetics became the mass transport in the expanded cycles. The interfacial concentration variation was accompanied by an overpotential increase, and then the dynamic concentration gradient reached its quasi-steady-state equilibrium with the arc shape plateau of the time voltage profile in the half cycle. [42–44] From these results, it is assumed that BC solvent, which has a lower polarity, a larger size, and a lower dielectric constant than EC or PC, was not effective in stabilize PF_5 and less affected the F-doping mechanism. That is, in a BC solvent introduced system, the surface stability of Li metal is significantly low in comparison to EC or PC solvent introduced system. [40–42] Meanwhile, the electrolyte system of LiTFSI in DOL/DME shows an arc shape plateau similar to that of BC, and indicates a low LiF ratio on the surface of Li metal anode. This suggests that the mechanism of LiF formation *via* fluorine doping to graphene proposed in this dissertation is difficult to be applied to the TFSI anion in DOL/DME system.

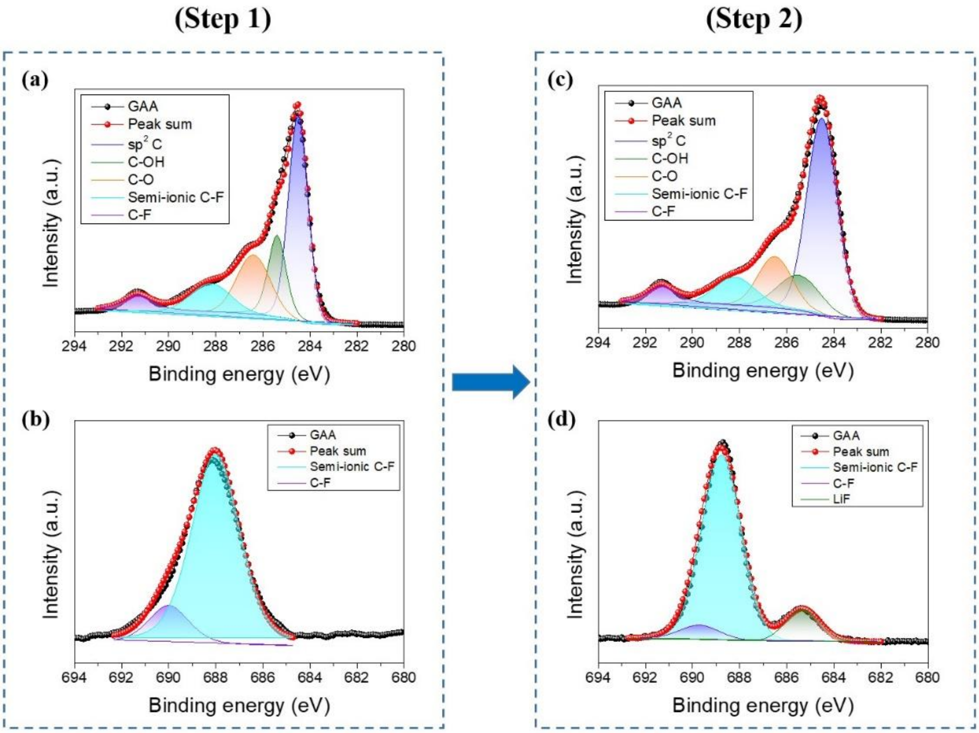

Figure 2.29 XPS data. (a) C XPS and (b) F XPS after F-doing process using HPF_6 in water. (c) C XPS and (d) F XPS after the Li salts treatment.

An ex-situ experiment was conducted in an external water jacket by separation into two steps involving the partially fluorinated graphene and the LiF formation. It confirmed that LiF is formed by Li^+ ion flux after fluorine was doped; (i) The graphene coating layer was partially fluorinated using 1 M HPF_6 in water when the electrical field was applied. At this time, the graphene coating layer was used as the role of the anode for receiving electrons in the coin-cell and a platinum electrode was used as the counter electrode, and a current density of 5 mA was applied continuously for 8 hours.

The platinum electrode should be used as the counter electrode because HPF_6 is a strong acid (pKa = −20 in water). In this process, water acts like an EC because it is also a polar, compact, and high dielectric constant solvent. (ii) After eight hours of the doping process, a sufficient amount of Li salt was melted in another water jacket filled with water. In this water jacket, the electrical field was applied to the F-doped graphene-coated aramid and the platinum electrode. The Li^+ ion flux migrates to the graphene coating layer while the anion of the Li salt migrates to the platinum electrode. During the experiment, the voltage was fixed at a value lower than the electrochemical window of the anion of Li salt to prevent the anionic decomposition of Li salt. As shown in XPS data, when the graphene coating layer goes through only step 1, the carbon-fluorine bonds appear in C XPS, but LiF does not appear in F XPS. The C–OH and C–O peaks is estimated to be due to the PR resin and the electrolysis of water. And, after the step 2, the carbon-fluorine bonds of C XPS and LiF peak in F XPS appear. Although the experiment was conducted in two steps, the result is the same as that of the manuscript. Through this result, it is possible to better understand the LiF formation by F-doping mechanism.

2.2.6 Semi-ionic C–F bond

The C–F bond characters of the fluorinated conjugated carbon network (CCN) materials are depending on the fluorine/carbon ratio (or stage number, C_x/F). [49,64,65] A decreased fluorine (the increased stage number) makes the C–F bond to have the properties of the ionic bond. Adversely, an increased fluorine (the decreased stage number) makes the covalent C–F bond. [49] The environment for the formation of commonly known semi-ionic C−F bonds is the fluorination of graphene. During the fluorination process of graphene, fluorine has two competitive reactions: (i) F^{-} anion reacts with the carbon atom of graphene to form a covalent C−F bond, where sp^3 carbon atom binds with F^{-} anion, thereby forming the buckled carbon sheet by fluorine. (ii) F^{-} anion reacts with the carbon atom of graphene to form a semi-ionic C−F bond, where sp^2 carbon atom binds with F^{-} anion, maintaining the planar carbon sheet without structure variation. The semi-ionic C−F bond is mainly formed by the chemical reaction of (ii) and shows its electronic configuration changes from sp^2 to sp^3, arising bond angle distortions. Therefore, the semi-ionic C–F bond has the intermediate state between the covalent bond and the ionic bond; it represents a lower bonding order and a longer bonding length than the covalent C–F, and it also has a chemically reactive property than the covalent bond without the ionization. [66] This nature of the semi-ionic C–F bond results from the binding state of fluorine atom, which is connected to the CCN as a hyperconjugation state, and results from the low the bonding dissociation energy (BDE) of fluorine atom to graphene. [35,54,67] This feature differs from the poly(tetrafluoroethylene) (PTFE) or poly(vinylidene-fluoride) (PVDF) derivatives containing of poly(carbon mono- or di- fluoride; low stage number), which are considered as inert due to their high bonding dissociation energy. [68] Moreover, the fluorine/carbon ratio (stage number) affects the conductivity. As the stage number (C_x/F) increases from 2 to 5 or more, the resistance decreases exponentially from 10^7 Ω cm to 10^{-3} Ω cm, showing a sufficient conductivity, unlike PTFE or PVDF which are considered as insulators.

In the proposed system, the semi-ionic C–F bond was formed also along the CCN materials in the coated fibers. When a current was applied, the reduction atmosphere was created in the electrode and the coated fibers in contact with the electrode. Then, in the decomposition process of an electrolyte, PF_6^- anion of $LiPF_6$ electrolyte was decomposed into PF_5 and F^- anion. Especially, when PF_6^- was decomposed in a solvent having polar, compact, and high dielectric constants properties, such as ethylene carbonate (EC) in this system, the resulting PF_5 was further stabilized and optimized by those solvent molecules in solvation process. In detail, because of the increase of PF_5 stability, the hybrid orbital of the fluorine coupled to the phosphorous of PF_6^- simultaneously could be dissociated during the decomposition process, and fluorine radical exists in an instantaneously intact state. At this time, the graphene is electron-rich state and then bind with sp^2-hybridized carbon in the CCN. Since only some of C atoms changed their electronic configuration from sp^2 to sp^3, the semi-ionic C–F bond was formed; fluorinated metathesis. Based on the atomic percent in EDS lining data, acquired at the site between the graphene with a clear lattice fringe and the lattice relaxation area (where carbon and oxygen interact chemically), the stage number was higher than 5. This indicates a low resistance and a low BDE of the partially fluorinated CCN. Therefore, the properties of the semi-ionic C–F bond, where the fluorine is partially connected to the CCN, were as follows: chemical reactivity from the low-order carbon-fluorine, conductivity from the high stage number, $C^{\delta+}$–$F^{\delta-}$ charge polarization from the high electronegativity of fluorine atom, and the low bonding dissociation energy of fluorine atom to graphene. This can lead to the unique fluorine-doped surface from the interaction between fluorine and carbon. Therefore, Li^+ ions can plate on the partially fluorinated sites of the CCN with the conductive property in the coated fiber, the semi-ionic C–F bond met Li^+ ion flux to generate LiF, as the key material of stable SEI. [61]

2.2.7 Application to other conjugated carbon network materials

Based on the preceding results of the electrochemical test and optophysical and electron microscopy analyses of the GAA applied system, other CCN materials were also tested using the PR coating platform to evaluate their capability of stabilizing the LMA surface *via* fluorinated metathesis (the F-doping effect). Other CCN materials include activated carbon (AC), among the most widely used carbon materials, and carbon black (CB), which is also widely used but closer to pure carbon than AC as a result of additional artificial treatment. To determine whether AC and CB promote LMA surface stabilization *via* the F-doping mechanism, the experimental and analytic results with AC and CB were compared with those from graphene, and the electrochemical data were averaged over ten cells to allow generalization. In Figures 2.30a–d, the galvanostatic cycling measurements of Li|Li symmetrical cells showed that both the AC- and the CB-coated fibers stabilized the LMA surface at a current density of 5 mA cm^{-2} (1 mAh cm^{-2}) during the course of 1000 cycles, whereas the internal resistance of the reference system increased above the electrolyte degradation level. However, there was a difference in their ohmic potential drop, which was caused mainly by accumulation of the inactive layer and electrically isolated Li. In the case of graphene, the ohmic potential drop did not differ significantly during the 1000 cycles, and the deviation was also low. However, AC and CB, especially AC, showed a tendency of a relative increase in the ohmic potential drop compared to graphene as the cycles progressed, and the deviation was also greater than that of graphene. These differences in the stability of the LMA surface with graphene-, CB-, and AC-applied symmetrical cell tests were also observed in the capacity fading of Li metal batteries using an LFP cathode (Figure 2.30e) and in the remaining electrolyte as the original state shown in P XPS after 1000 cycles of the Li|Li symmetrical cell test (Figure 2.30f–i). Application of the CB-coated fibers resulted in low capacity fading in the Li/LFP cell after 1000 cycles and close to that observed when the graphene-coated fibers were applied (CB – 101.66 → 70.98 mAh g^{-1}; average of ten cells at a 20 C-rate), with residual electrolyte levels after 1000 cycles also close to those in cells applying the graphene-coated fibers (CB – 48.17%; average of ten cells at 5 mA cm^{-2}, 1 mAh cm^{-2}). Meanwhile, application of the AC-coated fibers resulted in higher capacity fading after 1000 cycles relative to that observed for the CB-coated fibers (AC – 103.80 → 59.77 mAh g^{-1}; average of ten cells at a 20 C-rate) and close to the reference system during the first 250 cycles. Additionally, there was a relatively low quantity of residual electrolyte after 1000 cycles (AC – 21.31%; average of ten cells at 5 mA cm^{-2}, 1 mAh cm^{-2}). Figure 2.31 indicates the coulombic efficiency of Li metal batteries for each case. To determine the cause of the differences in LMA surface stabilization (graphene coating > CB coating > AC coating), C XPS analyses were conducted on each carbon material before and after cycling (Figure 2.32a–f). Only carbon and oxygen were detected by XPS (AC: N<0.1 at%). The particle size was similar among all the carbon materials after the grinding process (Figure 2.33). C XPS analysis before cycling revealed that the C–O-binding ratio increased in the order graphene coating (C: 92.84 at%; O: 7.16 at%) < CB coating (C: 92.21 at%; O: 7.79 at%) < AC coating (C: 91.40 at%; O: 8.60 at%), although the same amount of each carbon material and PR ratio were used. Conversely, C XPS analysis after cycling showed that the C–F-binding ratio decreased in the order graphene coating > CB coating > AC coating. In the proposed F-doping mechanism, the core reaction of the stable SEI formation was a "LiF induced reaction from a semi-ionic C–F bond". The semi-ionic C–F bond was derived from the partially fluorinated CCN material, which was formed by the reaction between the *sp*^{2} C atom of the CCN and F^- anion formed during the decomposition process of the PF_6^- anion in a specific solvent environment. Therefore, it can be inferred that the oxygen functionalities held by the intrinsic CCN materials affected this reaction. The oxygen functionalities induce a partial negative charge on the CCN ($C^{\delta+}$–$O^{\delta-}$) because oxygen is more electronegative than carbon. At this point, a higher number of negative functional groups in the CCN would increase the difficulty of C–F formation from the F^- anion and the *sp*^{2} C atom due to the negative repulsive force of the oxygen functionalities during semi-ionic C–F bond formation. Zeta-potential data for the negative charge induced by the carbon–oxygen functional groups of the intrinsic materials showed that graphene is electrically close to neutral (approximately -1.19 mV), whereas CB (approximately -25.50 mV) and AC (approximately -42.94 mV) were negatively charged due to the oxygen functionalities (Figure 2.32g).

Similarly, X-ray diffraction (XRD) data showed different peak positions due to the oxygen functionalities of intrinsic CB and AC compared to graphene (Figure 2.32h). In the case of graphene, the characteristic peak assigned to the (002) plane was observed as an intense and sharp crystalline peak of $2\theta = 26.5°$, indicating well-stacked CCN sheets in a d-spacing of 0.33 nm, similar to the theoretical value. For CB and AC, this crystalline peak assigned to the (002) plane was broader, weaker, and shifted to a lower angle at $2\theta = 24.9°$ and at $2\theta = 22.8°$, respectively, indicating that the oxygen functionalities influenced and broadened both the crystalline structure and orientation of the aromatic layer slice. [69] Additionally, peaks of a lower angle of $2\theta \leq 10°$ were observed in CB ($2\theta = 7.02°$) and AC ($2\theta = 6.94°$), indicating the contribution of oxidation to the presence of the oxygen functionalities populated on the CCN sheets. [70–72] These results indicated that CB displayed a stronger and more intense crystalline property than AC and revealed a weaker oxidation peak than

AC, suggesting the good structural completeness of CCN sheets of the CB sheets and the low ratio of oxygen functionalities relative to AC. These findings identified increased oxygen functionalities on AC networks relative to CB as well as a greater presence of an amorphousized lattice structure relative to CB as a result of oxidation.

Considering the analyses of XPS, zeta-potential, and XRD, the CCN materials could stabilize the LMA surface *via* fluorinated metathesis (the proposed F-doping mechanism) in a specific solvent environment. However, the extent of the core reaction between F^- anions and the sp^2 C in the F-doping mechanism was varied according to the type of carbon material. Specifically, a large number of oxygen functionalities with negative charge in the CCN induced a repulsive force with F^- anions and resulted in amorphousized crystalline structures. Consequently, the core reaction could be hindered by the negative repulsive force and the disordered lattice structure. This inference becomes apparent when comparing the ratio of LiF on the LMA surface in each cell between application of graphene-, CB-, and AC-coated fibers, as well as the results of Li|Li symmetrical cell tests at a high current density. Figure 2.32i shows the ratio of LiF^- according to TOF-SIMS data for the LMA surface of each cell involving graphene-, CB-, and AC-coated fibers, revealing decreases in the LiF^- ratio on the LMA surface in the order of graphene, CB, and AC applications. This was especially evident for AC, which showed an LiF^- ratio similar to that of the reference system. As noted, the oxygen functionalities, which increased in the order of graphene, CB, and AC, interfered with F^{-} anion binding with the sp^2 C, thereby limiting the sites where the reaction to form LiF could occur in the same order. This suggests that an increased negative charge in CCN materials would result in decreased bond formation *via* F-doping and lower SEI stability. Furthermore, the difference in the ratio of stable SEI influenced the cycling characteristics of LMA. In general, a higher current density applied for LMA charge/discharge results in a higher number of nucleation points, which can promote unstable SEI formation and dendritic growth on the LMA surface, thereby limiting LMA operation to within a limited cycle range. [1-4,23] Although the ohmic potential drop in the AC-applied case was relatively higher than that in the graphene- and CB-applied cases, the AC-applied case did stably operate at a current density of 5 mA cm^{-2} (1 mAh cm^{-2}). However, the AC-applied case showed a significantly low stability with an increased internal resistance close to the electrolyte degradation voltage at a high current density of 20 mA cm^{-2} (1 mAh cm^{-2}) (Figure 2.34). This can be explained as follows: when AC-coated fibers are in contact with the LMA surface, there are not enough LiF formation sites for the F-doping mechanism to cover the nucleation points, thereby resulting in unstable SEI formation or dendritic growth at a high current density.

Due to the decreased LiF formation as a result of the presence of oxygen functionalities in intrinsic CCN materials, the resulting unstable SEI affects the life span of LMA. Thus, the life characteristic of the AC-applied system with a low ratio of stable SEI was much inferior to CB and graphene applications. Figure 2.35 indicates the results of the life-span test. When a cell using a predetermined amount of a Li source is cycled, depletion of the Li source causes its potential to increase. [73] This measurement was an application of a Li/Cu half-cell test, in which the voltage increases when all of the plated Li source on Cu (the current collector) was stripped. Considering that, the Li|Li symmetrical cell test was performed using a thin Li electrode with a capacity of 12.4 mAh cm^{-2} (Li – 30 μm thickness and 16 mm diameter) and at a current density of 6.2 mA cm^{-2} (6.2 mAh cm^{-2}; half-value). In this system, when the Li source equivalent to the half capacity (Li 15 μm thickness, 6.2 mAh cm^{-2} capacity) was exhausted to generate the SEI, the cell potential on the stripping side increased, and peaks appeared at the end point of each cycle stage in the time–voltage profile, because all of the remaining Li source was stripped from Cu. That indicated that the time at which half of the predetermined capacity was reduced was measured (cut-off voltage; 1.5 V). In the reference system, a Li source equivalent to the half capacity was exhausted within 28.16 h, as both the Li source and electrolyte were consumed to generate a new SEI each cycle. However, a higher ratio of stable SEI formation resulted in less Li source and electrolyte consumption; therefore, the Li source lasted longer, corresponding to a capacity of 6.2 mAh cm^{-2}, and indicating an improved lifetime; AC – 64.93 h, CB – 216.84 h, and graphene – 306.98 h.

Given the application of the F-doping mechanism to CCN materials, carbon materials close to the complete lattice structure of pure carbon are the optimized system for stabilizing the LMA surface by the F-doping mechanism in a specific solvent environment. Moreover, when the carbon material harbors more negative functional groups and a disordered lattice structure, the LMA stability is not mainly affected by the F-doping mechanism but rather by the property of the conductive framework. This agrees with previous studies reporting that the LMA surface is stabilized by the conductive interlayer. Although the degree of LiF formation by the F-doping mechanism was low, similar to the reference system, it still acted as a conductive framework. [12–15]

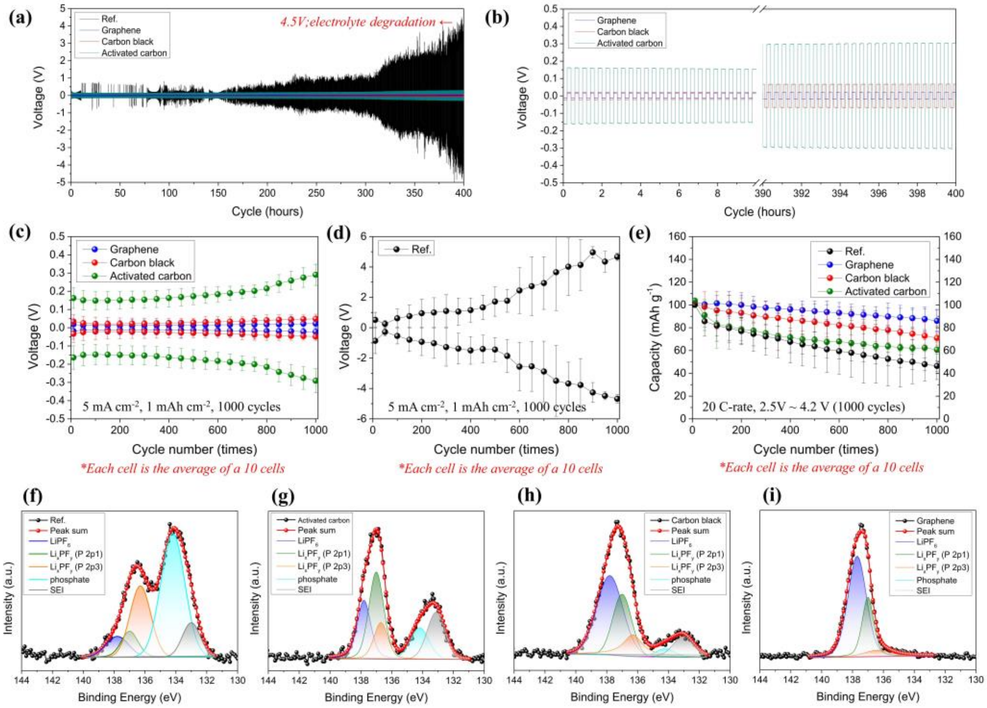

Figure 2.30 Galvanostatic cycling measurements and P XPS data of the reference system and the activated carbon-, carbon black-, and graphene-coated fiber applied systems. (a and b) Time–voltage profiles for the Li|Li symmetrical cell at a current density of 5 mA cm^{-2} (1 mAh cm^{-2}). (c and d) The ohmic potential drop tendency of Li|Li symmetrical cells at a current density of 5 mA cm^{-2} (1 mAh cm^{-2}). (e) The cycling performance of Li metal batteries (Li/LFP) at a 20 C-rate. (f–i) P XPS data after the 1000 cycles at a current density of 5 mA cm^{-2} (1 mAh cm^{-2}).

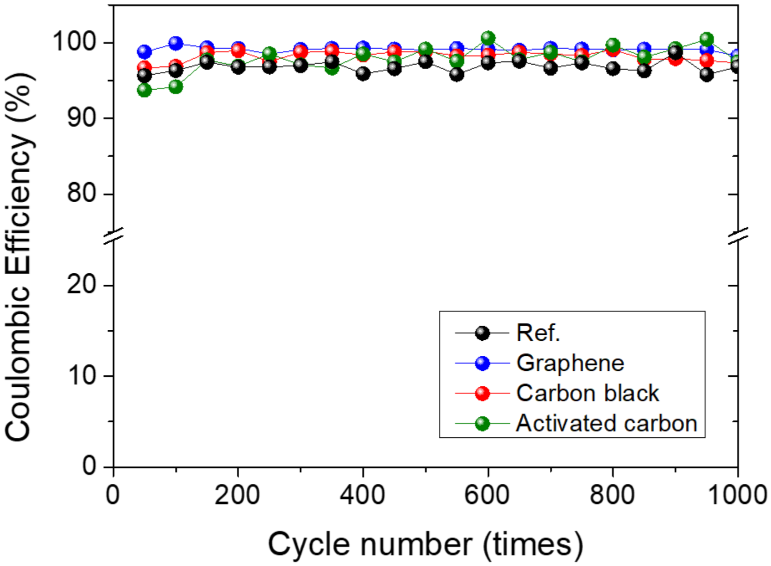

Figure 2.31 Coulombic efficiency of Li metal batteries in the case of the other CCN materials being applied.

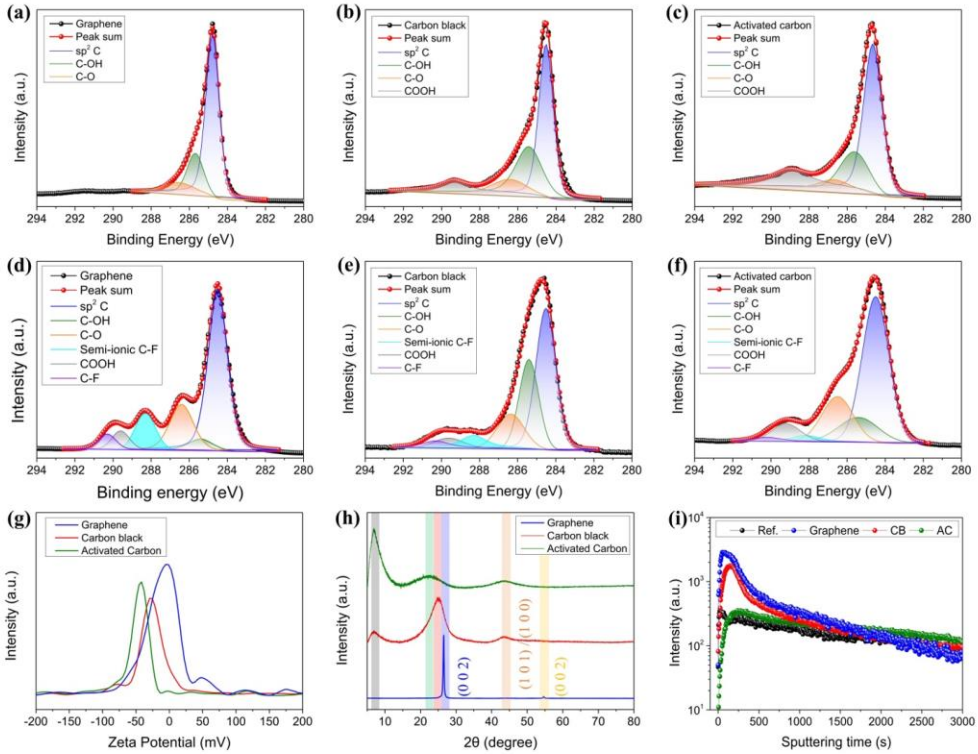

Figure 2.32 Optophysical analyses for other conjugated carbon network materials: graphene-, carbon black-, and activated carbon-coated applied systems. The C XPS data (a–c) before the cycles and (d–f) after the cycles. (g) Zeta-potential data of the intrinsic carbon materials. (h) XRD data of the intrinsic carbon materials. (i) TOF-SIMS data.

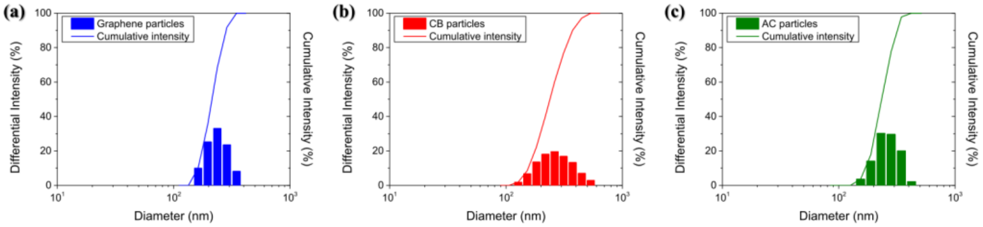

Figure 2.33 Particle size distribution of the carbon materials measured by dynamic light scattering spectrophotometer (DLS) after the grinding process; (a) Graphene. (b) Carbon black. (c) Activated carbon.

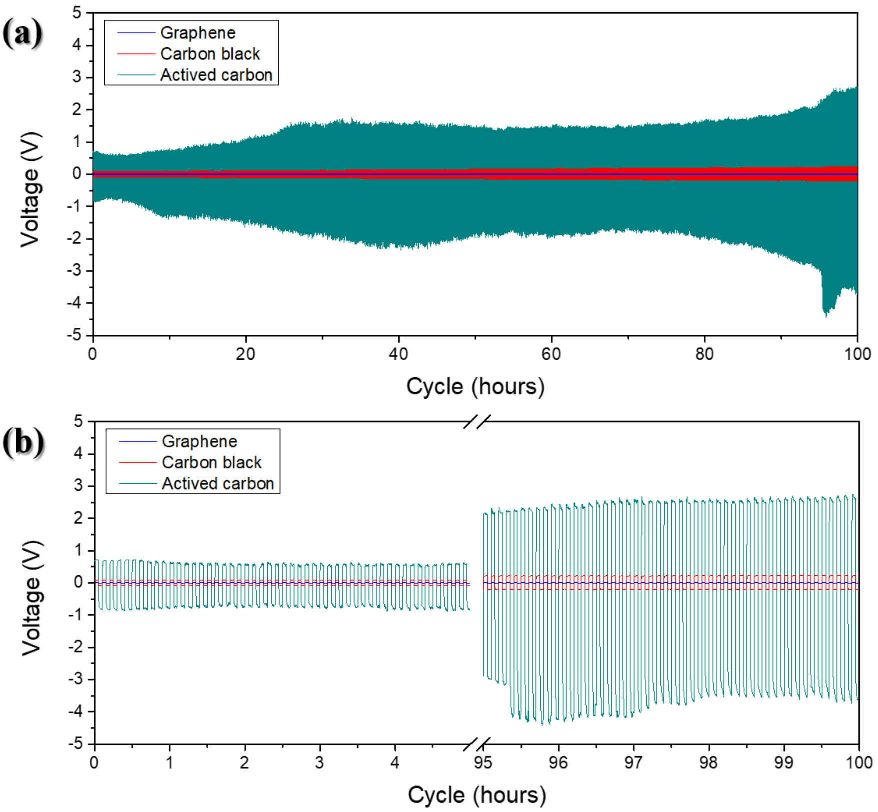

Figure 2.34 Li|Li symmetrical cell test at the high current density of 20 mA cm^{-2} (1 mAh cm^{-2}) in graphene, carbon black, and activated carbon applied system.

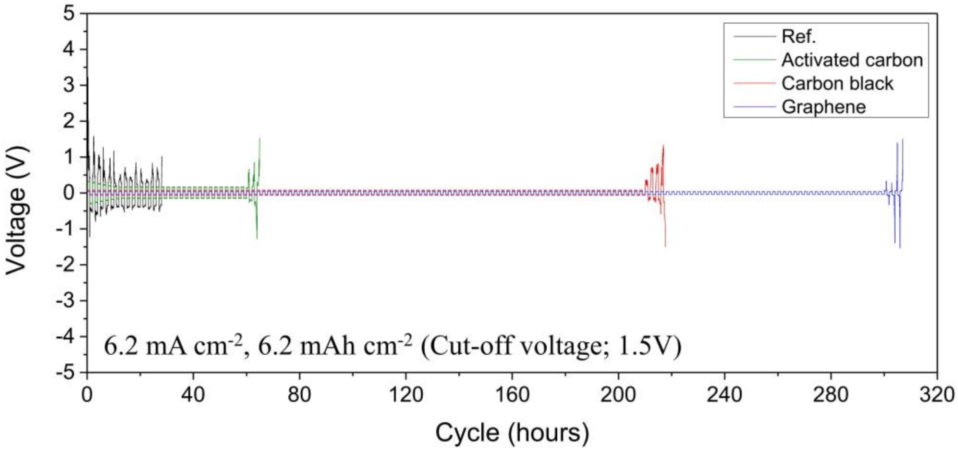

Figure 2.35 Life-span test.

2.2.8 Stabilization of the Li metal anode surface using a pencil

Based on the interpretation of the correlation between the CCN materials and F-doping mechanism, a simple, low-cost, and reasonably effective method was proposed to stabilize the LMA surface with no need for a platform. This method uses a pencil. A pencil can be easily available, and especially produces percolated CCN materials of various graphite flakes including multilayer graphene, just by drawing on paper.[74–76] Here, two types of pencils were used: a graphite pencil composed of crystalline graphite and a charcoal pencil known as amorphous graphite (Figure 2.36a). In Figure 2.36b, the zeta-potential indicated that a graphite pencil rod was approximately –20.14 mV and a charcoal pencil rod has a more negative charge of approximately –35.52 mV. Besides, XRD data revealed that a graphite pencil rod shows an intense and sharp characteristic peak assigned to the (002) plane at $2\theta = 26.5°$, whereas a charcoal pencil rod shows an amorphousized graphite structure (Figure 2.36c). According to the inference in the preceding paragraph, the percolated CCN materials on paper-mill-aramid made by drawing with a graphite pencil present the appropriate conditions for the proposed F-doping mechanism to occur. Thus, one side of the paper-mill-aramid was drawn on using a graphite pencil, and then a Li|Li symmetrical cell and Li/LFP cell were assembled where the side drawn on using the graphite pencil was towards the LMA surface. As shown in Figure 2.26d and e, when using a graphite pencil, the Li|Li symmetrical cell showed stable behavior accompanied by a low ohmic potential drop and regular anodic polarization at a current density of 5 mA cm^{-2} (1 mAh cm^{-2}). Additionally, the Li/LFP cell exhibited low capacity fading at a 20 C-rate within a potential window of 2.5 V to 4.2 V, with high capacity retention (99.64 → 80.37 mAh g^{-1}) observed after 500 cycles. By contrast, using a charcoal pencil resulted in the Li|Li symmetrical cell showing unstable behavior, and the Li/LFP cell showing higher capacity fading (99.82 → 58.92 mAh g^{-1}) after 500 cycles according to the difficulty in performing the F-doping mechanism. Figure 2.37 indicates the coulombic efficiency of Li metal batteries in the case of the charcoal pencil and the graphite pencil being applied. These results are consistent with earlier observations and demonstrated that the LMA surface can easily be stabilized by using a graphite pencil.

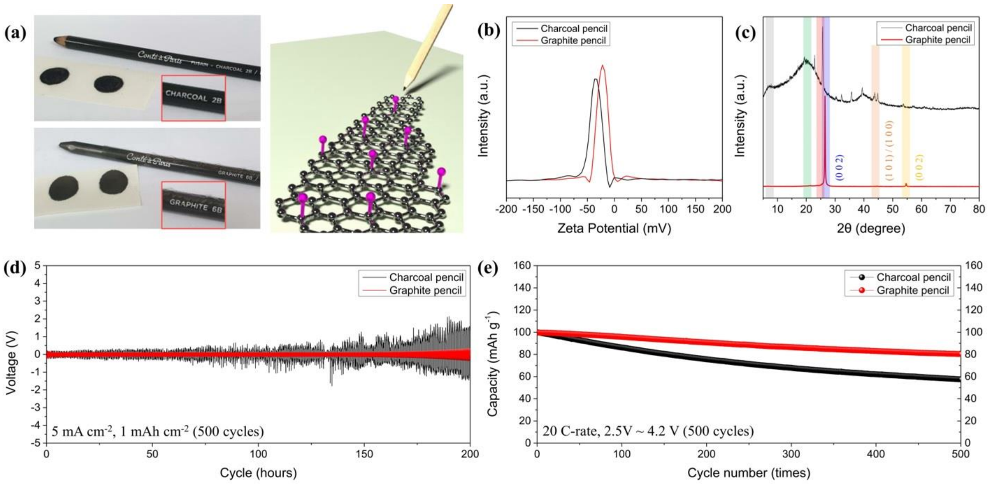

Figure 2.36 Pencil application system. (a) An image of the pencil-drawn part on paper-mill-aramid and its depiction of the fluorination state through the F-doping mechanism. (b) Zeta-potential data of a charcoal pencil and a graphite pencil. (c) XRD data of a charcoal pencil and a graphite pencil. (d) Time–voltage profiles for Li|Li symmetrical cells. (e) The cycling performance of LFP full cells. (The N/P ratio is 30)

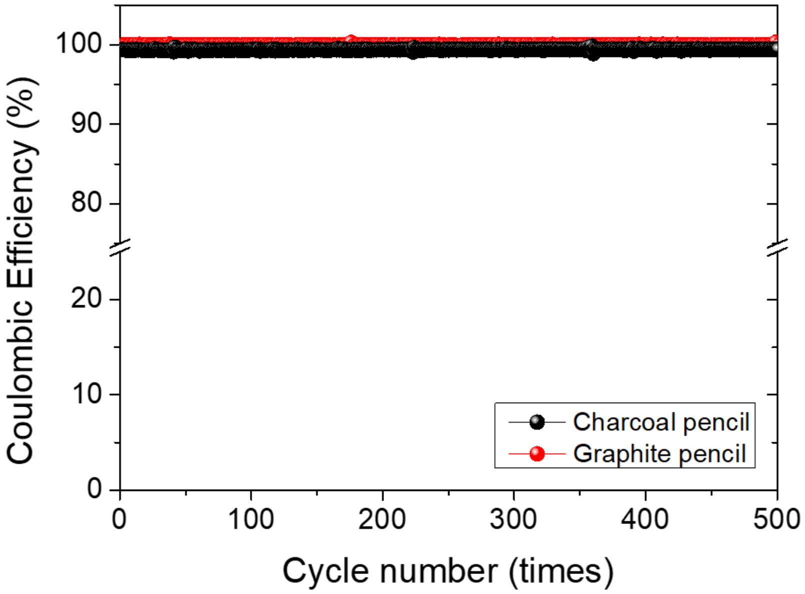

Figure 2.37 Coulombic efficiency of Li metal batteries in the case of the charcoal pencil and the graphite pencil applied.

2.3 Conclusion

In summary, I induced the formation of LiF, as a stable SEI component, from a semi-ionic C–F bond *via* fluorinated metathesis (the F-doping mechanism) in a specific solvent environment and using a CCN fiber system coated using a simple painting method. To prepare the functional separator through which this mechanism can be applied, graphene was used as a conductive CCN material along with high modulus paper-mill-aramid to help suppress dendritic growth and act as a frame for painting with graphene paste. Electrochemical tests and optophysical analyses showed that a LMA using this functional separator demonstrated high stability and performance, even at a high current density and high areal capacity (20 mA cm^{-2} and 20 mAh cm^{-2}). Moreover, I identified other CCN materials capable of stabilizing the LMA surface through LiF formation *via* fluorinated metathesis, finding that their functional groups and crystallinity of the lattice structure affected the LMA reliability. In terms of generalizing the stabilization of the Li metal anode using CCN materials, the materials' functional group type and crystallinity of the lattice structure affect the reliability of the Li metal anode. [34,77–81] Specifically, the presence of a negative charge and an amorphousized lattice structure in the CCN materials increases the difficulty of fluorinated metathesis, precluding formation of the semi-ionic C–F bond and LiF formation and adversely affecting the LMA reliability. The results indicated that a complete lattice structure of pure carbon is optimal for fluorinated metathesis, and I ultimately revealed that use of a graphite pencil was sufficient as a simple, low-cost, and effective method for improving the reliability of a LMA as a LIB anode.

2.4 Experimental details

Preparation of the graphene-coated-fibers

Graphene powder was purchased from Graphene Supermarket (graphene nanopowder 99.9%, AO-2), and 3-methoxy-3-methyl-1-butanol (MMB) was purchased from Alfa Aesar (98+%). Commercial phenol-formaldehyde resin (PR) was used as binder. Carbon black (CB) (Timcal, super-P) and commercial activated carbon (AC) were used as other extended conjugated carbon network (CCN) materials. To prevent hydration, all carbon materials were stored in a convection oven (120 ℃) before use. Before the mixture preparation, graphene powder was subjected to physical friction with two 5 mm Zr-ball and five 1 mm Zr-ball for 30 min at 2000 rpm in a 15 mL PTFE Teflon jar to prevent flake agglomeration and to ensure the uniformity of flakes by homogenizer (Thinky Mixer AR-100). This grinding process had been carried out five times. After that, graphene powder and phenol-formaldehyde resin were mixed with a weight ratio of 13:4, and then this high-viscosity mixture was diluted to 70 wt% in MMB solvent and dispersed homogeneously for 20 minutes by tip sonication (VC-750, Sonics & Materials, Inc.). The dispersion using by tip sonication was done three times. As-prepared graphene paste was painted on a paper-mill-aramid (Mitsubishi, paper-mill-aramid: HP3015, 30 μm thickness) by brush, and the graphene coated paper-mill-aramid was dried at 150 ℃ for 8 h in a convection oven. The carbon black- and the activated carbon-coated paper-mill-aramid were also prepared and painted by the same method, and dried at the same condition. After drying, the graphene coated paper-mill-aramid was attached to the uncoated paper-mill-aramid by applying a pressure of 30 MPa for 1 h at 50 ℃ by a hot-press. During this process, a trace amount of acetone and ethanol was drop-casted on the uncoated paper-mill-aramid. Paper-mill-aramid was a structure of fibers woven together using polyester and cellulose as adhesives. So, when the coated aramid was on the uncoated aramid wetted with acetone and ethanol, sufficient temperature and pressure were applied, making it to be easily attached and not to fall apart from each other. Finally, a double layer separator of about 40 ± 2 μm thickness was obtained. The resistance of the coated side was about 25 ~ 32 Ω cm^{-1} (graphene; 25 Ω cm^{-2}, carbon black and activated carbon; 26 ~ 32 Ω cm^{-2}) and the uncoated side was completely insulating.

Preparation of LiFePO4 to high C-rate test

$LiFePO_4$ (LFP) nanoparticles were firstly prepared as a cathode material by the solvothermal synthesis method and were secondary processed by additional treatment to a high C-rate test. Lithium hydroxide monohydrate ($LiOH \cdot H_2O$, 99%), phosphoric acid (H_3PO_4, 85%), and iron sulfate heptahydrate ($FeSO_4 \cdot 7H_2O$, 99%) were purchased from Sigma Aldrich, ACROS, and Alfa Aesar, respectively. These materials were used as precursors in the stoichiometric ratio of 2.7:1:1.5, respectively. For the solvothermal synthesis, appropriated quantity of $LiOH \cdot H_2O$ was dissolved in 45 mL of commercial ethylene glycol (99%). H_3PO_4 was added dropwise into the solution of the previous step under stirring. $FeSO_4 \cdot 7H_2O$ was dissolved in 30 mL of ethylene glycol and then the $LiOH \cdot H_2O$ solution was added into the iron sulfate solution under stirring. The obtained green suspension was transferred into a Teflon-lined stainless steel autoclave and then heated at 180 °C for 10 h. After the heating process, the autoclave was cooled at room temperature. The obtained gray precipitates were washed with ethyl alcohol and deionized (DI) water for the several times. The LFP residues were dried in the freeze drier and the nanoparticle state of the LFP powder was finally obtained. For a high C-rate test, LFP synthesized through the above steps was additionally processed with N-doped carbon (NC) and reduced graphene oxide (rGO). Graphene oxide (GO) was synthesized by a modified Hummers' method. Dopamine hydrochloride and Tris-buffer were purchased from Sigma Aldrich. As-prepared LFP powder was dispersed in Tris-buffer solution (10 mM) by sonication. Then, dopamine hydrochloride (3 mg mL^{-1}, 200 mL H_2O) was added to the suspension of the previous step and stirred for 15 min. GO suspension (3 wt% in H_2O) was added into the dopamine solution for 10 min. After 5 min of reaction, the suspension of LFP, dopamine, and graphene oxide suspension was washed three times with DI water and dried at 70 °C in an oven for 10 h. The collected LFP@polydopamine@GO composite was calcined at 700 °C for 5 h in Ar-filled Swagelok container to form LFP@NC@rGO. All LFP used in this experiment were applied to Li/LFP cell after the post-treatment with N-doped carbon and reduced graphene oxide. In the coin cell fabrication, LFP cathode was prepared by mixing the as-prepared active materials with carbon black (CB) as a conductive material (Timcal, super-P), and poly(vinylidenefluoride) as a binder (PVDF, Kynar HSV900). This mixture was dissolved in commercial N-methyl-2-pyrrolidone (NMP, 99%) at a concentration of 7 wt% in a weight ratio of 70:15:15 (LFP:CB:PVDF). The mixed slurry was coated onto an aluminum foil current collector and dried at 120 °C under vacuum for 10 h. In the pouch cell fabrication, as a binder, poly(vinylidene fluoride-co-hexafluoropropylene) (PVdF-HFP; Mw = 400000 and Mn = ~130,000 g mol^{-1}, Sigma Aldrich) was used instead of PVDF. The mixed slurry was drop-casted on a Teflon plate. After drying, the free-standing LFP was peeled off and transferred to a freeze drier to obtain the final flexible LFP cathode.

The initialization steps of LiFePO4 interface

The LFP cathode made for the high C-rate test undergone a two-stage stabilization process for the initialization of the LFP interface before the cycling. As-assembled Li/LFP cell undergone the rest stage for liquid electrolyte soaking for 24 h at room temperature. Then, as first stabilization process, Li/LFP cell was cycled five times at a 0.1 C-rate within a potential window of 2.0 to 4.2 V to the LFP interface for initialization. After that, as a second stabilization process, the Li/LFP cell was cycled five times at a 0.2 C-rate within a potential window of 2.5 to 4.2 V to the LFP interface for initialization. After the two stages of stabilization, the Li/LFP cell was tested within a potential window of 2.5−4.2 V vs. Li^+/Li. The loading density of the active materials was about 1.5 mg cm^{-2}, and testing temperature was 30 ºC.

Electrochemical measurement

The CR2032 coin cell was assembled with a Li/Cu asymmetrical cell, Li|Li symmetrical cell, and Li/$LiFePO_4$ cell using paper-mill-aramid separators (Mitsubishi, paper-mill-aramid: HP3015 - 30 μm thickness, HKMS50 - 50 μm thickness)) and 1M $LiPF_6$ (in EC/DEC/DMC =1/1/1 v/v/v) (Panax Etec Co. Ltd. STARLYTE or Simga Aldrich). HP3015 (30 μm) was used for the paste coating and for the uncoated aramid as separator in GAA system, and HKMS50 (50 μm) was used as the reference system and for the pencil drawing. Galvanostatic cycling measurements in the Li|Li symmetrical cell test were performed (1) at a current density of 5 mA cm^{-2} (1 mAh cm^{-2}), (2) at a high current density of 20 mA cm^{-2} (1 mAh cm^{-2}) as the rapid charging/discharging test, (3) at a high areal capacity and at a high current density of 20 mA cm^{-2} (20 mAh cm^{-2}). The amount of Li plated was 0.00259 g under 1 mA cm^{-2} for 10 h. Based on this, the plated Li was 0.000259 g for 1 mA cm^{-2} for 1 h. Thus, 1.000258 mAh was set to 1 C-rate (3862 mAh g^{-1} × 0.000259 g). In Li/Cu asymmetric cell, Li foil was used as the counter electrode and the reference electrode. In symmetrical cell, Li metal foil (MTI Korea - 300 μm) was used as the working, counter, and reference electrode. In life span test, custom-made thin Li metal electrode on Cu was supplied by Welcos (thickness - Li; 30 μm and Cu; 10 μm). Galvanostatic cycling measurements in Li metal battery test were performed at 20 C-rates with LFP@NC@rGO. A commercial available pouch cell having a nominal dimension of 65 mm × 50 mm × 1.5 mm were assembled. LFP, Li metal and GAA were used as cathode, anode, and separator, respectively. GAA separator was used after soaking in the electrolyte for a sufficient time. All manufacturing processes were carried out in an Ar-filled glove box under vacuum with 0.1 ppm or less of oxygen and 1 ppm or less of humidity.

The resistance measurement

The sheet resistance was measured using a source meter (Keithley 2400). First, conductive silver paste was painted at vertices of Square-shaped GAA (the coated side). Electrode tip was contacted to sample and a current of 1 mA was applied to measure the voltage drop. The R_A value and R_B value obtained from this measurement were substituted into Van der Paw's law to get the sheet resistance.

X-ray photoelectron spectroscopy (XPS) analysis

X-ray photoelectron spectroscopy (Kratos, Axis Supra™) analysis was used to investigate the elemental species, binding state, and distribution of S4 specific elements in the prepared sample. All samples, which were vertically cut to 0.8 cm × 0.8 cm specimens at the center by a razor blade, were measured without any additional treatment to observe the surface as it was in ultra-high vacuum (UHV) chamber under 5×10^{-10} torr and excited by monochromatic Al Kα radiation (1486.6 eV) source with operation at 15 kV. Reference and sample were analyzed using XPS equipment with higher resolution. The binding energy of XPS spectra was calibrated using a carbon peak (*sp*^{2} C at 284.5 eV) as the reference, peak fitting of all spectra was undertaken on XPSPEAK4.1 program grounded the Shirley background and Lorentzian-Gaussian curve synthesis.

X-ray diffractometer (XRD) analysis

Carbon materials stored in a convection oven (120 °C) went through the same grinding process as in the process of making paste, and samples were scanned and recorded using an X-ray diffractometer (Smartlab, Rigaku) with an X-ray generator from 0 to 80 of 2θ (diffraction angle) using CuKα radiation under the following conditions: 40 kV and 30mA ($\lambda = 0.154$ nm). A pencil rod also went through the same grinding process, and its powder was scanned and recorded in the same way.

Electron microscope analysis

High resolution scanning electron microscopy (HR-SEM with JEOL Ltd) analysis and scanning transmission electron microscopy (Cs corrected STEM with Cold FEG, JEOL Ltd) analysis were carried out at 15 kV (SEM) and 80 kV (TEM). After electrochemical tests, the cells were carefully disassembled by de-crimping machine (MTI Korea MSK-110) in an Ar-filled glove-box. To prevent oxidation of surface of Li metal, Li metal is taken out from an Ar-filled glove-box while being immersed in an ionic liquid (1-Ethyl-3-methylimidazolium bis(trifluoromethylsulfonyl) imide, [EMI][TFSI]), and then SEM analysis was conducted. Other samples were sealed with Ar gas, and then taken out of the Ar-filled glove-box. For cross-sectional analysis of the GAA single strand fiber, a dual beam focused ion beam (FIB, Helios 5 UX, Thermofisher) equipment was used to prepare samples for TEM investigation.

Microscopic Fourier-transform infrared spectroscopy (FT-IR) analysis

For cross-sectional analysis of GAA and uncoated aramid fiber by microscopic FT-IR (Perkin Elmer), the coated side of GAA separator and the uncoated aramid fiber were cut using by the surface and interfacial characterizing analysis system (SAICAS, Daipla wintes). After the cutting process, the coated fiber of GAA separator and aramid fiber was scanned from 600 to 2000 cm^{-1}. The confirmation of graphene coating of the uncoated aramid fiber was scanned from 400 to 4000 cm^{-1} in normal mode.

Time-of-flight secondary ion mass spectrometer (TOF-SIMS) analysis

A time-of-flight secondary ion mass spectrometer (TOF.SIMS 5, ION-TOF) at a pressure below 3.8×10^{-9} Torr was used for analysis of the depth and 3D depth mapping of the chemical composition of Li metal anodes by the negative polarity. A Bi^+ (30 keV, 1 pA) ion beam was used as the primary source for detecting the composition of facile-section, and sputtering with a Cs^+ ion beam (2 keV, 150 nA) was used for depth profiling analysis (analysis area; 100×100 μm^2, etching area; 400×400 μm^2).

Zeta-potential measurements and Dynamic light scattering spectrophotometer (DLS)

Graphene, carbon black, and activated carbon powders were subjected to physical friction with two 5 mm Zr-ball and five 1mm Zr-ball for 30 minutes at 2000 rpm in 15 mL PTFE teflon jar. Like the paste preparation, grinding process had been carried out five times. And powders were dispersed in water (DLS: ethyl alcohol) at an appropriated concentration by tip sonication for 20 minutes. Like the paste preparation, tip sonication also was done three times. After that, Zeta-potential and DLS were measured to each aqueous (DLS: ethyl alcohol) solution by electrophoretic light scattering spectrophotometer (Els z-1000, Otsuka Portal) and by dynamic light scattering spectrophotometer, respectively.

Atomic force microscopy (AFM) analysis

The thickness of graphene flake was investigated using AFM (XE100, PSIA).

Raman spectroscopy analysis

The graphene powder was characterized by Raman (DXR2xi, Thermo, USA).

2.5 References

[1] X. B. Cheng, R. Zhang, C. Z. Zhao, Q. Zhang, *Chem. Rev.* **2017**, *117*, 10403.

[2] Z. Li, J. Huang, B. Yann Liaw, V. Metzler, J. Zhang, *J. Power Sources* **2014**, *254*, 168.

[3] P. Verma, P. Maire, P. Novák, *Electrochim. Acta* **2010**, *55*, 6332.

[4] B. Lee, E. Paek, D. Mitlin, S. W. Lee, *Chem. Rev.* **2019**, 5416.

[5] R. Xu, X. Q. Zhang, X. B. Cheng, H. J. Peng, C. Z. Zhao, C. Yan, J. Q. Huang, *Adv. Funct. Mater.* **2018**, *28*, 1.

[6] K. Xu, *Chem. Rev.* **2014**, *114*, 11503.

[7] S. S. Zhang, *J. Power Sources* **2006**, *162*, 1379.

[8] D. Wang, W. Zhang, W. Zheng, X. Cui, T. Rojo, Q. Zhang, *Adv. Sci.* **2017**, *4*, 1600445.

[9] X. B. Cheng, T. Z. Hou, R. Zhang, H. J. Peng, C. Z. Zhao, J. Q. Huang, Q. Zhang, *Adv. Mater.* **2016**, *28*, 2888.

[10] D. J. Lee, H. Lee, Y. J. Kim, J. K. Park, H. T. Kim, *Adv. Mater.* **2016**, *28*, 857.

[11] C. Li, S. Liu, C. Shi, G. Liang, Z. Lu, R. Fu, D. Wu, *Nat. Commun.* **2019**, *10*, 1.

[12] H. Kim, Y. J. Gong, J. Yoo, Y. S. Kim, *J. Mater. Chem. A* **2018**, *6*, 15540.

[13] Y. J. Gong, H. Kim, G. Yoo, J. Cho, S. Pyo, Y. H. Cho, J. Yoo, Y. S. Kim, *ACS*

Appl. Energy Mater. **2019**, *2*, 8310.

[14] Y. J. Gong, J. W. Heo, H. Lee, H. Kim, J. Cho, S. Pyo, H. Yun, H. Kim, S. Y. Park, J. Yoo, Y. S. Kim, *Adv. Energy Mater.* **2020**, *10*, 1.

[15] Y. Deng, H. Lu, Y. Cao, B. Xu, Q. Hong, W. Cai, W. Yang, *J. Power Sources* **2019**, *412*, 170.

[16] S. Matsuda, Y. Kubo, K. Uosaki, S. Nakanishi, *Carbon N. Y.* **2017**, *119*, 119.

[17] Y. Wang, Y. Shen, Z. Du, X. Zhang, K. Wang, H. Zhang, T. Kang, F. Guo, C. Liu, X. Wu, W. Lu, L. Chen, *J. Mater. Chem. A* **2017**, *5*, 23434.

[18] H. Zhang, X. Liao, Y. Guan, Y. Xiang, M. Li, W. Zhang, X. Zhu, H. Ming, L. Lu, J. Qiu, Y. Huang, G. Cao, Y. Yang, L. Mai, Y. Zhao, H. Zhang, *Nat. Commun.* **2018**, *9*, 1.

[19] Y. Liu, X. Li, L. Fan, S. Li, H. Maleki Kheimeh Sari, J. Qin, *Front. Chem.* **2019**, *7*, 1.

[20] J. Xie, L. Liao, Y. Gong, Y. Li, F. Shi, A. Pei, J. Sun, R. Zhang, B. Kong, R. Subbaraman, J. Christensen, Y. Cui, *Sci. Adv.* **2017**, *3*, 1.

[21] O. Sheng, J. Zheng, Z. Ju, C. Jin, Y. Wang, M. Chen, J. Nai, T. Liu, W. Zhang, Y. Liu, X. Tao, *Adv. Mater.* **2020**, *32*, 1.

[22] T. Xu, P. Gao, P. Li, K. Xia, N. Han, J. Deng, Y. Li, J. Lu, *Adv. Energy Mater.* **2020**, *10*, 1.

[23] D. Lin, Y. Liu, Y. Cui, *Nat. Nanotechnol.* **2017**, *12*, 194.

[24] H. Wang, D. Lin, Y. Liu, Y. Li, Y. Cui, *Sci. Adv.* **2017**, *3*, 1.

[25] T. Wang, R. Villegas Salvatierra, A. S. Jalilov, J. Tian, J. M. Tour, *ACS Nano* **2017**, *11*, 10761.

[26] G. M. Stone, S. A. Mullin, A. A. Teran, D. T. Hallinan, A. M. Minor, A. Hexemer, N. P. Balsara, *J. Electrochem. Soc.* **2012**, *159*, A222.

[27] C. Monroe, J. Newman, *J. Electrochem. Soc.* **2005**, *152*, A396.

[28] J. Liu, L. Tao, W. Yang, D. Li, C. Boyer, R. Wuhrer, F. Braet, T. P. Davis, *Langmuir* **2010**, *26*, 10068.

[29] Y. Xu, H. Bai, G. Lu, C. Li, G. Shi, *J. Am. Chem. Soc.* **2008**, *130*, 5856.

[30] Q. Su, S. Pang, V. Alijani, C. Li, X. Feng, K. Müllen, *Adv. Mater.* **2009**, *21*, 3191.

[31] J. Fan, Z. Shi, M. Tian, J. Yin, *RSC Adv.* **2013**, *3*, 17664.

[32] N. N. Lapteva, L. I. Kulikova, *Vestn. Akad. Med. Nauk SSSR* **1975**, 76.

[33] J. Zhang, Q. Kong, Z. Liu, S. Pang, L. Yue, J. Yao, X. Wang, G. Cui, *Solid State Ionics* **2013**, *245–246*, 49.

[34] W. Liu, Y. Xia, W. Wang, Y. Wang, J. Jin, Y. Chen, E. Paek, D. Mitlin, *Adv. Energy Mater.* **2019**, *9*, 1.

[35] P. Gong, Z. Wang, Z. Li, Y. Mi, J. Sun, L. Niu, H. Wang, J. Wang, S. Yang, *RSC Adv.* **2013**, *3*, 6327.

[36] M. Mukherjee, S. Kumar, S. Bose, C. K. Das, A. P. Kharitonov, *Polym. - Plast. Technol. Eng.* **2008**, *47*, 623.

[37] N. Sharma, V. Sharma, Y. Jain, M. Kumari, R. Gupta, S. K. Sharma, K. Sachdev, **2017**, *1700006*, 1.

[38] Y. Wang, W. C. Lee, K. K. Manga, P. K. Ang, J. Lu, Y. P. Liu, C. T. Lim, K. P. Loh, *Adv. Mater.* **2012**, *24*, 4285.

[39] S. Abramowitz, N. Acquista, I. W. Levin, *J. Res. Natl. Bur. Stand. Sect. A Phys. Chem.* **1968**, *72A*, 487.

[40] D. Lin, J. Zhao, J. Sun, H. Yao, Y. Liu, K. Yan, Y. Cui, *Proc. Natl. Acad. Sci. U. S. A.* **2017**, *114*, 4613.

[41] K. H. Chen, K. N. Wood, E. Kazyak, W. S. Lepage, A. L. Davis, A. J. Sanchez, N. P. Dasgupta, *J. Mater. Chem. A* **2017**, *5*, 11671.

[42] K. N. Wood, E. Kazyak, A. F. Chadwick, K. H. Chen, J. G. Zhang, K. Thornton, N. P. Dasgupta, *ACS Cent. Sci.* **2016**, *2*, 790.

[43] Z. Chu, X. Feng, B. Liaw, Y. Li, L. Lu, J. Li, X. Han, M. Ouyang, *J. Electrochem. Soc.* **2018**, *165*, A3240.

[44] J. Oh, J. Lee, T. Hwang, J. M. Kim, K. dong Seoung, Y. Piao, *Electrochim. Acta* **2017**, *231*, 85.

[45] C. Ma, Y. Feng, F. Xing, L. Zhou, Y. Yang, Q. Xia, L. Zhou, L. Zhang, L. Chen,

D. G. Ivey, D. R. Sadoway, W. Wei, *J. Mater. Chem. A* **2019**, *7*, 19970.

[46] N. Li, Z. Chen, W. Ren, F. Li, H. M. Cheng, *Proc. Natl. Acad. Sci. U. S. A.* **2012**, *109*, 17360.

[47] Y. Zhang, Q. Wang, R. Li, Z. Lou and Y. Li, *Crystals*, **2020**, *10*, 159.

[48] A. Ganguly, S. Sharma, P. Papakonstantinou, J. Hamilton, *J. Phys. Chem. C* **2011**, *115*, 17009.

[49] W. Feng, P. Long, Y. Y. Feng, Y. Li, *Adv. Sci.* **2016**, *3*, 1.

[50] R. Younesi, M. Hahlin, M. Roberts, K. Edström, *J. Power Sources* **2013**, *225*, 40.

[51] K. Tasaki, K. Kanda, S. Nakamura, M. Ue. *J. Electrochem. Soc.* **2003**, *150,* A1628.

[52] Y. Sato, K. Itoh, R. Hagiwara, T. Fukunaga, Y. Ito, *Carbon N. Y.* **2004**, *42*, 3243.

[53] M. Dubecký, E. Otyepková, P. Lazar, F. Karlický, M. Petr, K. Čépe, P. Banáš, R. Zbořil, M. Otyepka, *J. Phys. Chem. Lett.* **2015**, *6*, 1430.

[54] E. Jeong, B. H. Lee, S. J. Doh, I. J. Park, Y. S. Lee, *J. Fluor. Chem.* **2012**, *141*, 69.

[55] G. Feng, R. Qiao, J. Huang, S. Dai, B. G. Sumpter, V. Meunier, *Phys. Chem. Chem. Phys.* **2011**, *13*, 1152.

[56] C. Shen, S. Wang, Y. Jin, W. Q. Han, *ACS Appl. Mater. Interfaces* **2015**, *7*, 25441.

[57] Y. Okamoto, *J. Electrochem. Soc.* **2013**, *160,* A404.

[58] S. Leroy, F. Blanchard, R. Dedryvère, H. Martinez, B. Carré, D. Lemordant, D. Gonbeau, *Surf. Interface Anal.* **2005**, *37*, 773.

[59] D. E. Arreaga-Salas, A. K. Sra, K. Roodenko, Y. J. Chabal, C. L. Hinkle, *J. Phys. Chem. C* **2012**, *116*, 9072.

[60] R. Dedryvère, S. Leroy, H. Martinez, F. Blanchard, D. Lemordant, D. Gonbeau, *J. Phys. Chem. B* **2006**, *110*, 12986.

[61] C. Gómez-Navarro, R. T. Weitz, A. M. Bittner, M. Scolari, A. Mews, M. Burghard, K. Kern, *Nano Lett.* **2007**, *7*, 3499.

[62] Y. Chernyak, *J. Chem. Eng. Data* **2006**, *51*, 416.

[63] L. H. Hess, A. Balducci, *Electrochim. Acta* **2018**, *281*, 437.

[64] A. N. Enyashin, A. L. Ivanovskii, *Chem. Phys. Lett.* **2012**, *545*, 78.

[65] T. Nakajima, *J. Fluor. Chem.* **1999**, *100*, 57.

[66] T. Nakajima, M. Koh, V. Gupta, B. Žemva, K. Lutar, *Electrochim. Acta* **2000**, *45*, 1655.

[67] J. Kim, R. Zhou, K. Murakoshi, S. Yasuda, *RSC Adv.* **2018**, *8*, 14152.

[68] U. Rajeena, M. Akbar, P. Raveendran, R. M. Ramakrishnan, *New J. Chem.* **2018**, *42*, 9658.

[69] T. Qiu, J. G. Yang, X. J. Bai, Y. L. Wang, *RSC Adv.* **2019**, *9*, 12737.

[70] X. Jiao, Y. Qiu, L. Zhang, X. Zhang, *RSC Adv.* **2017**, *7*, 52337.

[71] P. Chen, H. Li, S. Song, X. Weng, D. He, Y. Zhao, *Results Phys.* **2017**, *7*, 2281.

[72] H. H. Huang, K. K. H. De Silva, G. R. A. Kumara, M. Yoshimura, *Sci. Rep.* **2018**, *8*, 2.

[73] P. Albertus, S. Babinec, S. Litzelman, A. Newman, *Nat. Energy* **2018**, *3*, 16.

[74] K. H. Choi, H. W. Kim, S. S. Lee, J. T. Yoo, D. G. Lee, S. Y. Lee, *Adv. Sustain. Syst.* **2018**, *2*, 1.

[75] B. Yao, L. Yuan, X. Xiao, J. Zhang, Y. Qi, J. Zhou, J. Zhou, B. Hu, W. Chen, *Nano Energy* **2013**, *2*, 1071.

[76] Annu, S. Sharma, R. Jain, A. N. Raja, *J. Electrochem. Soc.* **2020**, *167*, 037501.

[77] A. Zhamu, G. Chen, C. Liu, D. Neff, Q. Fang, Z. Yu, W. Xiong, Y. Wang, X. Wang, B. Z. Jang, *Energy Environ. Sci.* **2012**, *5*, 5701.

[78] R. Zhang, X. B. Cheng, C. Z. Zhao, H. J. Peng, J. Le Shi, J. Q. Huang, J. Wang, F. Wei, Q. Zhang, *Adv. Mater.* **2016**, *28*, 2155.

[79] T. Xu, L. Sun, *Defects Adv. Electron. Mater. Nov. Low Dimens. Struct.* **2018**, *5*, 137.

[80] R. Mukherjee, A. V. Thomas, D. Datta, E. Singh, J. Li, O. Eksik, V. B. Shenoy, N. Koratkar, *Nat. Commun.* **2014**, *5*, 1.

[81] R. Zhang, X.-R. Chen, X. Chen, X.-B. Cheng, X.-Q. Zhang, C. Yan, Q. Zhang, *Angew. Chemie* **2017**, *129*, 7872.

Chapter 3 Lithiophilic Wetting Agent Inducing Interfacial Fluorination for Long-Lifespan Anode-Free Lithium Metal Batteries

3.1 Introduction

Li metal batteries (LMBs) have emerged as a promising high-energy-density rechargeable batteries. [1] Since the Li metal anode (LMA) has an ultrahigh theoretical specific capacity (3862 mAh g^{-1}) and the lowest negative electrochemical potential (-3.040 V vs. standard hydrogen electrode), its employment ensures a higher energy density beyond conventional Li-ion batteries with a limited energy density of less than 250 Wh kg^{-1} at the cell level. [2] In this respect, anode-free LMBs (AFLMBs) are considered the ultimate system to achieve a dramatic increase in energy density (>500 Wh kg^{-1}), which all the active Li sources are stored in the fully lithiated cathode. [3] In addition, compared with traditional LMBs, the anode-free design significantly reduces cost and simplifies the manufacturing process. [4] However, LMBs suffer from the Li dendritic growth and the continuous formation and breakage of the solid electrolyte interphase (SEI) during Li plating/stripping processes, leading to a low coulombic efficiency (CE) and rapid capacity fading. [1,5] Thus, AFLMBs are more challenging to improve their lifespan due to no excess Li inventory to compensate the loss of active Li sources. [4,6] Therefore, such uncontrollable interfacial issues should be addressed.

Recently, many strategies have been reported to control the interfacial chemistry between Li and the electrolyte as well as between Li and the current collector, which finally determines electrochemical performance of AFLMBs (i.e. modification of current collector, electrolyte design, optimization of cycling protocols). [7–9] Among them, studies about employing lithiophilic wetting agents on the current collector has proven an effective way to stabilize Li plating behavior, which can achieve the favorable lifespan of the cells. [10–12] In particular, wetting agents show outstanding effect on guiding homogeneous Li deposition by lowering the Li nucleation barrier, and consequently suppressing dendritic Li growth. However, the critical problem of sequentially irreversible capacity loss prior to the formation of a stable SEI still remains, which is a serious obstacle in no excess Li cell. [13]

Herein, I introduce Ag nanoparticles incorporated p-doped conjugated polymer (Ag-PCP) wetting agent simultaneously to regulate the Li nucleation and promote a rapid stabilization of SEI at the early stage, and further prolong lifespan of AFLMBs. Furthermore, I demonstrate an interfacial fluorinated mechanism of the Ag-PCP chains to efficiently control the SEI chemistry, which is related to LiF formation. The

Ag-PCP wetting agent is fabricated directly on the current collector without any additional interlayers by simple one-step fabrication process *via* the electrostatic interaction between the oppositely charged Ag cations and ClO_4^- dopants, which has little effect on the total energy density of the cell. [14] Critically, the PCP chains with the delocalized π-electron system induce interfacial fluorinated reactions with the F anions derived from $TFSI^-$ decomposition, and thus the F-doped PCP promotes the formation of LiF-rich SEI. [15,16] Also, the lithiophilic Ag nanoparticles (Ag NPs) on the PCP wetting agent act as both Li nucleation seeds and polymer chain modifiers about the structural rearrangement and inter-chain distance of the Ag-PCP chains, so they provide both uniform Li nucleation and continuous conductive channels, resulting in an increase of LiF ratio in the SEI. [17,18] The LiF-rich SEI facilitates Li ion diffusion, which effectively suppresses Li dendritic growth and depletion of the Li reservoir. [19] Benefiting from the synergistic effect of Ag-Li alloying and interfacial fluorination, the Ag-PCP wetting agent optimizes Li deposition and promotes a favorable SEI chemistry, leading to superior cycling performances. Consequently, the Ag-PCP | Cu half-cell displays quite stable voltage profiles with low polarization (≈17 mV) over 300 cycles, even at high current density/areal capacity of 3mA cm^{-2}/3mAh cm^{-2}. Moreover, the anode-free $LiFePO_4$ (LFP) full cell achieves superior cycling stability with a high capacity retention of 72% (Li inventory retention rate 99.8%) at 1C-rate after 200 cycles. This strategy shows the promising applicability to interfacial stabilization for long lifespan of AFLMBs.

3.2 Experimental section

3.2.1 Characterization of the Ag-PCP wetting agent

I fabricated the Ag-PCP wetting agent on the current collector using a simple one-step method *via* the electrostatic interaction between the oppositely charged Ag cations and ClO_4^{-} dopants. [14] The PCP wetting agent on Cu foil is a dark blue, but the Ag-PCP wetting agent changes color to gray after immersing into 1 mM silver nitrate ($AgNO_3$) aqueous solution for 3 mins (Figure 3.1a and b). I confirm that the Ag NPs and PCP are uniformly deposited on Cu foil overall through the Cu, C, and Ag energy-dispersive X-ray spectroscopy (EDS) mapping of the Ag-PCP cross-section (Figure 3.1c-e). Also, the obtained Ag-PCP wetting agent on Cu foil has 2 μm thickness and a mass loading of 0.49 mg cm^{-2} (1.1% of the total current collector mass), which is advantageous for high-energy-density AFLMBs (Figure 3.1f).

I examined the differences between the PCP and Ag-PCP in the extent of alignment and π-π stacking distance. The presence of Ag NPs in the PCP chains induce a conformational structural change from the random coil conformation (benzoid structure) to the ordered expanded-coil or linear conformation (quinoid structure) as well as a decrease in the π–π stacking distance ($d_{(020)}$), which facilitates a LiF-rich

SEI formation *via* F-doping chemistry of the Ag-PCP chains. [14,18,20,21] To confirm these structural changes, I performed X-ray diffraction (XRD) and Grazing-incidence wide-angle X-ray scattering (GIWAXS), Fourier transform infrared spectrometer (FT-IR), and X-ray photoelectron spectroscopy (XPS) analysis of the PCP and Ag-PCP wetting agents. In Figure 3.2a, the XRD peak of the Ag-PCP wetting agent shifts to a higher angle from 24.7° to 25.3°, implying the reduction of π–π stacking distance [$d_{(020)}$] from 3.60 Å to 3.52 Å, as calculated by Bragg's law. [22,23] Also, the distinct peak at the 2θ value of 6.9° in both the PCP and Ag-PCP represents the $d_{(100)}$ spacing of 12.80 Å for the lamella-stacking distance along the out-of-plane direction. [24] The $d_{(020)}$ peak and $d_{(100)}$ peak for the Ag-PCP wetting agent have the higher intensities and sharpness compared with those for the PCP wetting agent, indicating that the polymer structure transforms from an amorphous coil to a more linear crystalline configuration. In addition, Figure 3.3 exhibits the 1D GIWAXS profile (Q_{xy}) of the PCP and Ag-PCP wetting agent obtained from the 2D GIWAXS spectra. The Q_{xy} value (Å^{-1}) in the GIWAXS pattern is assigned to the π–π stacking of the PCP along the in-plane direction, which is correlated with the d-spacing, as calculated by Bragg's law. [25–27] For the PCP wetting agent, the (020) peak at Q_{xy} = 1.75 Å^{-1} with weak intensity corresponds to a lattice spacing of 3.59 Å (Figure 3.2b), while the Ag-PCP wetting agent shows a stronger (020) peak (Q_{xy} = 1.81 Å^{-1} for $d_{(020)}$

= 3.47 Å), as shown in Figure 3.2c. These results again verify that the presence of Ag NPs lead to preferential ordered alignment and a decrease in the π–π stacking distance of the conjugated polymer chains. Furthermore, FT-IR analysis is conducted to investigate the conformation changes in the polymer backbones at the molecular level (Figure 3.4a). For the Ag-PCP wetting agent, the absorption bands at 1479 $\mathrm{cm^{-1}}$ and 1385 $\mathrm{cm^{-1}}$ that correspond to C=C and C–C stretching vibrations of the thiophene ring slightly shift toward a higher wavenumber (so-called blue shift). [28,29] Also, the intensity of the absorption bands at 1209 $\mathrm{cm^{-1}}$ and 1051 $\mathrm{cm^{-1}}$ increase, which are attributed to the C–O–C bending vibration and C–O–C stretching vibration in ethylenedioxy group, respectively. [30,31] These changes result from the delocalization of π-electrons overall, which verifies the conformation changes of the PCP chains due to the existence of charged Ag NPs. In Figure 3.4b and c, the increased peak intensity of C–S (285.3 eV) in the Ag-PCP is attributed to the weakened interaction between the Ag-PCP chain and $\mathrm{ClO_4^-}$ dopant. [32] In addition, two peaks from S $2p_{1/2}$ and S $2p_{3/2}$ electrons shift to higher energies as a result of the enhanced $\mathrm{ClO_4^-}$ counter ions–Ag NPs interaction and the reduced Ag–PCP:$\mathrm{ClO_4}$ interaction, respectively. Ag NPs serve as electrostatic interaction modifiers, which leads to an increased peak intensity of C 1s and the peak shift of S 2p, indicating a resonant structure transformation of the polymer chains.

Based on our observation, the schematic representation shows a mechanism of conformational structure modification due to the presence of Ag NPs in the PCP chains (Figure 3.2d), which is closely related to a favorable interfacial fluorination of the Ag-PCP wetting agent. Due to the small size of ClO_4^- dopants, the PCP wetting agent has a random coil conformation with loose π–π stacking. This distortion of the PCP chains leads to the establishment of short-range conductive channels due to the localization of positive charges. [18] However, the Ag treatment on the PCP chains induces new electrostatic interactions between the positively charged Ag cations and negatively charged ClO_4 counter ions, thus weakening the interaction between the PCP chains and ClO_4^- dopants (electrostatic screening) and intensifying the inter-chain interactions in the PCP. [14] Therefore, the conjugated polymer chains are more relaxed and elongated with highly dense packing polymer chains, which facilitates F-doping chemistry of the Ag-PCP due to the reduced effect of the ClO_4^- dopants. The improved alignment (the ordered expanded-coil or linear conformation) and densification of the Ag-PCP chains provides continuous conductive channels by delocalizing the conjugated π-electrons throughout the Ag-PCP chains, which provides the increased F-doping sites due to rapid charge transport along the chain backbone and π-stacking of the Ag-PCP. Furthermore, the Ag NPs in the PCP chains serve as the bridge between disconnected conductive pathways in the PCP chains, significantly enhancing the conductivity of the Ag-PCP wetting agent. [18] Therefore, the resistance of the Ag-PCP considerably reduces to under ~6 Ω cm^{-1} (PCP; ~14 Ω cm^{-1}), exhibiting good conductivity as a wetting agent. Critically, Ag NPs not only act as Li nucleation seeds but also as electrostatic interaction modifiers, and the elongated Ag-PCP chains with closely packing of π-conjugated structure induce a stable SEI layer *via* interfacial fluorination. Consequently, these synergistic effects of the Ag-PCP wetting agent could suppress Li dendritic growth and improve CE, which would be a highly effective strategy for enhancing cycling performances of AFLMBs.

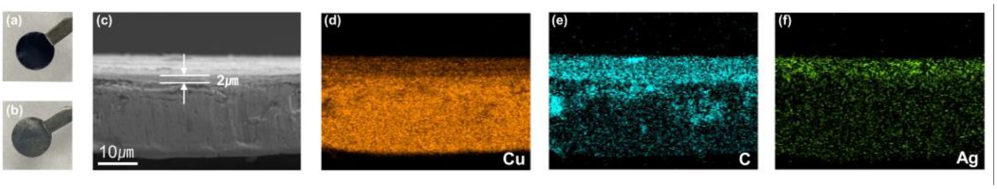

Figure 3.1 Characterization of the Ag-PCP wetting agent. The optical images of (a) PCP|Cu and (b) Ag-PCP|Cu. (c) Cu, (d) C, and (e) Ag EDS mapping images of the Ag-PCP|Cu cross-section. (f) The thickness of Ag-PCP wetting agent on Cu foil.

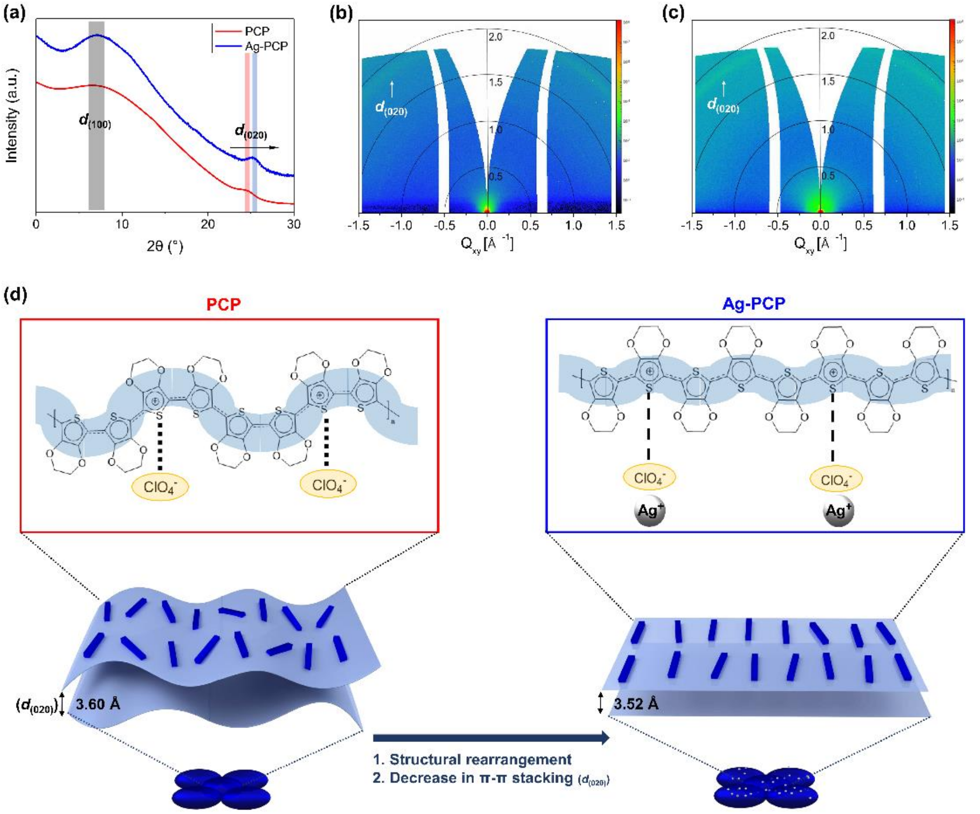

Figure 3.2 Characterization of PCP and Ag-PCP wetting agents. (a) XRD patterns of PCP wetting agents before (red) and after (blue) Ag treatment. 2D GIWAXS images of (b) PCP wetting agent and (c) Ag-PCP wetting agent. (d) Schematic of the differences between the PCP and Ag-PCP wetting agents in the extent of alignment and π-π stacking distance ($d_{(020)}$) of polymer chains.

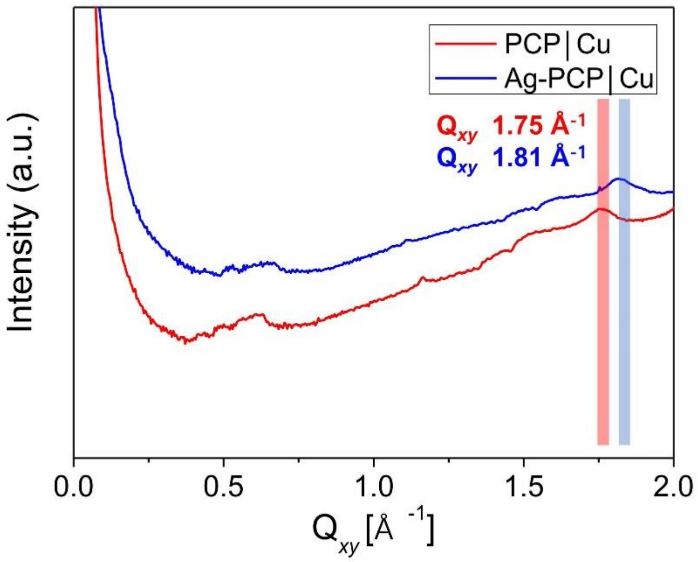

Figure 3.3 1D GIWAXS profiles of pristine PCP and Ag-PCP. Q_{xy} value corresponds to the π–π stacking distance ($d_{(020)}$) of polymer chains.

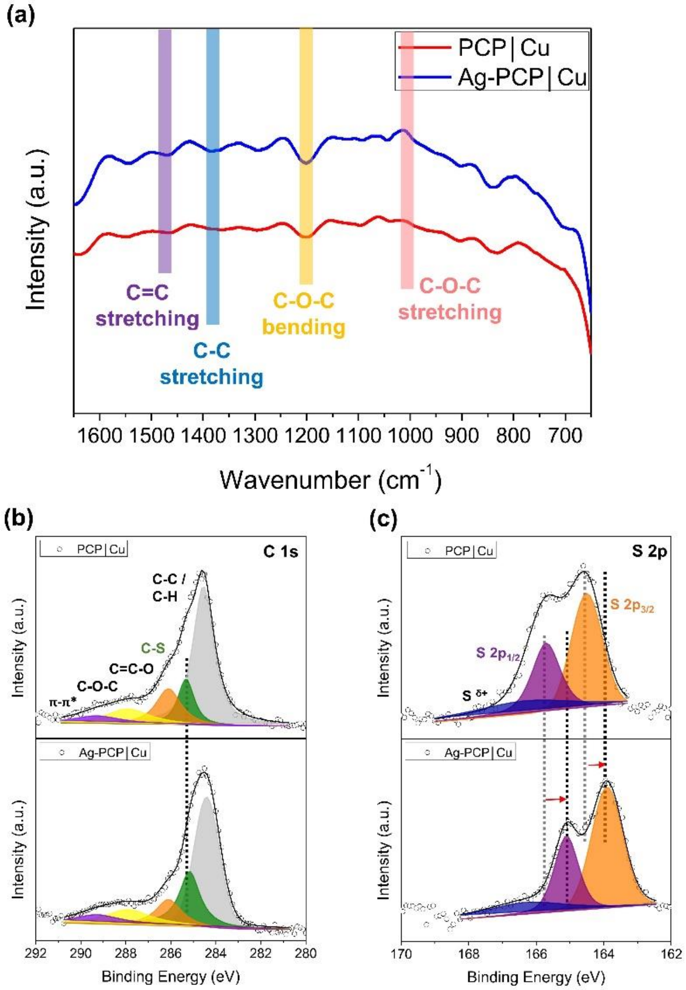

Figure 3.4 (a) FT-IR spectra of PCP wetting agents before (red) and after (blue) Ag treatment in the wavenumber region of 600–1700 cm^{-1}. XPS profiles of (b) C 1s and (c) S 2p for pristine PCP (up) and Ag-PCP (down).

3.2.2 Morphology of Li nucleation and growth

To directly demonstrate the role of the Ag-PCP wetting agent, I conducted scanning electron microscopy (SEM) and focused ion beam (FIB) after Li plating of 3 mAh cm^{-2} on bare Cu, PCP│Cu, and Ag-PCP│Cu substrates with a current density of 3 mA cm^{-2}, respectively (Figure 3.5). Comparing the inset SEM images of Figure 3.6, the PCP and Ag-PCP wetting agents exhibit porous structures unlike the bare Cu which is planar and rough. Therefore, as expected, the three-dimensional(3D) structure of the PCP│Cu and Ag-PCP│Cu effectively decrease the local current density by increasing surface area and nucleation sites during Li plating/stripping processes, which results in uniform Li deposition. [33] Moreover, they have the advantage of accommodating anode volume change during cycling due to the presence of free volume. [34] In Figure 3.5a, the initial Li plating on bare Cu exhibits irregular and dendritic morphology due to the uneven surface and high Li nucleation energy barrier. [10,35] After 300 cycles, a large number of whisker-like Li dendrites and "dead Li" form, which is accelerated by inhomogeneous charge distribution and unstable SEI formation (Figure 3.5b). [36] For the PCP│Cu substrate, the initially deposited Li morphology is more even due to the PCP wetting agent, whose 3D conductive structure is favorable for homogeneous and speedy Li ion diffusion, and thus the Li dendritic growth is considerably suppressed after 300 cycles (Figure 3.5c, d). [19,37] More prominently, the morphology of the Li deposition on the Ag-PCP│Cu is flat, smooth, dense, and dendrite-free from the first cycle and remains so even after 300 cycles (Figure 3.5e and f). Because the existence of Ag serves as polymer chain modifiers and bridges, which maximizes charge movement along inter-chain and inter-domain of the Ag-PCP. Furthermore, the granular size of Li nucleation on the Ag-PCP│Cu significantly increases in comparison with that on the PCP│Cu, which confirms the combined effects of the lithiophilic nature of Ag and the lowered local current density by the 3D conductive frameworks of Ag-PCP. [38] Such Li nuclei with a large granular size minimizes the unwanted side reaction of Li with electrolyte for the SEI formation, thus could maintain high reversibility of Li plating/stripping process in the Ag-PCP│Cu. [39]

In Figure 3.5g, the thickness of the Li deposition on bare Cu is more than 40 μm after 300 cycles, which deviates quite from the theoretical value corresponding to 3 mAh cm^{-2}. The FIB image of bare Cu reveals that the deposited Li and SEI layer has a porous and loose structure due to severe Li dendritic growth with high tortuosity and repeats breakage and regeneration of the SEI, so the overall thickness of inactive Li increases with the number of cycles, followed by lowering CE (Figure 3.5h). [40] Meanwhile, on the PCP│Cu, the deposited Li has an improved structure and reduced the total thickness (Figure 3.5i and j). Although no obvious Li dendrite with high surface area is observed, the tortuous Li morphology could still cause accumulation of inactive Li and capacity fading. [6] Impressively, the notable thickness of the Li deposit on the Ag-PCP is only 20.8 μm, which is the closest to the theoretical value (Figure 3.5k). Moreover, the compact column-like Li morphology is beneficial to completely dissolve Li ions into the electrolyte during discharging due to stable structural contact with the current collector, effectively reducing the formation of inactive Li and thus resulting in a high CE (Figure 3.5l). [36,37] Consequently, the optimized Li deposition with dendrite-free morphology on the Ag-PCP current collector indicates the effects of homogeneous Li nucleation and the LiF-rich SEI formation.

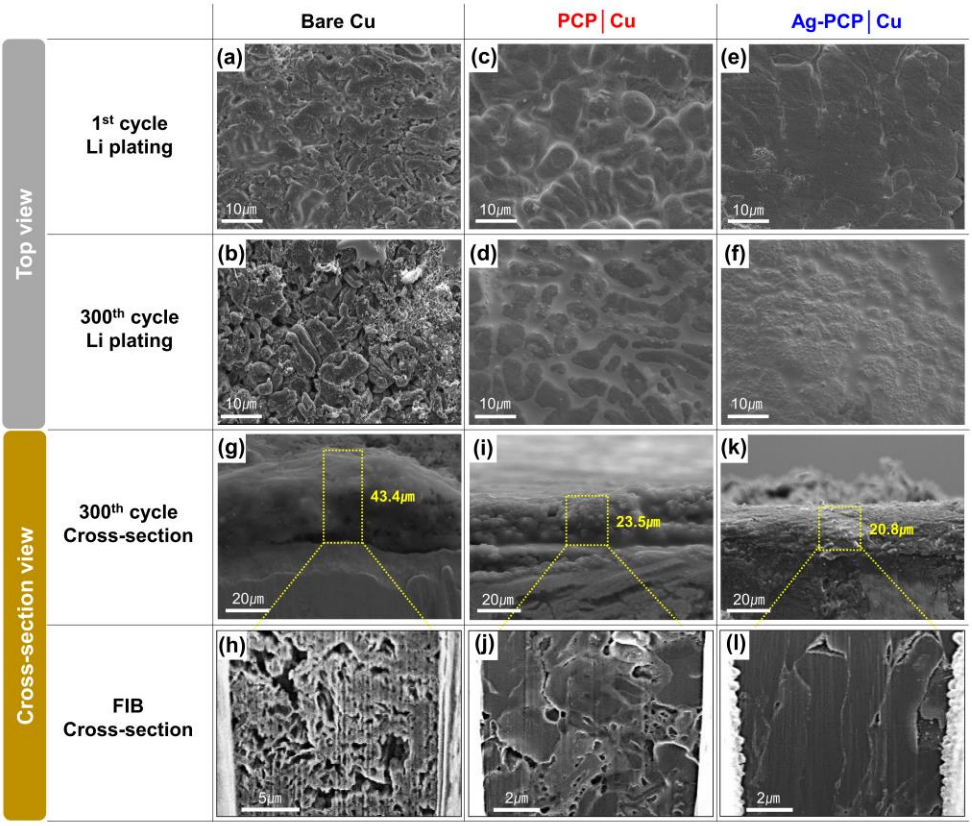

Figure 3.5 Li plating behavior on bare Cu, PCP│Cu, and Ag-PCP│Cu after Li deposition of 3 mAh cm^{-2} with a current density of 3 mA cm^{-2}. Top view SEM images at 1st and 300th cycle Li plating, Cross-sectional SEM images at 300th cycle, and FIB cross-section at 300th cycle of (a,b,g,h) bare Cu, (c,d,i,j) PCP│Cu, and (e,f,k,l) Ag-PCP│Cu.

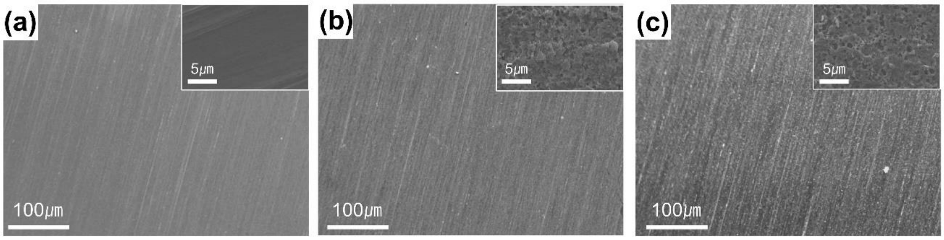

Figure 3.6 Top view SEM images of (a) bare Cu, (b) PCP│Cu, and (c) Ag-PCP│Cu with their magnified views (inset).

3.2.3 SEI Characterization of the Ag-PCP wetting agents

To elucidate in-situ interfacial fluorination mechanism for LiF-rich SEI on the Ag-PCP wetting agent, I performed in-depth X-ray photoelectron spectroscopy (XPS), cyclic voltammetry (CV), time-of-flight secondary ion mass spectrometer (TOF-SIMS), and transmission electron microscopy (TEM), as displayed in Figure 3.7. Figure 3.7a shows XPS depth profiles of SEI components covered on bare Cu, PCP│Cu, and Ag-PCP│Cu after 300 cycles, respectively. Before Ar^+ sputtering, the F 1s spectra indicates that the SEI surface is composed mainly the organic C-F bond and inorganic LiF (Figure 3.7ai). In the Ag-PCP│Cu, the SEI surface appears the lowest intensity of organic fluorine(C–F) due to the limited decomposition of $TFSI^-$, but the largest amount of LiF as a stable and conductive SEI composition, which facilitates Li^+ transfer within the SEI and allows uniform Li deposition. [41] As the sputtering time increases, no organic C–F peak, but new peaks of C–F and S–F are generated along the surface of the PCP and Ag-PCP wetting agents (Figure 3.7aii and aiii). Importantly, the covalent C–F bond on the SEI surface is different from the semi-ionic C–F bond at the bottom of the SEI, corresponding to 688.1eV and at 687.0eV on the XPS profile, respectively. [42] In general, fluorine has the highest electronegativity among all the elements (3.98); therefore, the semi-ionic C–F and S–

F bonds have chemical reactivity with plating Li due to the high negative charge on the fluorine atoms, which act as intermediate reaction sites for the LiF formation. [15,16,43] In other words, the newly formed semi-ionic C–F and S–F along the polymer chains are involved in the interfacial fluorinated reaction between the conjugated structure of the PCP chains and the temporarily existing F anions derived from the highly concentrated electrolyte, which followed by the reaction of the F-doped PCP wetting agent with Li ions, finally generating the LiF-rich SEI; the detailed F-doping mechanism is discussed in section 3.2.4. Notably, the semi-ionic C–F and S–F bonds present higher peak intensities in the Ag-PCP│Cu than in the PCP│Cu due to promoting interfacial fluorination by the Ag NPs, thus contributing to the increase in the LiF ratio. For the C 1s spectra of Figure 3.8, this is consistent with the aforementioned result that the formed SEI along the Ag-PCP chains shows the highest ratio of the semi-ionic C-F at 288.7eV, which is observed only in current collectors coated with wetting agent such as the PCP system. [41] This is because the ordered polymer chains and the increase in the degree of π–π stacking in the Ag-PCP chains provide a larger amount of F-doping sites than the PCP wetting agent due to the presence of more continuous conductive channels, as well as facilitate F anions access to the polymer chains due to electrostatic screening between the Ag-PCP chains and ClO_4^- counter ions. [14,18] Therefore, the presence of Ag NPs in the PCP wetting agent synergistically enhances the F-doping effect along the polymer chains. As shown in the Li 1s of Figure 3.9, the main contents of the outer SEI layer are organic components such as RCOLi and $ROCO_2Li$ which derived from the decomposition of electrolyte solvents, while the inner SEI layer consists of electrochemically stable inorganic species, such as Li_2O, Li_3N, Li_2CO_3, and LiF, which are originated from the $TFSI^{-}$ reduction. [44,45] Similarly, the Ag-PCP wetting agent displays the highest peak intensity of the inorganic species and the lowest peak intensity of the organic species compared to those of other current collectors, suggesting that it achieves favorable Li deposition and suppresses the undesirable side reaction between active Li and the electrolyte during cycling due to the formation of LiF-rich SEI. [19] Additionally, the XPS depth profiles of several element concentrations (Li, C, O, F, S, and N) reveal the properties and thickness of the SEI layer (Figure 3.10). For both the wetting agents, the Li and F concentration increase with increase in the Ar^{+} sputtering time, which means that LiF is a dominant constituent of the inner SEI layer. Particularly, for the Ag-PCP wetting agent, the total element concentration saturates in a shorter sputtering time and fluorine maintains a higher concentration for 16 minutes than that of the PCP wetting agent, indicating the formation of a thin and LiF-rich SEI layer on the Ag-PCP system that can prevent the continuous consumption of active Li and dendritic growth. [44]

To quantify the extent of SF^- and LiF^- as an indicator of stable SEI formation, I collected 3D chemical composition images of TOF-SIMS through separators directly attached to bare Cu, PCP│Cu, and Ag-PCP│Cu, respectively (Figure 3.7b). For bare Cu, SF^- do not appear due to the absence of intermediate components for interfacial fluorination, which results in the lowest intensity of LiF^-. By contrast, the separator in direct contact with the Ag-PCP wetting agent presents the highest ratio of SF^- from the upper region, and a remarkably high intensity of LiF^- in the region where SF^- is formed. In the depth profiles of TOF-SIMS, the ratio of LiF also shows the same result (Figure 3.11). These results indicate that the interfacial fluorination reaction of conjugated structure promotes a stable SEI formation with high ratio of LiF, as evidenced by the existence of SF^- on the PCP and Ag-PCP wetting agents. In particular, due to the new electrostatic interaction between Ag NPs and ClO_4^- counter ions, the Ag-PCP system with long-range conductive channels where π-electrons delocalize over the entire polymer chains allows more F-doping sites than the PCP system and facilitates F anions access to the Ag-PCP chains. [20,21]

In order to illustrate the fluorination process on the PCP and Ag-PCP wetting agent at the initial stage, CV scans are conducted on bare Cu, the PCP│Cu, the Ag-PCP│Cu in the potential range of $-0.05\sim1.8$ V (vs Li^+/Li) at a scan rate of 0.2 mV s^{-1} (Figure 3.7c and Figure 3.12). In the first cycle, the PCP and Ag-PCP exhibit two cathodic peaks around 0.7 V and 1.1 V, but there is no anodic peak. In the subsequent cycle, cathodic peak at 0.7 V decreases significantly, while the other cathodic peak at 1.1 V disappears. For the bare Cu, only a small cathodic peak around 0.7 V appears in the first cycle and second cycle. Therefore, the lower peak at 0.7 V corresponds to the decomposition of concentrated ether-based electrolytes. [46,47] The upper peak at 1.1 V corresponds to the interfacial fluorinated reaction between PCP chains and F anions derived from the reduction of $TFSI^{-}$, as soon as lithium is deposited on the F-doped PCP or Ag-PCP, which consequently promotes the formation of LiF-rich SEI. As a result of the fluorination process, the rapid stabilization of the SEI at the early stage minimizes the consumption of active Li for the SEI formation, leading to a long lifespan of AFLMBs. Furthermore, the formed LiF-rich SEI inhibits the repeated decomposition of electrolyte solvents during cycling due to the low electronic conductivity nature of the SEI. Notably, the cathodic peak at 1.1V for the Ag-PCP wetting agent is broader and larger than that of the PCP wetting agent, indicating the formation of ion-conductive SEI during the first cycle, which improves the diffusion ability of Li ions. [48]

I further analyzed the fluorinated SEI chemistry on the cycled Ag-PCP wetting agent using TEM, and focused on energy dispersive X-ray spectroscopy (EDS) mapping of carbon (C), oxygen (O), fluorine (F), sulfur(S), and silver (Ag) within the Ag-PCP and

SEI. In Figure 3.7d, the Ag-PCP wetting agent has lattice fringes with a d-spacing of 0.352 nm for PCP (020) and 0.235nm for Ag (111), however, the relaxed lattice spacing is also observed due to the F-doped polymer chains. [22,49] In addition, through the EDS line data, I observe fluorine distribution from the distinct lattice spacing to the relaxed lattice spacing (Figure 3.7e). It is notable that fluorine concentration significantly increases only at the lattice relaxation spacing, while the concentrations of other elements (C, O, S, and Ag) are similar or decreased at the lattice boundary. Considering the fact that the d-spacing of PCP (020) is 0.352nm, and the ionic diameter of F anion is 0.12nm, the high concentration of fluorine is originated from the interfacial reaction between the Ag-PCP chains and F anions. [15,16] Based on our observation, the interfacial fluorination promotes the formation of LiF-rich SEI at early stages, especially in the Ag-PCP system, resulting in high Li utilization efficiency to prolong the lifespan of AFLMBs.

Density functional theory (DFT) calculations are also used to illustrate the effectiveness of the Ag-PCP wetting agent for interfacial fluorination during cycling (Figure 3.7f and g). Compared with the interaction between F anions and pristine PCP or Ag-PCP chains, the increased binding energies of F anions with atoms in the Ag-PCP chains (C–F boding; from 2.691 to 3.391 and S–F boding; from 0.781 to 1.641) indicate that the presence of Ag NPs on the PCP chains could promote more interfacial fluorination than the pristine PCP chains, which is directly involved in a high ratio of LiF in the SEI.

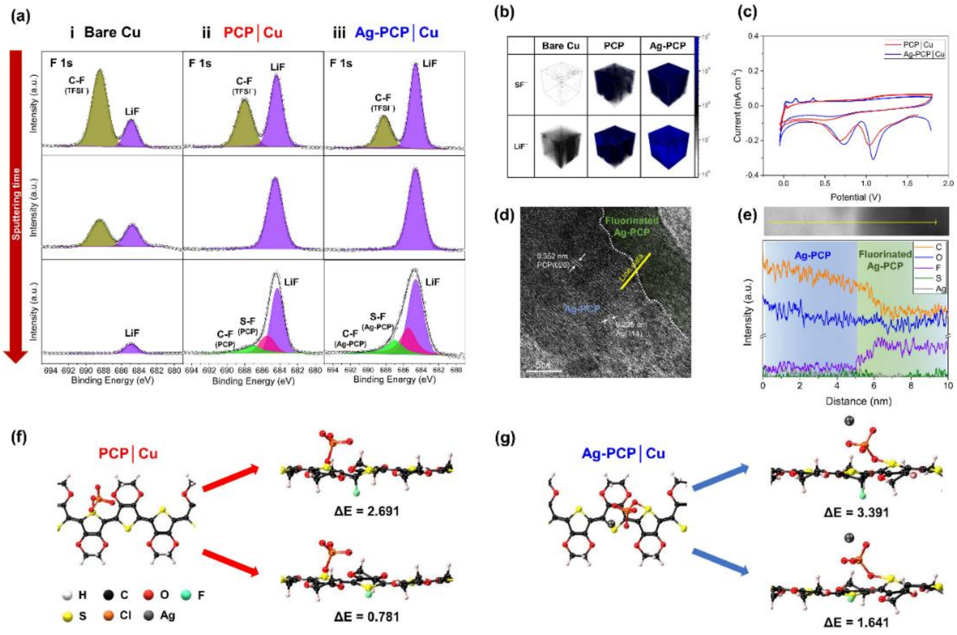

Figure 3.7 Interfacial chemistry of bare Cu, pristine PCP│Cu, and Ag-PCP│Cu after cycling. (a) F 1s XPS depth profiles of SEI formed on the cycled (i) bare Cu, (ii) pristine PCP│Cu, and (iii) Ag-PCP│Cu after 300 cycles at a current density of 3 mA cm^{-2} (3 mAh cm^{-2}). (b) 3D chemical composition images from TOF-SIMS depth profiles of SEI formed on the cycled separators directly attached to bare Cu, pristine PCP│Cu, and Ag-PCP│Cu, respectively. (c) CV curves in the potential region of –0.05~1.8 V (vs Li$^+$/Li) at a scan rate of 0.2 mV s^{-1}. (d) TEM image of the cycled Ag-PCP wetting agent and (e) EDS line data of yellow line in d image. The binding energies of F anion with (f) PCP wetting agent; C–F binding energy (up), S–F binding

energy (down) or (g) Ag-PCP wetting agent; C–F binding energy (up), S–F binding energy (down) extracted from the DFT calculations.

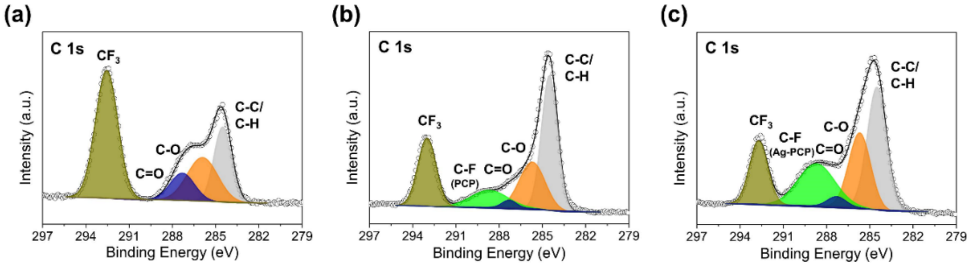

Figure 3.8 C 1s XPS profiles of SEI formed on the cycled separators directly attached to (a) bare Cu, (b) PCP/Cu, and (c) Ag-PCP/Cu, respectively, after 300 cycles at a current density of 3 mA cm^{-2} (3 mAh cm^{-2}).

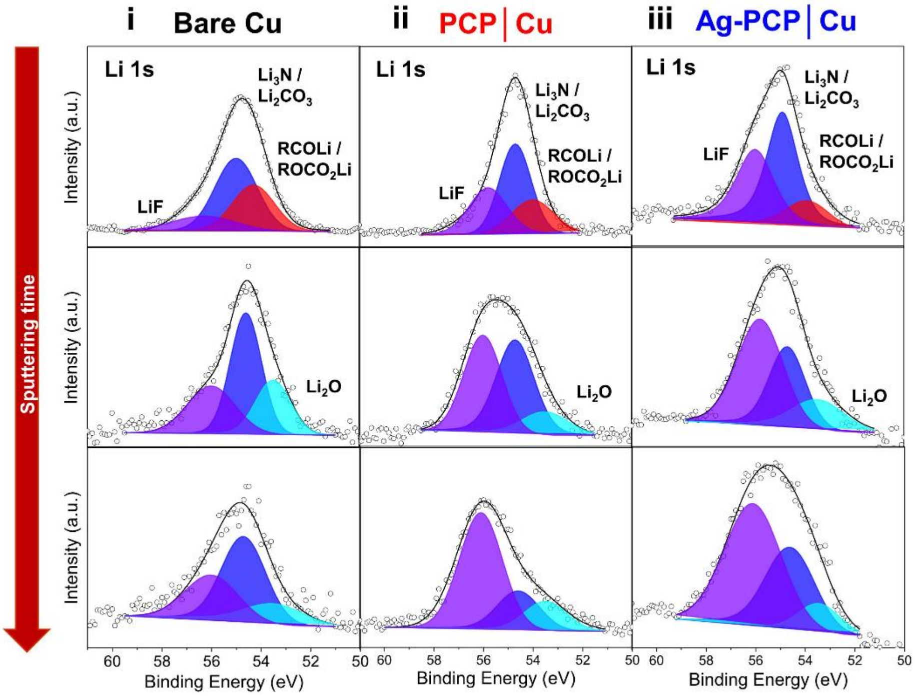

Figure 3.9 Li 1s XPS depth profiles of SEI formed on the cycled (a) bare Cu, (b) pristine PCP│Cu, and (c) Ag-PCP│Cu after 300 cycles at a current density of 3 mA cm^{-2} (3 mAh cm^{-2}).

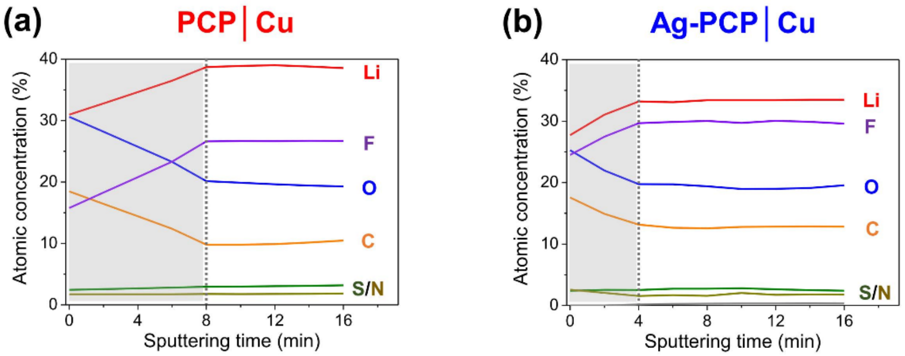

Figure 3.10 Several element concentrations (Li, C, O, F, S, and N) from XPS depth profiles of SEI formed on the cycled (a) PCP│Cu and (b) Ag-PCP│Cu after 300 cycles at a current density of 3 mA cm^{-2} (3 mAh cm^{-2}).

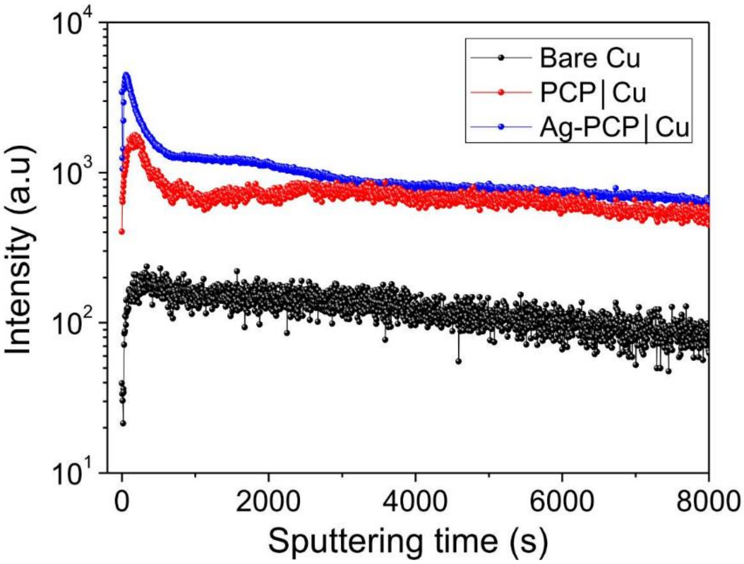

Figure 3.11 The comparison of LiF¯ ratio, a component of stable SEI, from TOF-SIMS depth profiles of SEI formed on the cycled separators directly attached to bare Cu, PCP│Cu, and Ag-PCP│Cu, respectively.

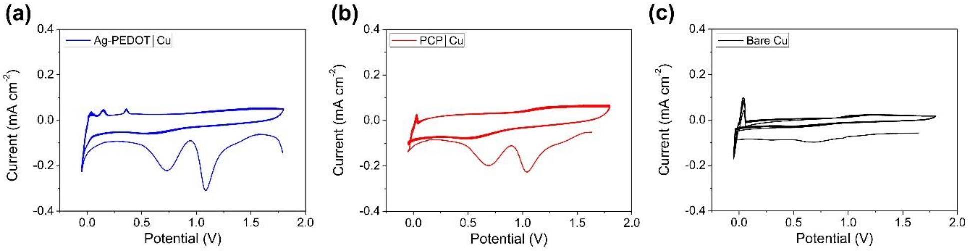

Figure 3.12 Cyclic voltammetry (CV) curves of (a) Ag-PCP | Cu, (b) PCP | Cu, and (c) Ag | Cu as working electrodes with Li metal as reference and counter electrodes in the potential region of –0.05~1.8 V (vs Li^+/Li) at a scan rate of 0.2 mV s^{-1}.

3.2.4 Mechanism of interfacial fluorination

I propose a strategy of wetting agent on the current collector without requiring any extra additives or post-treatment to regulate the initial Li deposition and construct LiF-rich SEI for long lifespan of AFLMBs. Starting from the salt-concentrated electrolyte (typically > 3.0 M, M being molarity (mol L^{-1})), the reduction pathways of electrolyte are significantly modified by the improved reductive stability. [50,51] For the concentrated electrolytes, solvent molecules and salt anions are strongly coordinated to Li ions by strong coulombic interactions, so the solvent molecules are effectively stabilized due to an absence of free solvent molecules. Therefore, the factor participating in the SEI formation changes from solvent decomposition to salt anion decomposition which has the lower lowest unoccupied molecular orbital (LUMO) energy level. When current is applied, the TFSI anions are preferentially reduced on the surface of the PCP wetting agent in contact with Cu foil. Although the primary reduction products of TFSI anions mainly comprise relatively large fragments, these large fragments immediately start to the defluorination, leading to the formation of F anions. Next, the formed F anions combine with the π-conjugated sites in the Ag-PCP wetting agent, generating the semi-ionic C–F bond and S–F bonds. [16] Notably, the semi-ionic C–F bond and S–F bonds have high polarities due to the highest electronegativity of fluorine (3.98), and thus the F-doped PCP wetting agent has chemically reactivity, which acts as intermediate reaction sites for the formation of stable SEI. [43] As soon as Li ions are deposited and react with the F-doped sites of PCP wetting agent. Consequently, the formation of LiF-rich SEI is promoted by the F-doped PCP wetting agent.

Especially, the presence of Ag NPs on the PCP chains further enhances the interfacial fluorination chemistry in the following ways: (1) Ag NPs provide long-range conductive channels over the entire PCP chains due to the structural rearrangement and the reduction of π–π stacking distance. [18] This is because the positively charged Ag NPs attract the negatively charged ClO_4^- counter ions, so the interactions between the PCP chains are considerably intensified. The elongated Ag-PCP chains with higher packing density have the delocalized π-electrons throughout the Ag-PCP wetting agent, leading to an increase in the F-doping sites. [21] (2) The positively charged Ag NPs on the PCP wetting agent reduce the repulsive force of the negatively charged ClO_4^- counter ions against the F anions. Since the presence of Ag NPs generates the electrostatic interaction between Ag NPs and ClO_4^- counter ions, it induces electrostatic screening between the PCP chains and ClO_4^- counter ions. [20] In the Ag-PCP wetting agent, the decreased effect of ClO_4^- counter ions facilitates F anions access to the polymer chains. For these reasons, the Ag-PCP wetting agent promote the formation of LiF-rich SEI at the early stage, which improves Li ion diffusion and suppresses Li dendrite growth.[19] Overall, I report that the synergistic effect of Ag NPs and PCP optimizes Li deposition behavior and promotes favorable SEI chemistry, with the aim of expanding the applicability to interfacial stabilization for high-energy-density rechargeable batteries.

Based on the above observations and discussion, Figure 3.13 illustrates the Li plating behavior and SEI evolution on bare Cu, PCP│Cu, and Ag-PCP│Cu during cycling, respectively. When employing bare Cu as the current collector, the Li nucleation is isolated and randomly distributed due to the poor lithiophilicity and heterogeneous surface of Cu foil. [10,52] Li morphology with high tortuosity induces inhomogeneous Li ion flux and leaves a large amount of inactive Li, resulting from structural disconnection to the current collector. [6] Thus, on bare Cu, unfavorable Li plating with increasing cycles accelerates dendritic Li growth and the accumulation of unreacted by-product (Figure 3.13a). By contrast, the PCP wetting agent provides 3D conductive framework as well as F-doping sites that act as the intermediates for LiF formation, thus improving both the nucleation behavior of Li ion and its growth process. [15,16] Furthermore, the curved Li morphology with its low tortuosity facilitates Li ion diffusion and reduces the presence of inactive Li, resulting in little Li dendritic growth and a thinner SEI layer (Figure 3.13b). Prominently, when employing the Ag-PCP wetting agent as the Li plating matrix, the combined effect of Ag and PCP chains significantly promotes uniform Li nucleation and deposition due to the Ag-Li alloying process and the enlarged F-doping sites throughout the Ag-PCP chains. Therefore, this ideal Li deposition with its compact column-like structure and minimum tortuosity ensures homogeneous Li ion flux and achieves high Li utilization efficiency. [6,53] When cycles were complete, the surface of the Ag-PCP│Cu is covered by smooth Li deposition with dendritic-free structure and dense LiF-rich SEI (Figure 3.13c).

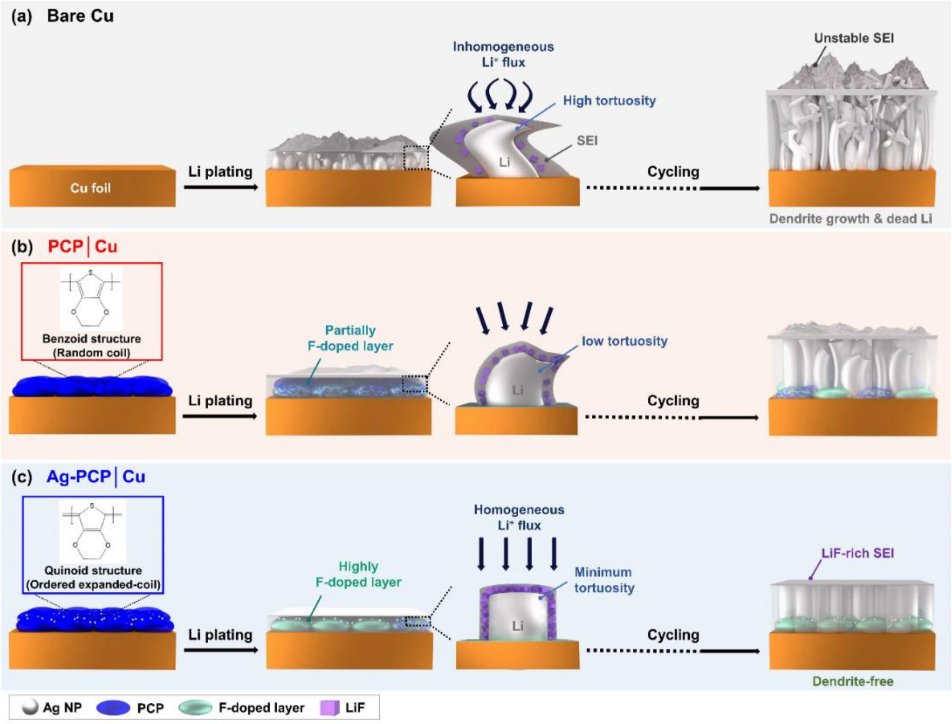

Figure 3.13 Schematic of Li plating behavior and the SEI formation mechanism (a) Bare Cu, (b) PCP│Cu, and (c) Ag-PCP│Cu.

3.2.5 Electrochemical performances of asymmetric cells

To verify the Ag-PCP wetting agent as Li nucleation guidance, I evaluated the nucleation overpotential before galvanostatic cycling tests in asymmetric cells (Figure 3.14a). Note that the nucleation potential defines the difference between the lowest voltage dip and the later voltage plateau, appearing only the initial Li deposition on the heterogeneous substrate. Also, the nucleation potential is a critical parameter that influences the subsequent deposition behavior of Li ions. [54–56] In bare Cu, the nucleation potential exhibits 143 mV with a sharp voltage dip, while the PCP│Cu shows a nucleation potential of 25 mV with a smoother voltage dip. Particularly, the Ag-PCP│Cu exhibits no voltage dip due to the formation of Ag-Li alloy as well as the ordered Ag-PCP chains with densely packing of the conjugated structure. Furthermore, I proved again the interfacial fluorination of the PCP and Ag-PCP wetting agents. The upper voltage plateau around 1.1 V indicates the formation potential of LiF-rich SEI, and the lower voltage plateau around 0.7 V indicates the reduction potential of electrolyte solvents, which is in agreement with the aforementioned CV results. In Figure 3.15, I observed the nucleation overpotentials at different current densities ranging from 0.1 to 3 mA cm^{-2}. The nucleation overpotential of the Ag-PCP│Cu increases to 0.059 V with the increase in current density, while that of the bare Cu drastically increases from 0.143 to 0.344 V. These results suggest that the Ag-PCP wetting agent optimizes the Li nucleation even at high current densities.

To evaluate the effectiveness of Ag-PCP wetting agent for the interfacial stability and the reversibility of Li ions, I carried out the electrochemical performance in asymmetric cells (Li//bare Cu, Li//PCP│Cu, and Li//Ag-PCP│Cu). Figure 3.16 shows the voltage-time profiles at current density of 0.5 mA cm^{-2} for 1 mAh cm^{-2} of Li deposition and then Li stripping to 0.3 V. After 1000 hours, the Ag-PCP│Cu shows no short circuit and better voltage profile with the lowest overpotential than the PCP│Cu. By contrast, bare Cu exhibits an increase in voltage hysteresis and a sudden voltage drop within only 80 hours, indicating the accumulation of inactive Li and thick SEI due to continuous breakage and formation of SEI. [40] Also, I conducted the modified test method, Aurbach CE test, to accurately calculate the average CE of Li deposition/dissolution except for the low initial CE (ICE), as shown in Figure 3.17. [57] After a single cycle of Li deposition with a high capacity (5 mAh cm^{-2}) and Li dissolution to 0.3 V, I deposit Li onto the bare Cu, PCP│Cu, and Ag-PCP│Cu as the Li reservoir (Q_T=5 mAh cm^{-2}) at 0.5 mA cm^{-2}, respectively. The cells cycled (Q_C=1 mAh cm^{-2}) for 10 cycles, and then stripped to 0.3 V (Q_S) at fixed current density of 0.5 mA cm^{-2}. The average CE, excluding the initial stabilizing cycle, is calculated by

Equation.1. $\mathrm{CE}_{avg} = \frac{nQ_C+Q_S}{nQ_C+Q_T}$ (1) Using the equation, the Ag-PCP | Cu reveals a stable cycling performance with the highest CE of 99.95% when compared with PCP | Cu (99.91%) or bare Cu (89.66%).

Based on the greatly improved interfacial stability of the Ag-PCP, I applied a modified test protocol to investigate the practical application of Ag-PCP wetting agent in AFLMBs (Figure 3.14b). [58] I preplated excess Li metal with a capacity of 3 mAh cm^{-2} onto the bare Cu, PCP | Cu, and Ag-PCP | Cu for 5cycles, respectively, and then cycled with a capacity of 1 mAh cm^{-2} (1 mA cm^{-2}). The amount of preplated Li is determined by the basis of the areal capacity in commercial batteries. When the preplated Li is depleted in Li reservoir, the voltage curve of Li stripping appears sharp tip. Notably, the Ag-PCP | Cu cell achieves an excellent cycle stability over 1000hours, while the PCP | Cu cell completely exhausts the excess Li within 607 hours and bare Cu do not operate at all. Moreover, to verify the combined effect of Ag NPs and PCP chains even under harsh conditions, I evaluated the electrochemical behavior at high current density of 3 mA cm^{-2} and high capacity of 3 mAh cm^{-2} where it accelerates the SEI formation and Li dendrite growth (Figure 3.18a). The Ag-PCP applied cell shows the highest ICE of 95.36%, benefiting from the Ag–Li alloying reaction and the formation of LiF-rich SEI at the beginning of Li plating. The Ag-Li alloying/de-alloying process could observe a voltage plateau in the profiles of Li deposition/dissolution under 0.5 V, leading to the high reversibility of Li ions. [44] Also, the Ag–Li alloying process is confirmed by the XRD peaks of the Ag–Li alloy (2θ at 30.58°, 36.25°, 41.40°, 52.58°, and 76.63°) and the sharp cathodic peak under 0.2 V in the CV curves (Figure 3.18b and c). [22,49] Then, the anodic peaks at 0.15 V and 0.34 V are attribute to Li oxidation from the Ag-Li alloy. [54] Due to the outstanding initial electrochemical behavior of the Ag-PCP│Cu cell, I also obtained similar results of galvanostatic cycling test with the increasing number of cycles. In the Ag-PCP│Cu cell, the voltage profiles show quite low voltage polarization (≈17 mV) and excellent capacity retention over 300 cycles even under harsh conditions (3 mA cm^{-2}, 3 mAh cm^{-2}) due to the initial interfacial stabilization, compared to the PCP│Cu cell with its relatively large polarization (≈42 mV) and the increase in capacity loss (Figure 3.14c and d). Since the voltage polarization is attributed to the charge transfer kinetic of interfacial feature, the Ag-PCP│Cu cell with the lowest polarization delivers fast charge transfer, which inhibits the undesirable interfacial reaction. [52] Otherwise, the bare Cu exhibits a severe increase in voltage hysteresis and rapid capacity fading, resulting from the accumulated side products and unstable SEI (Figure 3.14e). Also, in the rate performance, the Ag-PCP│Cu cell exhibits a highly stable voltage profile with the lowest voltage hysteresis and without obvious polarization even at high current density of 5 mA cm^{-2} (Figure 3.19).

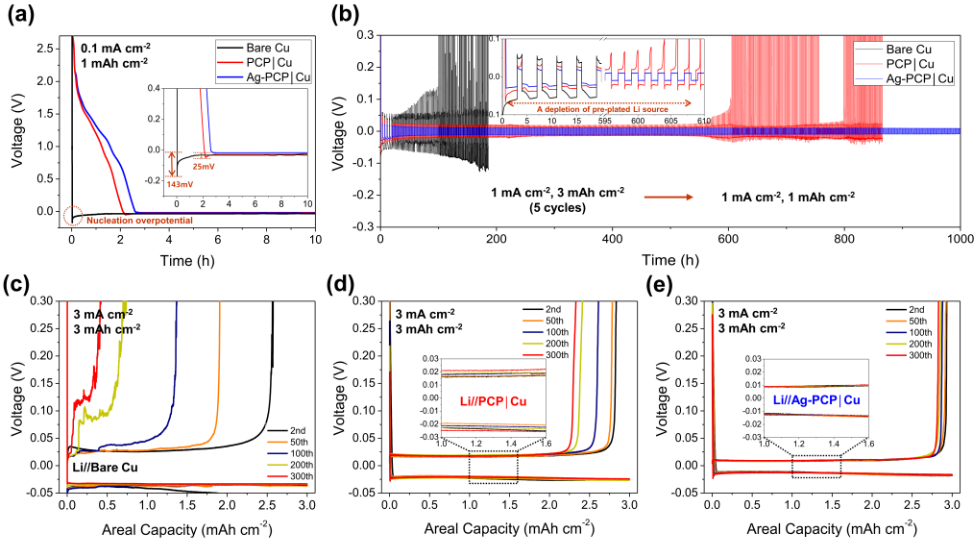

Figure 3.14 Electrochemical performances of asymmetric cells (Li//bare Cu, Li//PCP│Cu, and Li//Ag-PCP│Cu). (a) Evaluation of Li nucleation overpotential; voltage profile of Li plating at a current density of 0.1 mA cm^{-2} (1 mAh cm^{-2}). (b) Evaluation of interfacial stability and Li plating/stripping reversibility; Voltage profile of the practical applicability test. During the initial five cycles, excess Li metal with a capacity of 3 mAh cm^{-2} was plated onto the bare Cu, PCP│Cu, and Ag-PCP│Cu, respectively. In subsequent cycles, all cells were cycled at a current density of 1 mA cm^{-2} with a capacity of 1 mAh cm^{-2}. (c-e) Voltage profiles of Li plating/stripping at a current density of 3 mA cm^{-2} (3 mAh cm^{-2}).

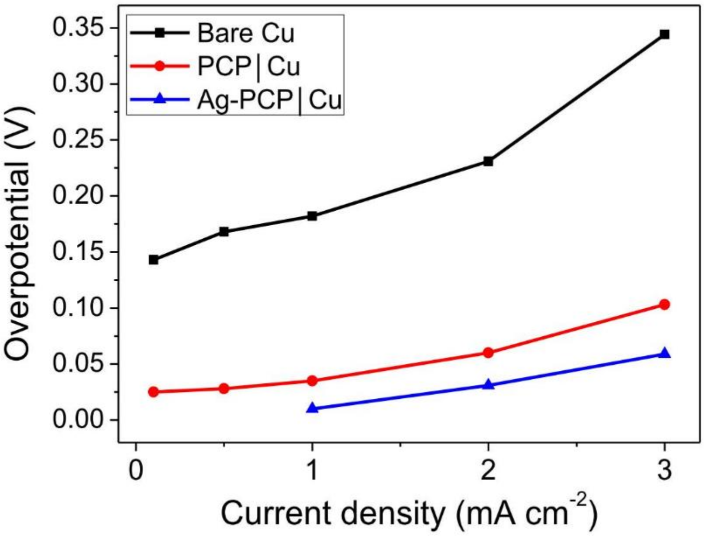

Figure 3.15 Li nucleation overpotential of asymmetric cells (Li//bare Cu, Li//PCP│Cu, and Li//Ag-PCP│Cu) at different current densities ranging from 0.1 to 3 mA cm^{-2}.

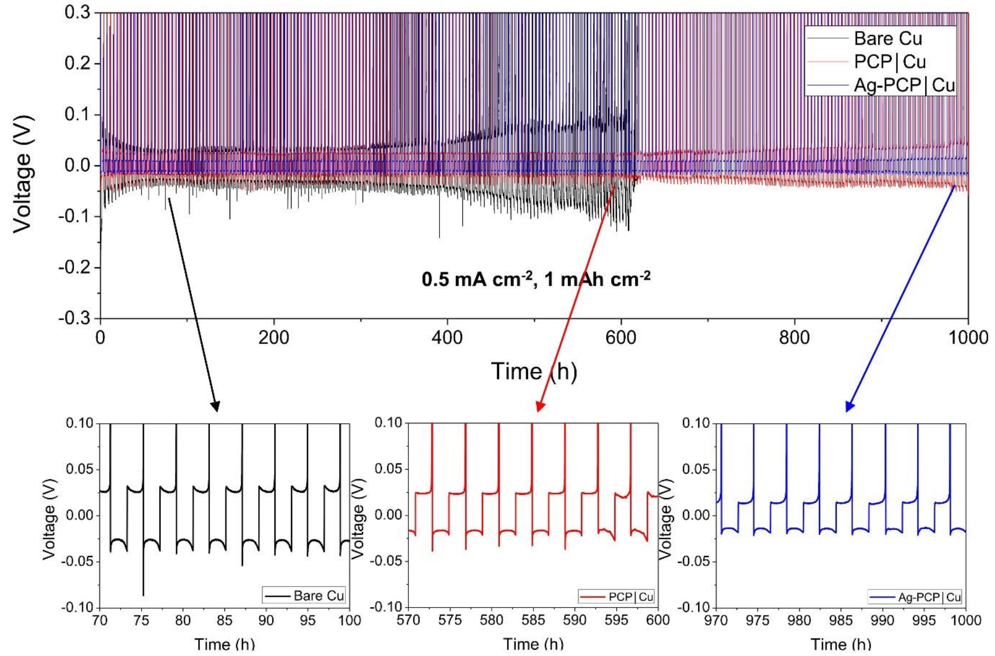

Figure 3.16 Voltage-time profiles at current density of 0.5 mA cm^{-2} for 1 mAh cm^{-2} Li deposition and then Li stripping to 0.3 V. The magnified images show voltage polarization of the bare Cu, PCP│Cu, and Ag-PCP│Cu, respectively.

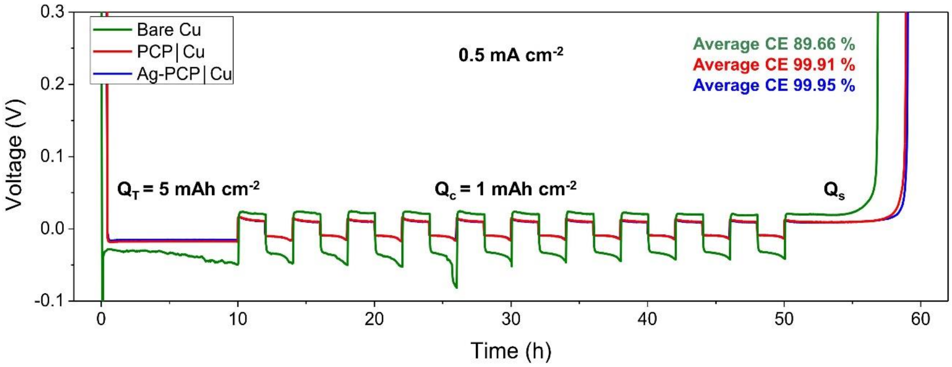

Figure 3.17 Aurbach CE test

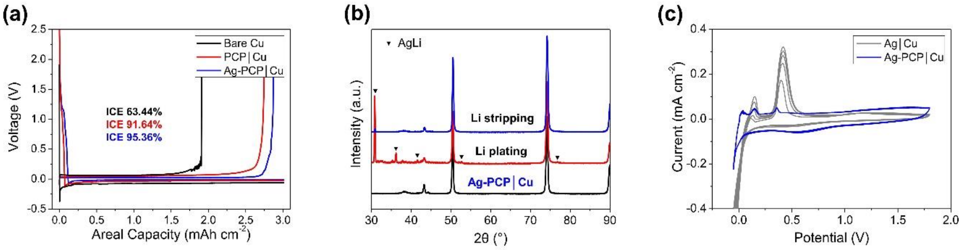

Figure 3.18 (a) Voltage profiles of Li plating/stripping at a current density of 3 mA cm^{-2} (3 mAh cm^{-2}) in the 1st cycle. (b) XRD patterns of the Ag-PCP│Cu showing the Ag-Li alloying/dealloying. (c) CV curve of Ag-PCP│Cu and Ag│Cu as working electrodes with Li metal as reference and counter electrodes in the potential region of - 0.05 ~ 1.8 V (vs Li$^+$/Li) at a scan rate of 0.2 mV s^{-1}.

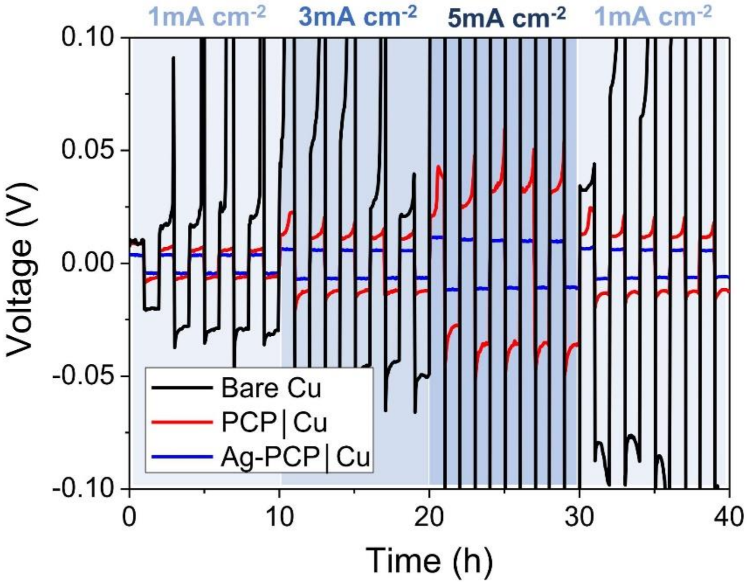

Figure 3.19 The rate performance of asymmetric cells (Li//bare Cu, Li//PCP│Cu, and Li//Ag-PCP│Cu). The areal capacity is determined by the time (1 hour) with increasing current density from 1 to 5 mA cm^{-2}, each cycling 5 times.

3.2.6 Electrochemical performances of anode-free full cells

I further investigated the practical utilization of the Ag-PCP wetting agent in an anode-free full cell using an LFP cathode. Since the anode-free full cell has only a limited amount of active Li, I can identify significant differences in the cycling performances according to the interfacial properties of the current collector where the Li ions is deposited. To verify the improved interfacial properties of the LFP//Ag-PCP│Cu cell at the early stage, electrochemical impedance spectroscopy (EIS) is conducted, which is also a crucial factor for ensuring outstanding cycling performances (Figure 3.20). [59] The Ag-PCP│Cu full cell shows the stabilized interfacial impedances with the greatly low charge transfer resistance after 10 cycles compared to the bare Cu and PCP│Cu full cells, indicating that a LiF-rich SEI with high ionic conductivity had successfully formed. In Figure 3.21a, benefiting from the synergistic effect of the Ag-Li alloying process and F-doping chemistry on the Ag-PCP chains, the Ag-PCP based full cell exhibits higher specific capacity of 129.9 mAh g^{-1} and initial coulombic efficiency (ICE) of 85.94% at 1 C-rate than the LFP//PCP│Cu (specific capacity of 118.9 mAh g^{-1}, ICE of 82.70%). However, the LFP//bare Cu cell delivers the lowest specific capacity of 65.0 mAh g^{-1} and ICE of 58.85%, which indicates a severe consumption of Li sources due to the initial side reactions for the SEI formation. In the subsequent cycles, rapid capacity fading occurs, finally followed by depletion of the Li reservoir (Figure 3.22). Meanwhile, the LFP//Ag-PCP│Cu cell shows the enhanced cycling performances with capacity retention of 72% throughout 200 cycles, especially remarkable within 80 cycles, where the LFP//PCP│Cu cell exhibits oscillating CE and more severe capacity fading, finally capacity retention of 53% (Figure 3.21b). A notable point is that the capacity retention of anode-free full cells can predict the Li inventory retention rate (LIRR), which indicates the "average" loss in Li inventory per cycle and is analogous to coulombic efficiency (CE) value. [19] A new parameter, LIRR, is calculated by the capacity retention (Q_n / $Q_{initial}$) at cycle number (n), given by Equation.2. LIRR = $100 * \left(\frac{Q_n}{Q_{initial}}\right)^{\frac{1}{n}}$ (2) Based on the equation, the LFP//Ag-PCP│Cu cell exhibits a higher LIRR of 99.8% than the LFP//PCP│Cu cell with LIRR of 99.6% after 200cycles, resulting from a high Li utilization efficiency as Li reservoir. Moreover, Figure 3.21c-e displays the voltage profiles of LFP//bare Cu, LFP//PCP│Cu, and LFP//Ag-PCP│Cu with different cycles, respectively. The LFP//Ag-PCP│Cu cell presents almost invariable voltage hysteresis and polarization, which is attributed to the improved kinetic properties and Li ion transfer due to the LiF-rich SEI, however, the LFP//PCP│Cu cell shows an increased voltage hysteresis and polarization, indicating an accumulation of side products, especially in the LFP//bare Cu cell. [59]

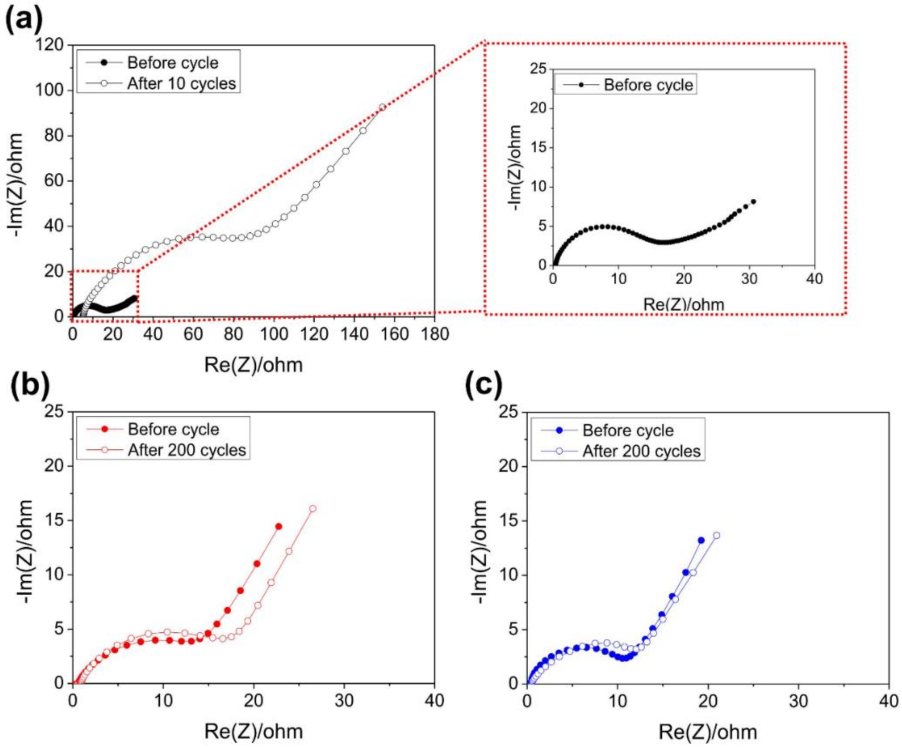

Figure 3.20 Nyquist plots of (a) LFP//bare Cu, (b) LFP//PCP│Cu, and (c) LFP//Ag-PCP│Cu full cells before and after 10 cycles at 1 C-rate.

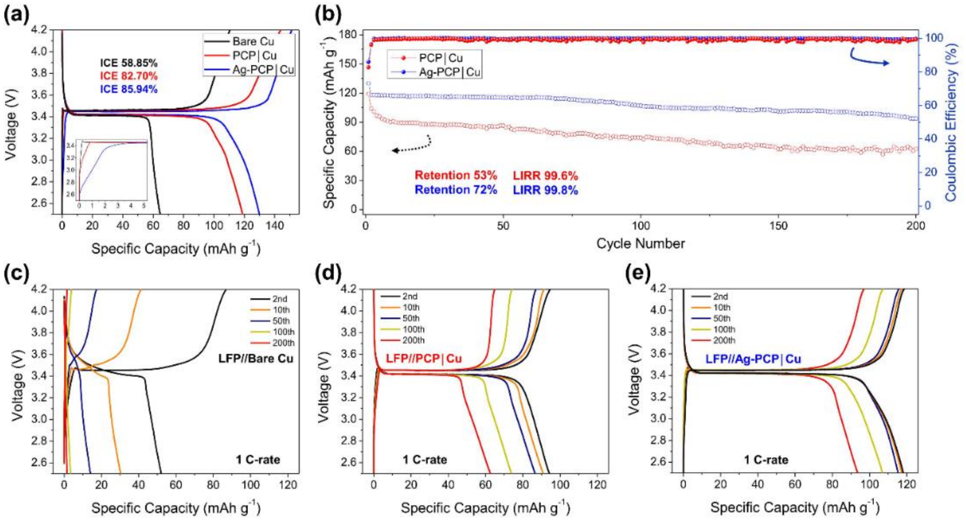

Figure 3.21 Electrochemical performances of LFP full cells (LFP//bare Cu, LFP//PCP│Cu, and LFP//Ag-PCP│Cu) at 1 C-rate. (a) Voltage profiles of Li plating/stripping at the 1st cycle. (b) Cycling performance of LFP//PCP│Cu (red) and LFP//Ag-PCP│Cu (blue) full cells. Voltage profiles of Li plating/stripping at the 2nd, 10th, 50th, 100th, and 200th cycles; (c) LFP//bare Cu, (d) LFP//PCP│Cu, and (e) LFP//Ag-PCP│Cu.

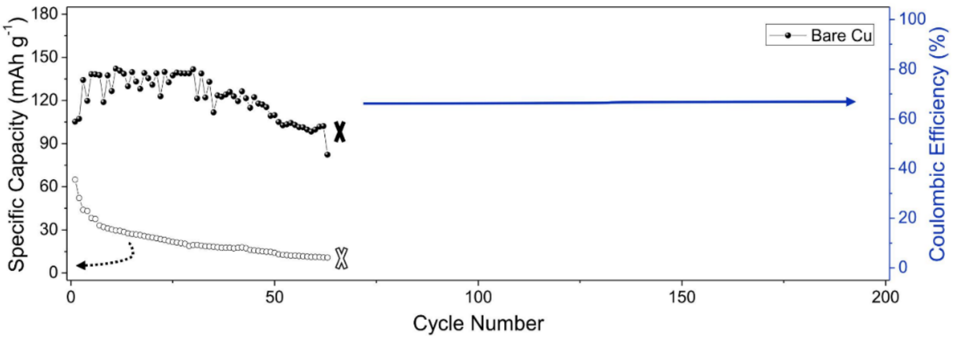

Figure 3.22 Cycling performance of LFP//bare Cu full cell.

3.3 Conclusion

In conclusion, I propose an Ag-PCP wetting agent on the current collector to prolong the lifespan of AFLMBs with ultrahigh Li utilization efficiency by enabling both uniform Li nucleation and the rapid formation of LiF-rich SEI at the early stage. In addition, I uncover an interfacial fluorinated mechanism induced by the Ag-PCP to efficiently regulate the SEI chemistry related to LiF formation, arising from the consecutive reactions between π-conjugated regions in the Ag-PCP chains and F anions derived from $TFSI^{-}$ reduction, as soon as between the F-doped Ag-PCP and the plating Li ions. The Ag NPs act not only as Li nucleation seeds but also as polymer chain modifiers, and the ordered Ag-PCP chains with closely π-conjugated structure provide F-doping sites, resulting in an increase in the LiF ratio in the SEI. The stable SEI with a high ratio of LiF facilitates kinetically favorable Li-ion diffusion, which significantly inhibits the Li dendritic growth and depletion of the Li reservoir. Benefiting from the synergistic effect of Li deposition control and a favorable SEI chemistry, I achieve dendrite-free structure and superior cycling stability even under a harsh environment, with the LFP/Ag-PCP | Cu full cell achieving a high capacity retention of 72% (LIRR 99.8%) at 1C-rate after 200 cycles. Moreover, the fabrication of the Ag-PCP wetting agent is quite simple *via* the electrostatic interaction between oppositely charged Ag cations and ClO_4^- dopants. All these above advantages suggest that our study provides a promising strategy for interfacial stabilization to develop high-energy-density rechargeable batteries.

3.4 Experimental details

Preparation of Ag-PCP wetting agent

The Cu current collector (2.5 × 5 cm) was polished with acetic acid (Sigma-Aldrich, ACS reagent, ≥99.7%) to remove copper oxide and other surface contaminants, and then dried with a nitrogen gas flow. The Ag NPs incorporated PCP wetting agent was synthesized *via* electrochemical polymerization and the electrostatic interaction between oppositely charged Ag cations and ClO_4^- dopants.[14] The PCP wetting agent on Cu foil was polymerized using the Agilent Technologies 33500B series at constant potential mode at 1.5 V vs. SCE by passing a charge of 44 mC for 300 s, and this process was repeated 5 times. In the three-electrode configuration, the acid-treated Cu foil was used as the working electrode, Ag/AgCl as the reference electrode, and a Ti plate (3 × 5.5 cm) as the counter electrode. The electrolyte contained 0.04 M 3,4-ethylenedioxythiophene (EDOT) monomer with 0.1 M lithium perchlorate ($LiClO_4$) as the supporting salt and acetonitrile (ACN) as the solvent. EDOT (Clevios M V2) was purchased from Heraeus. Anhydrous $LiClO_4$ and ACN of analytical reagent grade were obtained from Sigma-Aldrich. The resulting PCP was rinsed several times using deionized (DI) water to remove unreacted reactants and residues. Subsequently, it was immersed into 1 mM silver nitrate ($AgNO_3$, Sigma Aldrich) aqueous solution for 3 mins and then washed with DI water. Finally, I obtained the Ag-PCP/Cu *via* the electrostatic interaction of Ag:ClO_4 without the need for any additional reductants.

Preparation of LFP cathode

The precursors of the LFP cathode (loading density 17 mg cm^{-2}, areal capacity 2.21 mAh cm^{-2}) were prepared: Li hydroxide monohydrate ($LiOH \cdot H_2O$, 99%, Sigma-Aldrich), phosphoric acid (H_3PO_4, 85%, ACROS), and iron sulfate heptahydrate ($FeSO_4 \cdot 7H_2O$, 99%, Alfa Aesar) were mixed in a ratio of 2.7:1:1.5, respectively, in ethylene glycol ($C_2H_6(OH)_2$, 99%, Samchun) to form an olive-green suspension. For solvothermal synthesis, the suspension was transferred into a Teflon-lined stainless-steel autoclave, where it remained at 180 °C for 10 hours. [60] Then, the resulting gray precipitates were rinsed several times with ethyl alcohol and DI water and dried in the freeze drier. For electrochemical test in harsh conditions, the additional treatment of LFP is implemented by N-doped carbon (NC) and reduced graphene oxide (rGO). The LFP powder was reacted in tris-buffer solution (10 mM), followed by the addition of dopamine hydrochloride (3 mg mL^{-1}, 200 mL H_2O). GO suspensions (3 wt% in H_2O) were mixed with the dopamine solution for over 10 mins, thus all suspension reacted for 5 mins. After washing with DI water three times, the products were dried at 70 °C for 10 hours under vacuum and then calcined at 700 °C for 5 hours in an argon-filled glove box to form LFP@NC@rGO. To fabricate the LFP electrode, the as-prepared powder, Super P (Timcal, carbon black), and poly(vinylidenefluoride) (PVDF, Kynar HSV900) with a weight ratio of 70:15:15 in N-methyl-2-pyrrolidone (NMP, 99%, Aldrich) were mixed by ball milling for 20 mins and then the resulting slurry was applied to the aluminum foil and dried at 120 °C for 10 hours in a vacuum oven.

Characterization of the Ag-PCP wetting agent

The sheet resistance was measured by the Van der Paw method using a source meter (Keithley 2400). For the structural analysis of the Ag-PCP, XRD patterns were obtained using an X-ray diffractometer (Smartlab, Rigaku) from 0 to 90° of 2θ (diffraction angle), with Cu Kα ($\lambda = 0.154$ nm) radiation at 40 kV and 30 mA. Also, the GIWAXS measurement was performed on a laboratory beamline system (Xeuss 2.0) with an X-ray wavelength of 1.54189 Å and sample to detector distance of 118 mm, and used a hybrid pixel array detector (Pilatus 300k, DECTRIS, pixel size 172 mm). The FTIR spectra were obtained by scanning from 1700 to 600 cm^{-1} on a Bruker Alpha II with a diamond crystal ATR.

Density functional theory (DFT) calculation

All binding energy calculations was performed with DFT calculation by the first principal method *via* Vienna Ab initio Simulation Package (VASP). The calculated electron exchange-correlation energies were confirmed by the generalized gradient approximation (GGA) from Perdew-Burke-Ernzerhof (PBE) with the effect of van der Waals reactions. The PCP and Ag-PCP supercell's dimensions were 20Å × 30Å × 15.8Å, and the k-point of the supercell grid was sampled to 4 × 4 × 1 for calculating intensities only the relationship between PCP (Ag-PCP) and F anions without interference from the surroundings. It was calculated with a generous size and cleaved through a single layer of bulk materials, which included $C_{24}S_4O_8H_{16}$ atoms in PCP (Ag-PCP) chains with vacuum cells. All calculations were performed after structural stabilization through thermodynamic sufficient stability. Adsorption sites and adsorption energies between each PCP (Ag-PCP) chain and F anion were computed. The binding energy was used to evaluate the adsorption strength between S atom or C atom in PCP (Ag-PCP) chain and F anion and was computed as the difference between the energy of the absorbed system and the sum of each system, as shown in the following equation:

$$E_{total} = E_{PCP\ or\ Ag-PCP} - E_{ClO_4(with\ or\ without\ Ag^+)}$$

Where E_{total} was the total energy of PCP (Ag-PCP), ClO_4^-, Ag^+ ion and F^- ion), E_{pcp}

and E_{ClO4} were the energies of the substrate and ClO_4 anion respectively.

Electrochemical Measurement

Standard CR2032 coin cells were used for the electrochemical test of all cells and assembled in an argon-filled glove box (oxygen contents < 0.1 ppm and water contents < 0.1 ppm). Celgard 2325 separator and 3 M lithium bis(trifluoromethanesulfonyl)imide in 1,2-Dimethoxyethane/1,3 Dioxolane (3M LiTFSI in DME/DOL) (1:1, v/v) electrolyte (Panax Etec Co. Ltd. STARLYTE) were also used. In the anode-free asymmetric cells, Li foil was used as the counter electrode (a diameter of 16mm), and Cu foil, PCP│Cu, and Ag-PCP│Cu were used as anode substrate (a diameter of 16mm). In common test protocol, the charge process had a fixed areal capacity, and the discharge process had a cutoff voltage of 0.3 V. The tests were conducted at constant currents from 0.1 to 3 mA cm^{-2}, and the areal capacity was varied from 1 to 3 mAh cm^{-2}. In the practical applicability test, excess Li metal with a capacity of 3 mAh cm^{-2} was pre-plated onto the bare Cu, PCP│Cu, and Ag-PCP│Cu for 5 cycles, respectively, followed by Li plating/stripping at a current density of 1 mA cm^{-2} with a capacity of 1 mAh cm^{-2}. For the Aurbach CE test, I conducted a single cycle of Li deposition with a high capacity (5 mAh cm^{-2}) and Li dissolution to 0.3 V, and Li (5 mAh cm^{-2}) was deposited on the bare Cu, PCP│Cu, and Ag-PCP│Cu as the

Li reservoir at 0.5 mA cm^{-2}, respectively. Finally, the cells were operated (1 mAh cm^{-2}) for 10 cycles and then stripped to 0.3 V at a fixed current density of 0.5 mA cm^{-2}. For the rate performance, the areal capacity was determined by the time (1 hour) with increasing current density from 1 to 5 mA cm^{-2}, each being cycled 5 times. Galvanostatic cycling tests of LFP//bare Cu, LFP//PCP┃Cu, and LFP//Ag-PCP┃Cu full cells were conducted within a voltage range of 2.5–4.2 V at 1 C-rate. Electrochemical impedance spectroscopy (EIS) was measured at room temperature between 0.1 Hz and 1 MHz with an amplitude of 5 mV. To verify the SEI formation derived by the wetting agent, CV curves were collected using BioLogic Science Instruments (VSP-300) at a scan rate of 0.2 mV s^{-1}.

Electron microscope analysis

For studying the Li morphology, SEM and EDS were recorded using a field emission scanning electron microscope, FE-SEM 7800F Prime (JEOL Ltd, Japan), at 5 kV and 15 kV, respectively. In addition, TEM analysis was performed using JEM-3010(JEOL Ltd, Japan) at 60 kV to observe the lattice distance of the Ag-PCP, and FIB equipment (Helios 5 UX, ThermoFisher) was used to investigate the cross-sectional view of Li deposition. After electrochemical cycling, all the cells were prepared in an argon-filled glove box. All the samples were washed by DME and dried in an argon-filled glove box for 12 hours before electron microscope analysis.

XPS characterization

X-ray photoelectron spectroscopy analysis was carried out using a Kratos Axis Supra with monochromatic Al Kα radiation (1486.7 eV, 240 W) at 15 kV under 5×10^{-10} torr. All spectra were calibrated using carbon C 1s (284.5 eV) as the reference, and the peaks were fitted by the XPSPEAK4.1 software using the Shirley background and Lorentzian-Gaussian curve synthesis. Prior to the XPS characterization, all samples were rinsed with DME to remove the residual Li salts on the surface and dried under argon environment.

TOF-SIMS characterization

To obtain the chemical composition of the SEI layer, time-of-flight secondary ion mass spectrometry (TOF-SIMS) analysis was conducted at a pressure of 3.8×10^{-9} torr by negative polarity to obtain the chemical composition of SEI layer. A Bi^+ (30 keV, 1 pA) ion beam was used as the primary source for detecting the composition of the facile-section (analysis area: $100 \times 100\ \mu m^2$). A Cs^+ ion beam (2 keV, 150 nA) was used as the sputtering source for depth profiling (etching area: $300 \times 300\ \mu m^2$).

3.5 References

[1] J. Liu, Z. Bao, Y. Cui, E. J. Dufek, J. B. Goodenough, P. Khalifah, Q. Li, B. Y. Liaw, P. Liu, A. Manthiram, Y. S. Meng, V. R. Subramanian, M. F. Toney, V. V. Viswanathan, M. S. Whittingham, J. Xiao, W. Xu, J. Yang, X. Q. Yang, J. G. Zhang, *Nat. Energy* **2019**, *4*, 180.

[2] B. Lee, E. Paek, D. Mitlin, S. W. Lee, *Chem. Rev.* **2019**, 5416.

[3] R. Weber, M. Genovese, A. J. Louli, S. Hames, C. Martin, I. G. Hill, J. R. Dahn, *Nat. Energy* **2019**, *4*, 683.

[4] J. Qian, B. D. Adams, J. Zheng, W. Xu, W. A. Henderson, J. Wang, M. E. Bowden, S. Xu, J. Hu, J. G. Zhang, *Adv. Funct. Mater.* **2016**, *26*, 7094.

[5] J. Xiao, Q. Li, Y. Bi, M. Cai, B. Dunn, T. Glossmann, J. Liu, T. Osaka, R. Sugiura, B. Wu, J. Yang, J. G. Zhang, M. S. Whittingham, *Nat. Energy* **2020**, *5*, 561.

[6] C. Fang, J. Li, M. Zhang, Y. Zhang, F. Yang, J. Z. Lee, M. H. Lee, J. Alvarado, M. A. Schroeder, Y. Yang, B. Lu, N. Williams, M. Ceja, L. Yang, M. Cai, J. Gu, K. Xu, X. Wang, Y. S. Meng, *Nature* **2019**, *572*, 511.

[7] W. Chen, R. V. Salvatierra, M. Ren, J. Chen, M. G. Stanford, J. M. Tour, *Adv. Mater.* **2020**, *32*, 1.

[8] Y. Yamada, J. Wang, S. Ko, E. Watanabe, A. Yamada, *Nat. Energy* **2019**, *4*, 269.

[9] M. Genovese, A. J. Louli, R. Weber, C. Martin, T. Taskovic, J. R. Dahn, *J. Electrochem. Soc.* **2019**, *166*, A3342.

[10] Y. Gu, H. Y. Xu, X. G. Zhang, W. W. Wang, J. W. He, S. Tang, J. W. Yan, D. Y. Wu, M. Sen Zheng, Q. F. Dong, B. W. Mao, *Angew. Chemie - Int. Ed.* **2019**, *58*, 3092.

[11] X. Liang, Q. Pang, I. R. Kochetkov, M. S. Sempere, H. Huang, X. Sun, L. F. Nazar, *Nat. Energy* **2017**, *2*, 1.

[12] R. Zhang, X. R. Chen, X. Chen, X. B. Cheng, X. Q. Zhang, C. Yan, Q. Zhang, *Angew. Chemie - Int. Ed.* **2017**, *56*, 7764.

[13] Z. Lu, Q. Liang, B. Wang, Y. Tao, Y. Zhao, W. Lv, D. Liu, C. Zhang, Z. Weng, J. Liang, H. Li, Q. H. Yang, *Adv. Energy Mater.* **2019**, *9*, 1.

[14] Z. Xiong, C. Dong, H. Cai, C. Liu, X. Zhang, *Mater. Chem. Phys.* **2013**, *141*, 416.

[15] Y. J. Gong, J. W. Heo, H. Lee, H. Kim, J. Cho, S. Pyo, H. Yun, H. Kim, S. Y. Park, J. Yoo, Y. S. Kim, *Adv. Energy Mater.* **2020**, *10*, 1.

[16] Y. J. Gong, S. Pyo, H. Kim, J. Cho, H. Yun, H. Kim, S. Ryu, J. Yoo, Y. S. Kim, *Energy Environ. Sci.* **2021**, *14*, 940.

[17] X. Wang, A. K. K. Kyaw, C. Yin, F. Wang, Q. Zhu, T. Tang, P. I. Yee, J. Xu, *RSC Adv.* **2018**, *8*, 18334.

[18] N. A. Shahrim, Z. Ahmad, A. Wong Azman, Y. Fachmi Buys, N. Sarifuddin,

Mater. Adv. **2021**, *2*, 7118.

[19] S. Nanda, A. Gupta, A. Manthiram, *Adv. Energy Mater.* **2021**, *11*, 1.

[20] A. C. Bhowal, H. Talukdar, S. Kundu, *Polym. Bull.* **2019**, *76*, 5233.

[21] D. S. Patil, S. A. Pawar, J. Hwang, J. H. Kim, P. S. Patil, J. C. Shin, *J. Ind. Eng. Chem.* **2016**, *42*, 113.

[22] N. Kim, S. Kee, S. H. Lee, B. H. Lee, Y. H. Kahng, Y. R. Jo, B. J. Kim, K. Lee, *Adv. Mater.* **2014**, *26*, 2268.

[23] E. Hosseini, V. Ozhukil Kollath, K. Karan, *J. Mater. Chem. C* **2020**, *8*, 3982.

[24] C. M. Palumbiny, F. Liu, T. P. Russell, A. Hexemer, C. Wang, P. Müller-Buschbaum, *Adv. Mater.* **2015**, *27*, 3391.

[25] I. Petsagkourakis, E. Pavlopoulou, G. Portale, B. A. Kuropatwa, S. Dilhaire, G. Fleury, G. Hadziioannou, *Sci. Rep.* **2016**, *6*, 30501.

[26] Y. Zhao, S. Zhang, T. Yu, Y. Zhang, G. Ye, H. Cui, C. He, W. Jiang, Y. Zhai, C. Lu, X. Gu, N. Liu, *Nat. Commun.* **2021**, *12*, 1.

[27] S. Rudd, J. F. Franco-Gonzalez, S. Kumar Singh, Z. Ullah Khan, X. Crispin, J. W. Andreasen, I. Zozoulenko, D. Evans, *J. Polym. Sci. Part B Polym. Phys.* **2018**, *56*, 97.

[28] B. Xu, G. Sai-Anand, H. M. Jeong, S. W. Kim, J. S. Kim, J. B. Kwon, S. W. Kang, *Materials (Basel).* **2018**, *11*, 1.

[29] E. Mitraka, M. J. Jafari, M. Vagin, X. Liu, M. Fahlman, T. Ederth, M. Berggren, M. P. Jonsson, X. Crispin, *J. Mater. Chem. A* **2017**, *5*, 4404.

[30] S. J. Wang, Y. J. Choi, H. H. Park, *J. Appl. Phys.* **2011**, *109*, 1.

[31] S. Funda, T. Ohki, Q. Liu, J. Hossain, Y. Ishimaru, K. Ueno, H. Shirai, *J. Appl. Phys.* **2016**, *120*, 033103.

[32] Q. Xu, S. M. Xu, R. Tian, C. Lu, *ACS Appl. Mater. Interfaces* **2020**, *12*, 13371.

[33] H. Mao, W. Yu, Z. Cai, G. Liu, L. Liu, R. Wen, Y. Su, H. Kou, K. Xi, B. Li, H. Zhao, X. Da, H. Wu, W. Yan, S. Ding, *Angew. Chemie - Int. Ed.* **2021**, *60*, 19306.

[34] M. Wang, Z. Peng, W. Luo, F. Ren, Z. Li, Q. Zhang, H. He, C. Ouyang, D. Wang, *Adv. Energy Mater.* **2019**, *9*, 1.

[35] H. Park, O. Tamwattana, J. Kim, S. Buakeaw, R. Hongtong, B. Kim, P. Khomein, G. Liu, N. Meethong, K. Kang, *Adv. Energy Mater.* **2021**, *11*, 1.

[36] A. Pei, G. Zheng, F. Shi, Y. Li, Y. Cui, *Nano Lett.* **2017**, *17*, 1132.

[37] C. P. Yang, Y. X. Yin, S. F. Zhang, N. W. Li, Y. G. Guo, *Nat. Commun.* **2015**, *6*, 8058.

[38] Y. Lu, C. Z. Zhao, H. Yuan, X. B. Cheng, J. Q. Huang, Q. Zhang, *Adv. Funct. Mater.* **2021**, 2009925.

[39] R. Xu, J. F. Ding, X. X. Ma, C. Yan, Y. X. Yao, J. Q. Huang, *Adv. Mater.* **2021**, *33*, 1.

[40] Z. T. Wondimkun, W. A. Tegegne, J. Shi-Kai, C. J. Huang, N. A. Sahalie, M. A. Weret, J. Y. Hsu, P. L. Hsieh, Y. S. Huang, S. H. Wu, W. N. Su, B. J. Hwang, *Energy Storage Mater.* **2021**, *35*, 334.

[41] J. Fu, X. Ji, J. Chen, L. Chen, X. Fan, D. Mu, C. Wang, *Adv. Mater.* **2020**, *132*, 22378.

[42] Y. Sato, K. Itoh, R. Hagiwara, T. Fukunaga, Y. Ito, *Carbon N. Y.* **2004**, *42*, 3243.

[43] J. Kim, R. Zhou, K. Murakoshi, S. Yasuda, *RSC Adv.* **2018**, *8*, 14152.

[44] Y. Yang, D. M. Davies, Y. Yin, O. Borodin, J. Z. Lee, C. Fang, M. Olguin, Y. Zhang, E. S. Sablina, X. Wang, C. S. Rustomji, Y. S. Meng, *Joule* **2019**, *3*, 1986.

[45] T. T. Beyene, B. A. Jote, Z. T. Wondimkun, B. W. Olbassa, C. J. Huang, B. Thirumalraj, C. H. Wang, W. N. Su, H. Dai, B. J. Hwang, *ACS Appl. Mater. Interfaces* **2019**, *11*, 31962.

[46] C. Zhang, Q. Lan, Y. Liu, J. Wu, H. Shao, H. Zhan, Y. Yang, *Electrochim. Acta* **2019**, *306*, 407.

[47] Q. Xu, X. Yang, M. Rao, D. Lin, K. Yan, R. A. Du, J. Xu, Y. Zhang, D. Ye, S. Yang, G. Zhou, Y. Lu, Y. Qiu, *Energy Storage Mater.* **2020**, *26*, 73.

[48] C. Yan, Y.-X. Yao, X. Chen, X.-B. Cheng, X.-Q. Zhang, J.-Q. Huang, Q. Zhang, *Angew. Chemie* **2018**, *130*, 14251.

[49] R. Zhang, X. Chen, X. Shen, X. Q. Zhang, X. R. Chen, X. B. Cheng, C. Yan, C.

Z. Zhao, Q. Zhang, *Joule* **2018**, *2*, 764.

[50] J. Zheng, J. A. Lochala, A. Kwok, Z. D. Deng, J. Xiao, *Adv. Sci.* **2017**, *4*, 1.

[51] L. E. Camacho-Forero, T. W. Smith, P. B. Balbuena, *J. Phys. Chem. C* **2017**, *121*, 182.

[52] S. H. Wang, J. Yue, W. Dong, T. T. Zuo, J. Y. Li, X. Liu, X. D. Zhang, L. Liu, J. L. Shi, Y. X. Yin, Y. G. Guo, *Nat. Commun.* **2019**, *10*, 1.

[53] L. Lin, L. Suo, Y. sheng Hu, H. Li, X. Huang, L. Chen, *Adv. Energy Mater.* **2021**, *11*, 1.

[54] Z. Xie, Z. Wu, X. An, X. Yue, J. Wang, A. Abudula, G. Guan, *Energy Storage Mater.* **2020**, *32*, 386.

[55] V. Pande, V. Viswanathan, *ACS Energy Lett.* **2019**, *4*, 2952.

[56] S. S. Zhang, X. Fan, C. Wang, *Electrochim. Acta* **2017**, *258*, 1201.

[57] B. D. Adams, J. Zheng, X. Ren, W. Xu, J. G. Zhang, *Adv. Energy Mater.* **2018**, *8*, 1.

[58] Y. Qiao, H. Yang, Z. Chang, H. Deng, X. Li, H. Zhou, *Nat. Energy* **2021**, *6*, 653.

[59] Y. Tian, Y. An, C. Wei, H. Jiang, S. Xiong, J. Feng, Y. Qian, *Nano Energy* **2020**, *78*, 105344.

[60] J. Oh, J. Lee, T. Hwang, J. M. Kim, K. dong Seoung, Y. Piao, *Electrochim. Acta* **2017**, *231*, 85.

Chapter 4 Conclusion and Outlook

In conclusion, this dissertation proposes interfacial stabilization strategies for high-energy-density Li metal-based batteries. Furthermore, I demonstrate the interfacial fluorination mechanism of conjugated structures, which is related to LiF formation in the SEI layer.

In Chapter 2, the introduction of the functional carbon-coated separator shows excellent interfacial stability in LMBs. Carbon-family materials with high mechanical strength physically inhibit Li dendrite growth, and conjugated carbon network (CCN) induces fluorinated metathesis to form the SEI layer with a high proportion of LiF, leading to outstanding cycle stability even under high-speed charging/discharging conditions. In particular, carbon materials with different structures, including graphene, carbon black, and activated carbon, are applied as coating layer on the separator, thereby revealing the correlation between CCN materials and fluorinated metathesis and generalizing the stabilization mechanism. As a result, when applying the CCN material with a long-range sp^2 π conjugation electron system and the complete lattice structure, the F-doping mechanism occurs easily, which maximizes the stabilization effect of LMAs by promoting LiF formation.

In Chapter 3, the silver nanoparticles incorporated p-doped conjugated polymer (Ag-

PCP) wetting agent on the copper current collector is applied to improve the interfacial stability in AFLMBs. Moreover, I verify the interfacial fluorinated mechanism of the Ag-PCP with the π-conjugated structure to efficiently regulate the favorable SEI chemistry. In the Ag-PCP applied cells, the synergistic effect of Ag-Li alloying and interfacial fluorination on Ag-PCP wetting agent not only stabilizes the Li plating behavior but also promotes the formation of LiF-rich SEI. Consequently, the plated Li shows a compact column-like structure with dendrite-free morphology, and the anode-free cells achieve superior cycling stability with a long lifespan even under harsh conditions.

Overall, this dissertation uncovers interfacial fluorination mechanism based on various optophysical analysis, electrochemical measurements, and density functional theory (DFT) calculation, such as X-ray photoelectron spectroscopy (XPS), time-of-flight secondary ion mass spectrometer (TOF-SIMS), scanning electron microscopy (SEM), transmission electron microscopy (TEM), focused ion beam (FIB), grazing-incidence wide-angle X-ray scattering (GIWAXS), Fourier transform infrared spectrometer (FT-IR), X-ray diffraction (XRD), electrochemical impedance spectroscopy (EIS), cyclic voltammetry (CV), galvanostatic cycling test. Additionally, it helps fundamental understating the reaction at the anode interfaces and stable SEI formation. The proposed systems have the advantage of forming LiF-rich SEI *via* in-situ fluorination reaction in the cell operating window without requiring any extra additives or post-treatment, and have little effect on the gravimetric/volumetric energy density of the entire cell. With the advantages mentioned above, these strategies provide valuable insights into anode interface stabilization for next-generation rechargeable batteries with high energy density.

List of publications

- **Seonmi Pyo**, Seokgyu Ryu, Yong Jun Gong, Jinil Cho, Heejun Yun, Heebae Kim, Jeewon Lee, Byeongyun Min, Youngkyu Choi, Jeeyoung Yoo, and Youn Sang Kim, "Lithiophilic Wetting Agent Inducing Interfacial Fluorination for Long-Lifespan Anode-Free Lithium Metal Batteries" ***Advanced Energy Materials**, 13, 2203573 (2023)*
- **Seonmi Pyo**, Yong Jun Gong, Hyunjin Kim, Jinil Cho, Heejun Yun, Heebae Kim, Seokgyu Ryu, Jeeyoung Yoo, and Youn Sang Kim, "Advanced Li metal anode by fluorinated metathesis on conjugated carbon networks" ***Energy & Environmental Science**, 14, 940-954 (2021)*
- **Seonmi Pyo**, Gayeong Yoo, Yong Jun Gong, Jinil Cho, Heebae Kim, Youn Sang Kim, and Jeeyoung Yoo, "Highly reliable quinone-based cathodes and cellulose nanofiber separators: toward eco-friendly organic lithium batteries" ***Cellulose**, 27, 6707–6717 (2020)*
- Heejun Yun, Jinil Cho, Seokgyu Ryu, **Seonmi Pyo**, Heebae Kim, Jeewon Lee, Byeongyun Min, Yong Hyun Cho, Harim Seo, Jeeyoung Yoo, and Youn Sang Kim, "Surface Oxygen Vacancy Inducing Li-Ion-Conducting Percolation Network in Composite Solid Electrolytes for All-Solid-State Lithium-Metal Batteries" ***Small**,*

2207223 (2023)

- Jinil Cho, Seokgyu Ryu, Yong Jun Gong, **Seonmi Pyo**, Heejun Yun, Heebae Kim, Jeewon Lee, Jeeyoung Yoo, and Youn Sang Kim, "Nitrogen-doped MoS2 as a catalytic Sulfur Host for Lithium-Sulfur Batteries" ***Chemical Engineering Journal****, 439, 135568 (2022)*
- Heebae Kim, Changik Im, Seokgyu Ryu, Yong Jun Gong, Jinil Cho, **Seonmi Pyo**, Heejun Yun, Jeewon Lee, Jeeyoung Yoo, and Youn Sang Kim, "Interface Modeling via Tailored Energy Band Alignment: Toward the Electrochemically Stabilized All-Solid-State Li-Metal Battery" ***Advanced Functional Materials****, 32, 2107555 (2022)*
- Juyeon Han, Youngkyu Choi, Junyeong Lee, **Seonmi Pyo**, Sungjin Jo, and Jeeyoung Yoo, "UV curable ionogel for all-solid-state supercapacitor" ***Chemical Engineering Journal****, 416, 129089 (2021)*
- Yong Jun Gong, Jung woon Heo, Hakji Lee, Hyunjin Kim, Jinil Cho, **Seonmi Pyo**, Heejun Yun, Heebae Kim, Sang Yoon park, Jeeyoung Yoo, and Youn Sang Kim, "Nonwoven rGO Fiber-Aramid Separator for High-Speed Charging and Discharging of Li Metal Anode" ***Advanced Energy Materials****, 10, 2001479 (2020)*
- Jinil Cho, Yong-keon Ahn, Yong Jun Gong, **Seonmi Pyo**, Jeeyoung Yoo, and Youn Sang Kim, "An organic–inorganic composite separator for preventing shuttle effect in lithium–sulfur batteries" ***Sustainable Energy & Fuels****, 4, 3051-3057 (2020)*

- Yong Jun Gong, Hyunjin Kim, Gayeong Yoo, Jinil Cho, **Seonmi Pyo**, Yong Hyun Cho, Jeeyoung Yoo, and Youn Sang Kim, "Ni-Particle-Embedded Bilayer Gel Polymer Electrolyte for Highly Stable Lithium Metal Batteries" ***ACS Applied Energy Materials**, 2, 11, 8310-8318 (2019)*

요 약 (국문초록)

리튬 금속 기반 배터리의 우수한 사이클 성능을 위한 공액 구조에서의 불소화 계면 공정

표 선 미
융합과학부 나노융합전공
융합과학기술대학원
서울대학교

에너지 저장 시스템으로서 고에너지 밀도를 가진 이차 전지는 스마트폰에서 전기 자동차까지 광범위한 응용 분야에서 큰 관심을 받고 있다. 최근 리튬 금속 기반 배터리는 유망한 차세대 에너지 저장 기술 중 하나로 주목받고 있다. 이는 음극으로 사용하는 리튬 금속이 가장 낮은 전기화학적 전위, 높은 이론적 용량 및 낮은 중량 밀도를 가지고 있기 때문이다. 이러한 점에서, 리튬 금속 배터리와 과량의 리튬이 없는 무음극 리튬 금속 배터리는 고에너지 밀도를 가진 가장 이상적인 시스템이다.

하지만 이러한 장점에도 불구하고, 리튬 금속 기반 배터리는 리튬 금속

의 높은 반응성 및 호스트가 없는 전기화학적 도금/벗김 과정으로 인해 수지상 리튬 성장, 반복적인 SEI 층 형성 및 균열로 인해 실제 이용하는 데에는 어려움이 있다. 특히, 기존의 리튬 금속 배터리와는 달리, 무음극 리튬 금속 배터리는 리튬 활물질 손실을 보상할 만한 과량의 리튬이 없는 시스템으로써 사이클 성능을 향상시키는 것은 더 어렵다. 이러한 문제를 해결하기 위해, 이 논문에서는 플루오린화 리튬이 풍부한 SEI 형성 및 리튬 거동 안정화에 초점을 맞춘 계면 화학에 관한 연구를 다룬다.

첫 번째 연구는 리튬 금속 배터리에 관한 것으로 그래핀, 카본블랙, 활성탄과 같은 공액 탄소망 소재를 활용한 기능성 안전 강화 분리막을 도입한 시스템이다. 이는 특정 전해질 용매 조건에서 셀의 충방전 동안, 분리막의 탄소 코팅층에서 자가 불소 도핑 반응을 유도해 리튬 금속 음극에 플루오린화 리튬이 풍부한 SEI층을 형성하고자 하였다. 또한, 다른 구조를 가진 공액 탄소망 재료와 불소화 매커니즘 사이의 상관관계를 증명함으로써 리튬 금속 음극의 안정화 메커니즘을 일반화하였다.

두 번째 연구는 무음극 리튬 금속 배터리에 관한 것으로 은과 전도성 고분자 복합체가 코팅된 음극 집전체를 도입한 시스템이다. 이 복합 코팅층은 은과 리튬의 합금 반응 및 공액 구조로 인한 계면 불소화 반응을 촉진하였고, 이를 통해 사이클 초기 단계에서부터 리튬 핵 생성 에너지 장벽을 효과적으로 낮추고, 높은 비율의 플루오린화 리튬을 가진 안정적인

SEI 층을 생성하였다. 그 결과, 은과 전도성 고분자의 복합 코팅층을 적용한 배터리는 고속 충방전, 고용량 조건에서의 사이클 후에도 덴드라이트가 관찰되지 않았고, 높은 리튬 가역성을 가진 우수한 사이클 성능을 보였다.

이 연구들은 리튬 금속 기반 배터리의 계면 안정화를 위한 유망한 전략을 제시하고, 궁극적으로는 고에너지 밀도를 가진 이차 전지의 실용화를 목표로 한다.

주요어: 기능성 분리막, 리튬 친화 물질, 계면 불소화, 플루오린화 리튬이 풍부한 보호층, 덴드라이트가 없는 모폴로지, 리튬 금속 기반 배터리

학 번: 2018-21982